Pushing the boundaries of photoconductive sampling in solids

Najd Abdulaziz Suliman Altwaijry

München 2023

Pushing the boundaries of photoconductive sampling in solids

Najd Abdulaziz Suliman Altwaijry

Dissertation
an der Fakultät für Physik
der Ludwig–Maximilians–Universität
München

vorgelegt von
Najd Abdulaziz Suliman Altwaijry
aus Riad, Saudi-Arabien

München, den 13. April 2023

Erstgutachter: Prof. Dr. Matthias F. Kling
Zweitgutachterin: PD. Dr. Hanieh Fattahi
Tag der mündlichen Prüfung: 5. Juni 2023

إلى أبوي
عبدالعزيز سليمان التويجري
وأمي
الجوهرة محمد الخيال

Contents

Abstract

The advent of laser-based optical tools featuring few-cycle pulses with durations of less than a hundred femtoseconds in the late 1980s enabled scientists to initiate and observe the evolution of chemical reactions. This powerful approach combined the interactions of light and matter and unleashed an unprecedented metrology concept that tracks the interactions of atoms and molecules in their natural timescales. Electron wavepacket dynamics take place in the attosecond range, a thousand times faster than molecules. In optical terms, such durations typically last less than the half-cycle duration of optical fields. Consequently, the investigation of such electronic processes necessitates measurement techniques capable of resolving the oscillations of the electric field of light. The primary objective of this thesis is to develop and advance novel field characterisation techniques based on photoconductive sampling.

The first portion of this thesis addresses broadband field characterisation based on nonlinear photoconductive sampling. A theoretical analysis of current formation and localisation in solids is presented, prompting the fabrication of a heterostructured sample with the aim of enhancing the magnitude of the signal obtained from the measurement technique. A thorough proof-of-principle experiment is performed, whereby a significant enhancement in signal magnitude is established. As a consequence of signal improvement, the heterostructured sample reaches the desired stability regime earlier than its traditional bulk counterparts. Moreover, the performance of the heterostructured sample for field characterisation is compared to fused silica and benchmarked against the well-established technique of electro-optic sampling. These results pave the way towards field sampling in low pulse energy systems.

The following section details broadband field characterisation based on linear photoconductive sampling by employing tailored pulses from a waveform synthesiser. Visible-ultraviolet pulses are utilised to inject carriers in a common semiconductive material (gallium phosphide), enabling the complete characterisation of a mid-infrared test field. Furthermore, the technique is validated against electro-optic sampling. When compared to electro-optic sampling, the response function

of linear photoconductive sampling is concerned with the intensity envelope of the gating field, relaxing the strict requisites on the temporal phase of the gate. The demonstrated results represent a significant achievement in extending field sampling techniques beyond 100 THz and towards the visible range.

Finally, a machine learning-based algorithm for denoising waveforms obtained from a laboratory setting is developed and implemented. The algorithm is based on a one-dimensional convolutional neural network, ideal for processing data presented on an evenly spaced grid. The model is compared with well-established methodologies, namely denoising via the fast Fourier transform and wavelet analysis and exhibits excellent performance, extending the repertoire of tools typically used for combating noise.

The field characterisation methodologies presented in this thesis pave the way towards accessible and cost-effective field sampling techniques, enabling researchers to study field-induced electron dynamics in matter and usher in ultrafast optoelectronic signal processing towards the PHz range. In general, the field characterisation techniques presented occupy a small footprint, and the measurements take place in ambient air conditions, facilitating their integration in existing experimental infrastructures. With the aid of AI-accelerator chips, the machine learning tool developed in this thesis can be implemented during laboratory measurements as a concurrent denoising technique.

Zusammenfassung

Die Entwicklung laser-basierter Messinstrumente, welche sich durch sehr kurze Impulsdauern von weniger als 100 Femtosekunden auszeichneten, dies entspricht nur ein paar Schwingungen des EM-Feldes, erlaubte es Wissenschaftlern in den späten achtziger Jahren chemische Reaktionen optisch einzuleiten und deren Ablauf zu beobachten. Basierend auf der direkten Wechselwirkung von Licht und Materie ermöglichte diese neue Art der Metrologie erstmals die Beobachtung der Wechselwirkungen von Atomen und Molekülen auf deren natürlichen Zeitskalen. Die Dynamik von Elektron-Wellenpaketen hingegen kann bis zu tausendmal schneller ablaufen und liegt typischerweise im Attosekundenbereich. Dies entspricht nur einem kleinen Bruchteil der optischen Wellenschwingung. Um solch schnelle Prozesse untersuchen zu können, sind Messtechniken nötig, welche dazu in der Lage sind, die Oszillationen des elektrischen Lichtfeldes aufzulösen. Die Entwicklung und Verbesserung, der noch jungen Lichfeldcharakterisierung durch feldinduzierten Fotostrom (engl. photoconductive sampling PCS), stellt den Schwerpunkt dieser Arbeit dar.

Der erste Teil dieser Arbeit befasst sich mit der breitbandigen Lichtfeldcharakterisierung mittels nichtlinear-induziertem Fotostrom. Eine Analyse der Erzeugung und Lokalisation des Stroms im Festkörper legt die Herstellungen einer heterostrukturierten Probe nahe, um die Signalstärke des gemessenen Signals zu erhöhen. In einem ersten Versuch wurde hiermit ein deutlicher Anstieg der Signalstärke erreicht. Darüber hinaus wird mit der neuen Struktur der lineare Arbeits-Messbereich früher erreicht als im Falle des einfachen klassischen Mediums. Zusätzlich wurde ein Vergleich mit der verbreiteten Technik des induzierten elektrooptischen Effekts durchgeführt. Die Resultate sind sehr vielversprechend und erlauben insbesondere Lasersystemen mit deutlich geringerer Energie feldaufgelöste Messungen durchzuführen.

Der nächste Teil widmet sich unter anderem der breitbandigen Charakterisierung mittels linearer PCS unter Verwendung von maßgeschneiderten Lichtpulsen eines optischen Synthesizers. Die Ladungsträger werden durch Lichtpulse, welche das sicht-

bare bis ultraviolette Spektrum abdecken, in Galliumphosphid erzeugt und erlauben die vollständige Charakterisierung eines Abfrage-Lichtfeldes im mittleren infraroten Spektralbereich. Darüber hinaus wird die Methode einer anderen Technik, welche den induzierten elektrooptischen Effekt vermisste, gegenübergestellt. Im Gegensatz zum elektrooptischen Effekt, ist die Antwortfunktion des linearen PCS von der Intensitätseinhüllenden des Anregungspulses abhängig und nicht von der Phase der Trägerfrequenz. Die erzielten Ergebnisse stellen eine erhebliche Erweiterung des messbaren Spektralbereichs dar und erlaubt Frequenzen jenseits von 100 THz phasentreu zu detektieren und nähert sich damit dem sichtbaren Spektralbereich an.

Abschließend wird ein Algorithmus, basierend auf maschinellem Lernen, zur Rauschunterdrückung für diese Messungen entwickelt. Die zugrunde liegende Struktur des Algorithmus ist ein eindimensionales faltendes neuronales Netzwerk (engl. Convolutional Neural Network) welches sich hervorragend dazu eignet Daten auf einem regelmäßigen Gitter zu verarbeiten. Das so erstellte Model wird dann mit verschiedenen, weit verbreiteten Methoden zur Rauschunterdrückung, namentlich Rauschunterdrückung mittels Fourier- und Wavelet-Transformation, verglichen. Das Model überzeugt in diesem Vergleich und stellt damit eine neue Option dar, um Signal aus den Messungen zu extrahieren.

Die hier präsentierten Methoden zur Charakterisierung des elektrischen Lichtfeldes ebnen den Weg für eine leicht verfügbare und kosteneffiziente Technologie, welche es Wissenschaftlern erlaubt feldinduzierte Elektronendynamiken in Materie zu untersuchen und treibt die ultraschnelle optische Signalverarbeitung weiter in Richtung PHz. Sie zeichnen sich durch ihre Kompaktheit und einfache Anwendbarkeit aus, da sie unter Normalbedingungen im Labor durchgeführt werden können und damit sehr einfach in bestehende Experimente integrierbar sind. Darüber hinaus kann das hier entwickelte maschinell erlernte Hilfsmittel, mithilfe von KI-Beschleunigungs Prozessoren, direkt im Labor zur Rauschunterdrückung eingesetzt werden.

List of Abbreviations

AI	artificial intelligence
BBO	beta-barium borate, β-BaB_2O_4
BPF	bandpass filter
CEP	carrier-envelope phase
CMC	chirped mirror compressor
DFG	difference-frequency generation
EOS	electro-optic sampling
FFT	fast Fourier transform
FROG	frequency-resolved optical gating
FS	fused silica
FWHM	full width at half maximum
GaP	gallium phosphide
GDD	group-delay dispersion
GVD	group-velocity dispersion
HCF	hollow-core fiber
HEMT	high electron mobility transistor
iDFG	intrapulse difference-frequency generation
LO	local oscillator
LPS	linear photoconductive sampling
MIR	mid-infrared
ML	machine learning
NIR	near-infrared
NPS	nonlinear photoconductive sampling
OPCPA	optical parametric chirped pulse amplification
PPLN	periodically polled lithium niobate
RK4	Runge-Kutta-4
SFG	sum-frequency generation
Si	silicon

SiO_2	silicon dioxide
TiA	transimpedance amplifier
Ti:Sa	titanium doped sapphire, $Ti^{3+}:Al_2O_3$
VIS-UV	visible-ultraviolet
WP	Wollaston prism
XUV	extreme ultraviolet
Yb:YAG	ytterbium-doped yttrium aluminum garnet, $Yb^{3+}:Y_3Al_5O_{12}$

List of Figures

Introduction

The first laser—a ruby solid-state laser—introduced by Theodore Maiman [1] was naturally pulsed due to its operation mechanism. The duration of the pulses produced by Maiman was in the order of a millisecond, a few hundred times faster than the time it takes a human to blink. As time went by, pulsed lasers underwent developments to produce ever shorter pulses of nano-, pico-, femto- and ultimately attosecond durations, with each generation presenting substantial developmental challenges [2–7]. In the field of optics, the terms ultrafast or ultrashort are generally reserved for pulses in the range of femto- to attosecond durations.

Nowadays, pulses lasting a few femtoseconds ($1\,\mathrm{fs} = 10^{-15}\,\mathrm{s}$) are routinely produced by commercially available systems in both high and low pulse energy regimes. The key difference is where and for what purpose these pulses are used. This notable improvement in the quality and sophistication of laser systems enabled greater precision and accuracy in scientific endeavours. For instance, attosecond science [8], the powerhouse of modern ultrafast science, relies on high pulse energy systems with sufficient field strengths to generate extremely short bursts of light (high harmonic generation), in the attosecond duration range, using an extremely nonlinear ionisation process. The photo-emitted electrons generate extreme ultraviolet bursts of light via recombination with the parent atom, typically from a noble gas [9], but this process can also be done in solids [10] as well as liquids [11]. The technique allows for studying electronic processes in atoms [12, 13], molecules [14–17] and solids [18–21] in their natural timescales of $= 10^{-18}\,\mathrm{s}$. Without such laser systems, this feat would be unachievable.

Attosecond research forms the foundation upon which many contemporary field sampling techniques are built [22]. To sample a field, a shorter event, typically another field, is required to gate the process. In attosecond science, the short gate, i.e. the extremely short burst of light, is generated via nonlinear photo-emission and recombination of electrons. The extreme nonlinearity needed to generate the gate field, however, is in itself a significant disadvantage of the technique since the process is highly inefficient. Moreover, the nature of attosecond science necessi-

tates working in vacuum environments, which imposes strict requirements on the budget, infrastructure and complexity of the systems, limiting the technique to a few laboratories across the world. The quest for developing techniques capable of resolving optical fields and, at the same time, avoiding the problems set by attosecond science led to early demonstrations by Schiffrin *et al.* [23] of optical-field induced currents in dielectrics, which paved the way for works such as [24–26], and inspired the investigation of field-induced electronic processes in solids on attosecond timescales without the need for a costly vacuum infrastructure. The technique, dubbed nonlinear photoconductive sampling, proved capable of detecting fields from 100-1100 THz [27]. Nevertheless, the origins of this concept dates back to the 1980s, with works by Auston [28, 29] using linear absorption of photons for field sampling. Linear absorption of photons proved capable of detecting fields down to 100 THz, as demonstrated by Ashida *et al.* [30] in 2008. Since then, Ossiander *et al.* [31] employed vacuum-ultraviolet pulses to sample the field of a visible-near-infrared pulse using linear absorption, defining the band-structure limit of ultrafast optoelectronics in lithium fluoride. In 2018, Park *et al.* [32] demonstrated another ambient technique for field sampling in air based on tunnelling ionisation with a perturbation for the time-domain observation of an electric field (TIPTOE). This technique, similar to nonlinear photoconductive sampling, relies on nonlinearity to generate a 190 as gate pulse capable of resolving the electric field of an arbitrary test pulse up to 1.5 PHz. Within a few years, Liu *et al.* [33] demonstrated single-shot measurements of few-cycle 3.4 μm waveforms on a silicon chip using TIPTOE.

Generally speaking, field sampling metrology can be divided into two categories: field sampling based on photon-electron interactions and field sampling based on photon-photon interactions. Fig. 1 illustrates an overview of the different field resolved measurement techniques and some of their milestones. So far, field sampling based on photon-electron interactions has been mentioned. Techniques based on photon-photon interactions entail the nonlinear interaction of the gate pulse and the test pulse in a nonlinear medium, typically a crystal. The earliest demonstration of this concept, dubbed electro-optic sampling, dates back to the early 1980s [34], by exploiting the Pockels effect in lithium niobate. Soon after, it was demonstrated that this technique is capable of the complete characterisation of the electric field of a teraherz pulse based on second order nonlinear mixing [42, 43]. A significant advancement in electro-optic sampling was demonstrated by Porer *et al.* [37]. By combining spectral filtering with electro-optic sampling, a notable reduction in the shot-noise of the technique was achieved. This concept and reduction in noise via post-filtering enabled the detection of near-infrared [38] and visible [39] fields. Nevertheless, nonlinear mixing is not limited to second order nonlinearity. Zimin *et al.* pushed the detection limit of electro-optic sampling to PHz scales by relying on a

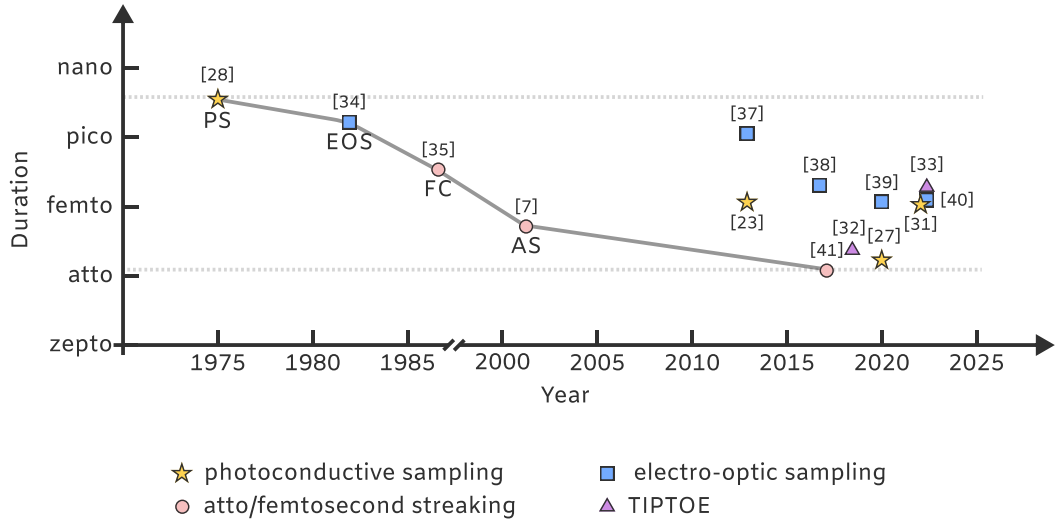

Figure 1: Overview of field sampling metrology techniques. The shapes represent different sampling techniques at their time of inception as well as significant milestones. Photoconductive sampling (PS, stars) following the works of Auston in 1975 [28] reached unprecedented levels of sampling precision, as implemented by Schiffrin *et al.* [23], Sederberg *et al.* [27] and Ossiander *et al.* [31] in the last decade. In the early 1980s, works by Valdmanis *et al.* [34] introduced the concept of electro-optic sampling (EOS, squares). Within a few years, femtochemistry (FC, circles), pioneered by Zewail in the late 1980s [35], enabled time-resolved observations of chemical reactions. Not too long after, with the advent of carrier-envelope phase stability and chirped mirror technology, the first isolated attosecond pulses were achieved by Henschel *et al.* [7, 36]. A breakthrough in the concept of electro-optic sampling, was shown by Porer *et al.* [37] and employed by Keiber *et al.* [38], to push the limit of EOS detection down to the near-infrared range by combining spectral filtering with a short visible-near-infrared sampling pulse. It was closely followed by pushing the limit to visible fields using visible-ultraviolet pulses from a waveform synthesiser by Ridente *et al.* [39]. Nonlinear mixing enabled Zimin *et al.* [40] to push the detection limit of electro-optic sampling to PHz scales. Within a year, Gaumnitz *et al.* [41] achieved 43 as pulses. By 2016, ambient field sampling techniques have been established and employed for phase detection [24, 25]. Two years later, Park *et al.* demonstrated how tunnelling ionisation in a gas generates a 190 as gate capable of resolving the electric field of an arbitrary pulse up to 1.5 PHz [32] in a technique called TIPTOE (triangles).

more generalised approach that exploits second and third order nonlinearities [40].

In this thesis field sampling techniques based on the concept of photoconductive sampling are developed and implemented. In Chapter 2, the technique of nonlinear photoconductive sampling is employed to study the functionality of an in-house engineered heterostructured sample. The idea behind this sample is to utilise an alternating structure of silicon and fused silica to boost the device's overall output and signal-to-noise ratio, shifting the energy requirements towards applications in low pulse energy systems such as oscillators. Next, in Chapter 3, the technique of linear photoconductive sampling is implemented in gallium phosphide in ambient air conditions, pushing the detection limit from 60-100 THz [30, 44] to more than 200 THz. Both techniques are compared to the established technique of electro-optic sampling [45, 46], with the added benefit of avoiding some of the issues imposed by electro-optic sampling, for example: phase-matching.

Nevertheless, every measurement performed in a laboratory is typically and unfortunately plagued by noise, and significant effort is usually put into improving the precision, reproducibility and signal-to-noise ratio of the measurement. To this end, methods such as active stabilisation, Fourier filtering, averaging, integration and so on have been developed and implemented over the decades to combat these issues. Chapter 4 introduces a contemporary solution to the problem based on the emergent technology of machine learning. In Chapter 4, a machine learning model based on a convolutional neural network is trained on augmented data acquired from laboratory measurements to denoise and extract waveforms relevant to the measurements in this thesis. The model is compared with traditional techniques such as Fourier filtering and wavelet analysis with excellent outcomes.

Chapter 1

Theoretical background and experimental foundations

The main objective of this chapter is to introduce a succinct mathematical description of ultrafast optics, by discussing few-cycle pulses and their interactions with matter, and in particular with solid state systems. Next, it covers the theoretical background of the physical processes explored and utilised as field sampling techniques in this thesis. Specifically, the techniques of electro-optic sampling, as well as linear and nonlinear photoconductive sampling, are considered.

The first Section (1.1) introduces basic concepts and the mathematical formalism for describing ultrashort pulses in the time and frequency domains, followed by Section (1.2), introducing light-matter interactions before finally concluding with Section (1.3) detailing experimental approaches for resolving the electric field of light.

1.1 Few-cycle pulses

Light pulses are packets of electromagnetic waves fully described by the Maxwell-Heaviside equations:

$$\begin{aligned} \nabla \cdot \vec{D} &= \rho \\ \nabla \cdot \vec{B} &= 0 \\ \nabla \times \vec{E} &= -\frac{\partial \vec{B}}{\partial t} \\ \nabla \times \vec{H} &= \frac{\partial \vec{D}}{\partial t} + \vec{J} \end{aligned} \tag{1.1}$$

where $\vec{E}$ is the total electric field, ρ is the free charge density, $\vec{B}$ is the total magnetic field, $\vec{H}$ is the magnetic field strength, $\vec{D}$ is the electric displacement field and $\vec{J}$ is the free current density. The fields $\vec{E}$ and $\vec{D}$ are related by the polarisation of the medium, such that $\vec{D} = \epsilon_0\vec{D} + \vec{P}$ and for a nonmagnetic medium, $\vec{B} = \mu_0\vec{H}$.

By following Maxwell's equations, we can deduce that the relationship between the magnitude of the magnetic field and the electric field is:

$$|\vec{B}| = \frac{|\vec{E}|}{c}, \tag{1.2}$$

where c is the speed of light. Given this relation, it is sufficient to only use the expression of the electric field of light and neglect the magnetic field in describing the interaction of electromagnetic waves with matter since the magnetic field component is 10^{-8} times smaller than the electric field component. Moreover, neglecting the spatial components of the electric field, we can describe the electric field of light using only its temporal dependence: $\vec{E}(x, y, z, t) = E(t)$.

Considering that $E(t)$ is a real quantity, its Fourier transform is given by:

$$E(\omega) = \int_{-\infty}^{\infty} E(t) \exp\Big(- i\omega t\Big)\, dt, \tag{1.3}$$

and as such, it must satisfy the relationship $E(\omega) = E^*(-\omega)$. This relation creates negative non-physical frequency components that carry no additional physical information as a mathematical artefact. For each positive $E(\omega)^+$ and negative $E(\omega)^-$ frequency components, there exists positive $E(t)^+$ and negative $E(t)^-$ temporal counterparts. Since these quantities are symmetric and can be obtained by taking simple Fourier transforms, knowledge of just one of them, e.g. $E(t)^+$, is sufficient to describe a pulse fully, such that $E(t) = 2\mathrm{Re}\{E(t)^+\}$.

The purpose of converting the real electric field $E(t)$ into a complex representation of the field $E(t)^+$ is twofold: 1) for mathematical convenience since $E(t)^+$ is considered the complex analytical commensurate of the real field $E(t)$, such that $E(t)^+ = E(t) + i\mathscr{H}\{E(t)\}$, where $\mathscr{H}$ is the Hilbert transform operator and 2) to allow for separating $E(t)^+$ into amplitude and phase terms. With that, we can finally write an expression for the field:

$$\begin{aligned} E(t)^+ &= \frac{1}{2}\mathcal{E}(t) \exp\Big(i \arg\{E(t)^+\}\Big) \\ &= \frac{1}{2}\mathcal{E}(t) \exp\Big(i[\omega_0 t + \phi(t)]\Big), \end{aligned} \tag{1.4}$$

here $\mathcal{E}(t)$ is the complex pulse envelope and the argument of $E(t)^+$ is decomposed into ω_0, which represents the carrier frequency and $\phi(t)$, which is the phase function. The complex envelope can take the shape of different functions, defining the overall profile of the pulse, e.g. Gaussian, hyperbolic secant, Lorentzian and so on.

1.1.1 Carrier frequency

The choice of carrier frequency ω_0 in equation (1.4) is commonly defined as the frequency at the pulse peak. This selection is somewhat arbitrary, especially in the case of uncompressed pulses, since it would yield different frequencies in the temporal vs. frequency domains. A more formal description would be the intensity-weighted average frequency, which yields a carrier frequency consistent in both domains:

$$\omega_0 = \frac{\int_{-\infty}^{\infty} |\mathcal{E}(t)|^2 \omega(t) dt}{\int_{-\infty}^{\infty} |\mathcal{E}(t)|^2 dt} = \frac{\int_{-\infty}^{\infty} |E(\omega)^+|^2 \omega dt}{\int_{-\infty}^{\infty} |E(\omega)^+|^2 dt} \tag{1.5}$$

1.1.2 Phase function

The phase function $\phi(t)$ in equation (1.4) can be Taylor expanded into:

$$\begin{aligned} \phi(t) &= \sum_{n=0}^{\infty} \frac{\phi^{(n)}(t-t_0)^n}{n!} \\ &= \phi_0 + \phi^{(1)}(t-t_0) + \frac{\phi^{(2)}}{2}(t-t_0)^2 + ... \end{aligned} \tag{1.6}$$

where the term ϕ_0 is referred to as the carrier-envelope phase (CEP). The CEP plays an integral role when defining ultrashort pulses since it details the position of the carrier field peak(s) with respect to the envelope maximum, as shown in Fig. 1.1a. The carrier field shown in orange has a CEP of zero, such that the peak of the carrier coincides with the peak of the envelope (one maximum), whereas the field shown in magenta has a CEP of $\pi/2$, such that the peaks of the field are offset by $\pi/2\omega_0$ (two maxima). For longer pulses, such as in Fig. 1.1b, the CEP does not play a big role.

The second term $\phi^{(1)}$ of the Taylor expanded phase function (1.6) yields a correction factor to the carrier frequency of the pulse, $\omega_0 + \phi^{(1)} = \omega_{\text{inst}}$, establishing a time-dependent carrier frequency. This time-dependent carrier frequency is commonly referred to as the instantaneous frequency of the pulse. The instantaneous frequency is a valuable concept when describing non-monochromatic fields, such as ultrashort pulses, since it refers to the frequency of an oscillation at a particular

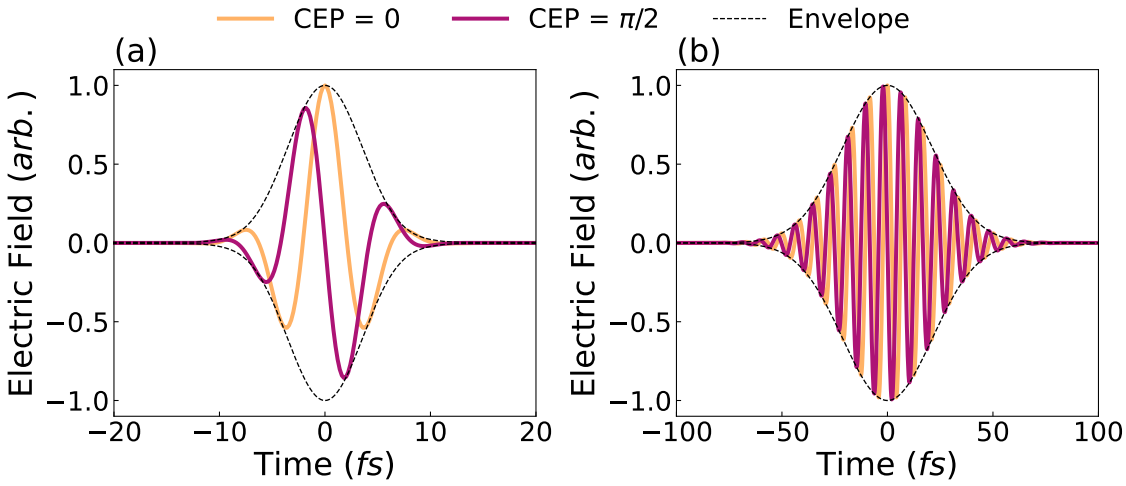

Figure 1.1: (a) Few-cycle 5 fs carrier fields with CEP = 0 (orange) and CEP = $\pi/2$ (magenta). (b) Multi-cycle 35 fs carrier fields with negligible CEP effect on the carrier shape under the envelope.

time t.

The third term ϕ_2 defines the chirp of the pulse, which describes whether the instantaneous frequency linearly increases (or decreases) as a function of time in the form $\omega_{\text{inst}} = \omega_0 + at$. Pulses acquire linear chirp as they propagate through transparent media (e.g. air, glass... etc.) due to chromatic dispersion. With sufficient power, higher-order phase terms proportional to t^n, where $n = 3, 4...$, arise due to nonlinear interactions with the transparent medium, such as the Kerr effect. Note that linear chirp is not the only form of chirp that can exist, more complex functions of t exist, e.g. exponential chirp.

For any given pulse, the minimum pulse duration (i.e. a compressed pulse) is achieved when $\phi^{(1)}... \ \phi^{(n)} = 0$. This condition corresponds to a constant instantaneous frequency in time equal to the carrier frequency ω_0 and equivalent to a constant spectral phase for all frequencies contained in the pulse spectrum.

1.1.3 Pulse intensity and duration

As mentioned, pulses with sufficient power or intensity can induce nonlinear interactions between the field and the medium. For this reason, an accurate definition of pulse intensity as a function of time is imperative for all practical applications.

Intensity, or power per unit area, is defined as the time average of the modulus square of the electric field over one period as follows:

$$\begin{aligned} I(t) &= \epsilon_0 nc \int_{t-T/2}^{t+T/2} \frac{1}{T} |E(t)|^2 \, dt \\ &= \frac{1}{2} \epsilon_0 nc |E(t)|^2, \end{aligned} \tag{1.7}$$

where ϵ_0 is the permittivity of free space, n is the refractive index of the material, c is the speed of light and T defines one period of oscillation. From the pulse intensity, we can define the duration of the pulse τ_p as the full width at half maximum (FWHM):

$$\tau_p = \mathrm{FWHM}[I(t)] \tag{1.8}$$

Analogously, a spectral width $\Delta\omega = \mathrm{FWHM}[I(\omega)]$ can be found from the spectral intensity. These two parameters are co-dependant since they are related to each other through the Fourier transform and define the minimum duration–bandwidth product $\tau_p \Delta\omega = 2\pi a_{FTL}$. The parameter a_{FTL} depends on the shape of the pulse (Gaussian, hyperbolic secant... etc.). It is worth noting that the shorter the pulse, the more difficult it is to define its characteristics in full detail. Furthermore, in the case of few-cycle pulses, the definition of an envelope becomes irrelevant and measuring the carrier field is necessary to measure the pulse. The most common and simplest tool of characterisation is the intensity autocorrelation of the pulse.

Note that in a laboratory, the measured power delivered by the pulse is not instantaneous. Instead, it is the time-averaged power of the entire pulse (envelope), measured by a photodiode or a photomultiplier, by integrating over the beam cross-section. In the teraherz and petaherz frequency domains, devices such as photodiodes cannot measure the fast carrier oscillations since the temporal response of such devices needs to be shorter than a half-cycle $\tau_{resp} \leq \pi/\omega_0$ to resolve them. The typical response time is in the range of picoseconds, making the process of resolving femto- and attosecond pulses a more sophisticated ordeal. For more details on the topic of photonics and nonlinear optics, excellent references such as [47–49] can be consulted.

1.2 Light-matter interaction

So far, only the temporal characteristics, and through the Fourier transform, spectral, of pulses have been discussed. In this section, the interaction of pulses with matter, limited to solid-state media, is addressed. Within a medium, light pulses interact with a very large number of particles. For example, 1 g of quartz contains

$\sim 10^{22}$ oxygen atoms. This large number of atoms allows for some leniency by excluding the individual motion of each particle and assuming that the summed-up macroscopic behaviour, represented by a material response function, effectively describes what happens when light and matter interact.

A wave equation for the electric field of light in regions of space that contain no free charges $\rho = 0$ and no free currents $\vec{J} = 0$, e.g. large bandgap solids at room temperature, can be derived from Maxwell's equations (1.1):

$$\left(\nabla^2 - \frac{1}{c^2}\frac{\partial^2}{\partial t^2}\right)\vec{E}(x,y,z,t) = \mu_0 \frac{\partial^2}{\partial t^2}\vec{P}(x,y,z,t), \tag{1.9}$$

here, μ_0 is the magnetic permeability of free space, and $\vec{P}$ is the polarisation, which contains information on the medium's response and its influence on the electric field of light. The time-dependent polarisation can be further decomposed into linear and nonlinear contributions: $\vec{P} = \vec{P}_L + \vec{P}_{NL}$, differentiating the two different light-matter interaction regimes. When light impinges on a medium such as a solid, two main forms of interactions occur: firstly, absorption of photons and secondly field-induced driving of charged particles in the medium. Below follows a detailed description of light-solid interactions.

1.2.1 Electronic bands

Solids form energy bands $E_n(\vec{k})$, rather than energy orbitals (like atoms), following the Tight Binding Model due to the quantum interaction between the tightly packed atoms comprising the solid itself [50, 51]. The mathematical formalism of the model is based on an approximate set of wave functions originating from the superposition of the individual wave functions of the isolated atoms located at each atomic site in the solid. The framework takes into account the overlap of the localised atomic orbitals, which results in a broadening of the discrete levels, leading to the formation of energy bands within the solid.

Each electronic band spans a specific bandwidth, which is controlled by the parameters of the solid itself, defined by the atomic separation a which describes the degree of overlap in the atomic orbitals. The electrons within the bands form delocalised states spreading over many atoms and possess the translational invariance of the crystal, defined by a translational vector $\vec{R}$ such that $u(\vec{r} + \vec{R}) = u(\vec{r})$. This follows from Bloch's Theorem [52], where the wave function ψ of the electrons can therefore be written as a product of a plane wave and an envelope function that has the periodicity of the crystal lattice:

$$\psi_n(\vec{r}) = \exp\left(i\vec{k}\cdot\vec{r}\right)u_n(\vec{r}), \tag{1.10}$$

where $u(\vec{r})$ is the periodic function with the same periodicity as the crystal lattice and the exponential term is that of a plane wave. For each value of $\vec{k}$, there exist multiple solutions, n, to the Schrödinger equation which amount to the number of possible energy levels of the solid. Each of these energy levels $E_n(\vec{k})$ evolves smoothly with changes in $\vec{k}$, forming the dispersion relation of the electrons in that band.

1.2.2 Interband absorption

An optical transition or photo-excitation, whereby an electron absorbs a photon from an externally applied electric field, can occur between the energy bands provided that the transition is permitted by quantum selection rules. Since bands possess a bandwidth, interband absorption is possible over a continuous range of photon energies determined by the difference between the upper and lower energy limits of each band.

The optical transition of an electron from a quantum state ψ_i to a final state ψ_f is given by the transition rate $\Gamma_{i\longrightarrow f}$, known as Fermi's golden rule, derived from time-dependent perturbation theory. This rate quantifies the probability of a transition per unit of time and is equal to:

$$\Gamma_{i\longrightarrow f} = \frac{2\pi}{\hbar}|\langle f|H_p|i\rangle|^2 g(E), \tag{1.11}$$

where $g(E)$ is the joint density of states representing the number of initial and final states per unit volume that fall within continuous energy bands and H_p is the perturbation to the Hamiltonian due to the external electric field and is equal to $H_p = -\vec{p}\cdot\vec{E}_{ext}(t)$, where $\vec{p} = e\vec{r}$ is the dipole moment of the particle. This interaction permits an electron transition between the different bands in a solid, e.g. from the valence band to the conduction band in a semiconductor.

1.2.3 Intraband motion

For intraband motion, where the electron moves within a single band, the semi-classical description of light-matter interaction is more befitting. Here, the electric field is treated classically and the electrons in the medium are treated quantum mechanically. The predictions of the semi-classical model assume prior knowledge

of the band structure $E_n(\vec{k})$ of the material and relate the band structure with the response of the charged particles to externally applied fields.

For each charged particle in a medium, a position vector $\vec{r}$, a wave vector $\vec{k}$, and a band number n are assigned to describe its equations of motion as mentioned in equation (1.10). When an external, time-varying electric field $\vec{E}_{ext}(t)$ impinges on a medium, its overall effect is a displacement of the charges. From that, it follows that the velocity of the charged particle in momentum space is given by the group velocity of the wavepacket, which depends on the band structure $E_n(\vec{k})$:

$$\dot{\vec{r}} = \vec{v}(\vec{k}) = \frac{1}{\hbar}\nabla_{\vec{k}} E_n(\vec{k}). \tag{1.12}$$

The wave vector $\vec{k}(t)$ as a function of time describes the pseudo-crystal momentum, where forces are exerted only by external fields, and is given by:

$$\hbar\dot{\vec{k}}(t) = -e\vec{E}_{ext}(t) + \frac{1}{c}\vec{v}(\vec{k}) \times \vec{B}_{ext}(t). \tag{1.13}$$

Since the magnitude of $\vec{B}_{ext}(t)$ is significantly smaller than the magnitude of $\vec{E}_{ext}(t)$ as mentioned in equation (1.2), the effect of the magnetic field in equation (1.13) can be neglected. It is worth noting that only in regions where an energy band $E_n(\vec{k})$ is approximately parabolic, i.e. resembles that of a free charged particle, the wave vector $\vec{k}$ given in equation (1.13) is equal to the true momentum of a free particle with momentum $\vec{P} = \hbar\vec{k}$. Otherwise, the actual momentum of the charged particle is described by the total forces acting on the particle.

Solving (1.13), we obtain the following expression for the crystal momentum:

$$\vec{k}(t) = -[\vec{k}_0 + \frac{e}{\hbar}\vec{A}_{ext}(t)], \tag{1.14}$$

where k_0 is the initial crystal momentum of the charged particle and $\vec{A}_{ext}(t)$ is the vector potential of the externally applied field, i.e. the laser pulse. For more details on the topic of solid-state physics, excellent references such as [50, 51, 53, 54] can be consulted.

1.3 Experimental approaches for field resolved measurements

Field-resolved measurements pertain to the acquisition of temporally and spatially [8, 55] resolved data, providing a detailed and comprehensive picture of the electric

field of light under investigation. Over the years many techniques capable of characterising certain properties of ultrashort pulses, such as spectral phase, spectral amplitude and pulse duration, have been developed. These techniques rely on using the pulse to measure itself by exploiting nonlinearities induced by the pulses' interaction in a nonlinear crystal. The most widespread method for pulse characterisation in the time domain is Frequency Resolved Optical Gating (FROG) [56]. In a second harmonic FROG geometry, a pulse is split into equal copies of itself, forming two arms of an interferometer. One arm is delayed relative to the other using a mechanical stage. The pulses interact noncollinearly in a $\chi^{(2)}$ medium, and generate a second harmonic signal. The noncollinear geometry assists in spatially separating the generated second harmonic signal from the fundamental. This second harmonic signal is then recorded using a spectrometer, yielding an intensity spectrogram of the instantaneous frequency as a function of time. From the recorded spectrogram, the pulse duration, spectral amplitude and spectral phase can be extracted. However, the information provided by the FROG spectrogram is ambiguous and insufficient, since it leaves out a few integral pieces of information as discussed below [57].

To precisely describe the electric field of a pulse, a measurement technique must precisely describe three integral pieces of information about the pulse: firstly, the pulse arrival time t_0, secondly the carrier-envelope phase ϕ_0 of the pulse and lastly the pulse direction. As mentioned in Section 1.1, the field for a linearly polarised time-dependent electric field can be written as:

$$E(t)^+ = \frac{1}{2}\mathcal{E}(t)\exp\Big(i[\omega_0 t + \phi(t) + \phi_0]\Big) \tag{1.15}$$

The spectral representation of which can be obtained through the complex Fourier transform:

$$E(\omega)^+ = |\mathcal{E}(\omega)|\exp\Big(i\Phi(\omega)\Big), \tag{1.16}$$

where $\Phi(\omega)$ is the spectral phase.

From equation (1.15), it can be seen that a temporal translation of t_0 such that $E(t) \to E(t-t_0)$ corresponds to a phase rotation in the frequency domain $E_{t_0}(\omega)^+ = \exp(-i2\pi\omega t_0)E(\omega)^+$. It follows that the spectrum of the translated pulse, taken as the absolute value of the complex representation $|E_{t_0}(\omega)^+|^2 = \tilde{E}_{t_0}(\omega)^+ E_{t_0}(\omega)^+$, where $\tilde{E}_{t_0}$ is the complex conjugate of E_{t_0}, is identical to the spectrum of the original pulse before temporal translation. This introduces an ambiguity with regards to t_0, which cancels out since the spectral amplitude is the square of the field. Conventional short pulse characterisation techniques cannot measure the CEP ϕ_0 following the same reasoning, where the constant phase term ϕ_0 would cancel out due to mea-

suring the spectral amplitude. Furthermore, an entire reversal of the time axis of the pulse such that $E(t) \rightarrow E(-t)$ corresponds to the exact same spectral representation as $E(t)$. As a consequence, to retrieve the field of a pulse, determining the pulse arrival time t_0, the carrier-envelope phase ϕ_0 of the field, as well as the sensitivity to time reversal $t \rightarrow -t$, is imperative. It follows then that gating techniques that measure the intensity as a function of time, such as FROG, are incapable of measuring the electric field of light [56, 57]. If FROG is combined with a technique that can measure the CEP, such as Stereo ATI or electro-optic sampling [58], the electric field can be retrieved.

Many clever techniques for measuring the electric field of light have been developed in the past 45 years such as electro-optic sampling [34] and attosecond streaking [7, 8]. For the past twenty years, attosecond streaking has been the powerhouse of optical field resolved measurements, enabling the measurement of ultrafast dynamics of electron processes in atoms, molecules, and solids [9, 15, 18, 21] based on the principle of using a strong, ultrashort laser pulse to "streak" the motion of electrons in a sample. Although a powerful tool for characterising electric fields in the optical range, attosecond streaking is a difficult technique that relies on gate pulses in the extreme ultraviolet (XUV) or soft x-ray range. This limits the applicability of this technique since XUV and soft x-ray pulses require ultra-high vacuum infrastructure. On top of that, the XUV pulses must be synchronised with waveform-controlled strong-field probe pulses.

Given these considerations, compact and flexible alternatives operating in ambient conditions are highly sought-after. Nevertheless, the basic concept of field sampling techniques can be distilled into two main branches: techniques based on photon-photon interactions following the nonlinear response of a medium or techniques based on photon-electron interactions. An excellent overview of field sampling metrology can be found in this reference by Herbst, A. *et al.* [59]. Similar to FROG, these techniques rely on the concept of gating as well, however, they are capable of measuring the carrier field rather than the envelope. In the following sections, a detailed description of the techniques used in this thesis is discussed.

1.3.1 Electro-optic sampling

Electro-optic sampling (EOS) is a technique based on photon-photon interactions in a nonlinear medium. A short gate pulse interacts with a phase-stable test pulse in an electro-optic nonlinear crystal, causing a measurable polarisation rotation to the gate pulse as detected by an ellipsometer [38, 45]. The interaction yields unambiguous information on the electric field of the test pulse, which can be extracted directly from the recorded polarisation rotation of the gate pulse and the response

of the system.

EOS is best understood in terms of the Pockels effect for a THz test pulse, where the frequencies contained in the pulse are long compared to the gate pulse bandwidth. The test pulse introduces birefringence in the EOS crystal, leading to a delay-dependent polarisation rotation of the gate pulse, with the magnitude of the polarisation rotation proportional to the test field amplitude. For the detection of test pulses containing frequencies in the order of the bandwidth of the gate pulse, EOS is best described in the frequency domain [43]. In this case, depending on the interaction geometry, a sum frequency generation (SFG) or a difference frequency generation (DFG) takes place between a CEP stable test pulse and the gate pulse in the nonlinear crystal, creating a phase stable up- or down-shifted replica of the gate pulse. The SFG or DFG signal then spectrally interferes with the local oscillator (LO)[1]. Their interference results in a detectable, delay-dependent polarisation rotation of the gate pulse, which can be detected in a heterodyne[2] detection scheme by employing a bandpass filter, a Wollaston prism and a differential measurement using two balanced photodiodes. The signal measured by the photodiodes is given by:

$$\Delta I(t) \propto |E_{\mathrm{LO}}||E_{\mathrm{SFG}}| \sin\Big(\phi_{\mathrm{LO}} - \phi_{\mathrm{SFG}}\Big), \tag{1.17}$$

where $|E_{\mathrm{LO}}|$ is the amplitude due to the LO, $|E_{\mathrm{SFG}}|$ is the amplitude due to the SFG signal and the phase term $\phi_{\mathrm{LO}} - \phi_{\mathrm{SFG}}$ reflects the phase difference between the spectral components of the two amplitudes. Note that in equation (1.17) only a single sum frequency is considered, whereas a full EOS measurement integrates over all frequencies. A global phase shift, such as a shift in the carrier-envelope phase of the gate pulse does not influence the EOS signal measured by the photodiodes. However, higher-order terms of the spectral phase, such as chirp, can reduce the signal strength due to incomplete spectral interference.

An illustration of the EOS signal generation mechanism is shown in Fig. 1.2 in the case of SFG. A bandpass filter can be used to filter out a portion of the spectrum where the gate and SFG intersect, selecting photons that contribute to the EOS signal and blocking the rest of the photons contributing to noise. This has the benefit of enhancing the signal-to-noise ratio of EOS [37].

In this thesis, EOS is implemented as a benchmarking tool to measure and compare the electric field of pulses with two other field sampling techniques in both

[1] A portion of the gate spectrum that overlaps with the SFG or DFG signal spectrum.
[2] Signifies the involvement of more than one frequency.

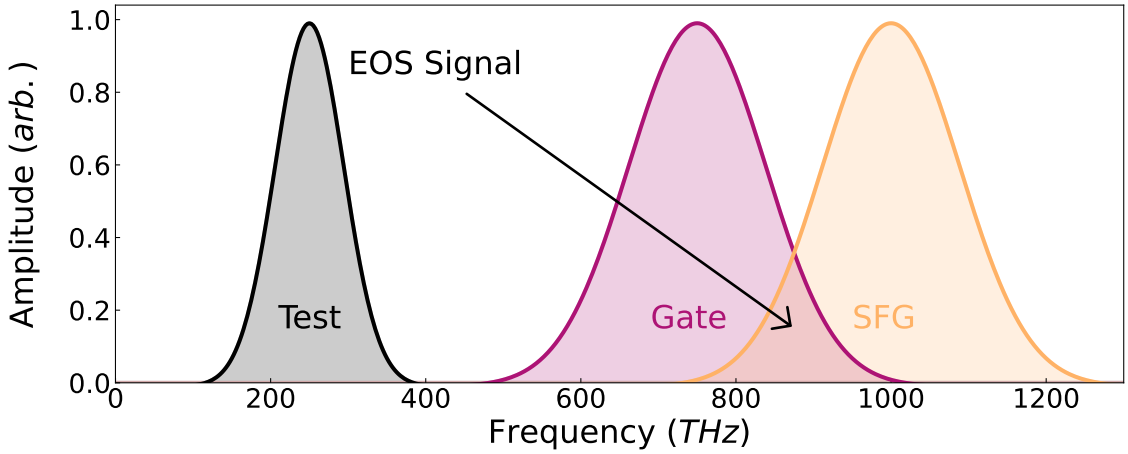

Figure 1.2: A general representation of EOS in the case of SFG between the test pulse and gate pulse. The arrow denotes the EOS signal, resulting from the spectral interference of the SFG and the LO.

Chapters 2 and 3. Note that in Chapter 2, the gate pulse is polarised on the ordinary axis of a beta-barium-borate (BBO) crystal and the test pulse is polarised on the extraordinary axis of the BBO crystal in a Type-II phase-matching configuration. The EOS signal emerges on the extraordinary axis, orthogonal to the gate pulse, and spectrally interferes with the LO. In Chapter 3, the gate and test pulses are polarised in the same direction on the ordinary axis of a BBO crystal, in a Type-I phase-matching configuration. The EOS signal emerges on the extraordinary axis and spectrally interferes with the LO. A Wollston prism set at 45° is implemented in both measurements to project the EOS signal and LO onto each other, resulting in a measurable change to the intensity of the LO due to the interference with the EOS signal. This change in intensity is detected by a pair of balanced photodiodes.

1.3.2 Photoconductive sampling

As the name suggests, photoconductive sampling measures the electric field of a test pulse based on photon-electron interactions. Typically, an ionising pulse termed the *injection pulse* impinges on a medium and abruptly changes the distribution of charges in it. This forms a short gating event that can be used to measure the electric field of another weak test pulse termed the *drive pulse*. The measurement is conventionally done by measuring a photocurrent in an external circuit, where the photocurrent is proportional to the vector potential of the driving pulse. There are two main flavours of this technique, based on the method through which the gating

event is generated: linear photoconductive sampling (LPS) [28, 31] and nonlinear photoconductive sampling (NPS) [23, 27, 60] as illustrated in Fig. 1.3 for solids.

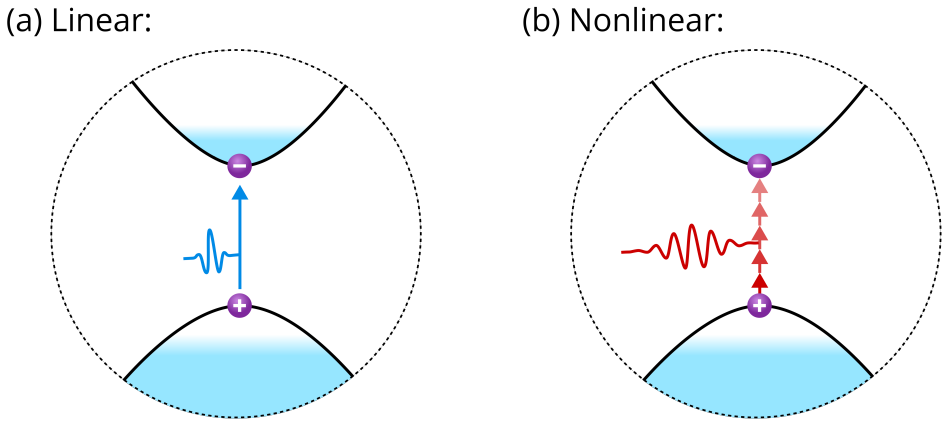

Figure 1.3: Injection mechanism in a solid. (a) Linear absorption of a single photon, shown here in reciprocal space for LPS. (b) Multiphoton absorption depicted in reciprocal space for NPS.

Both of these techniques rely on the master equation of photoconductive field sampling for measuring the field of the driving pulse. The measured signal or photocurrent is given by:

$$J(\tau) = -\int_{-\infty}^{\infty} dt\, A_{\text{drive}}(t) G_{\text{gate}}(t-\tau), \tag{1.18}$$

here, $A_{\text{drive}}(t)$ is the vector potential of the driving field and $G_{\text{gate}}(t-\tau)$ is the gating function, proportional to the rate of energy deposition in the medium. Note that the gate function must be confined to a temporal window shorter than one half-cycle of the driving field in order to resolve the drive field, and $\frac{d}{d\tau}J(\tau) = -A'_{\text{drive}}(\tau) = E_{\text{drive}}(\tau)$. The physical mechanism through which the gating event is created (linear or nonlinear absorption) is reflected in the form of the function $G_{\text{gate}}(t-\tau)$. For LPS, the gate function is given by the intensity of the injection pulse $G_{\text{LPS}} \propto I_{\text{injection}}$ whereas for NPS the gate function is given by $G_{\text{NPS}} \propto E^{2n}_{\text{injection}}$, where $2n$ represents the number of photons involved in the absorption process [27].

From the discussion above, several differences between the two gating methods can be deduced. For example, NPS relies on a strong field interaction (multiphoton absorption) to generate carriers in the medium [61] whereas LPS does not require an intense injection pulse as it generates carriers via single-photon absorption. Furthermore, LPS typically generates a gating event whose duration is in the order

of the injection pulse envelope. NPS on the other hand generates a gating event significantly shorter than the injection field duration due to the nonlinearity of the interaction. Fig. 1.4 illustrates the calculated difference between the ionisation rate of LPS and NPS for the same pulse plotted in Fig. 1.4a. It is evident from Fig. 1.4b and Fig. 1.4c that the energy transfer from the injection pulse to the medium occurs abruptly. In the case of linear injection, the gating mechanism is not temporally confined by nonlinearity, as evidenced by the spread of the injection rate. This places strict requirements on the injection pulse duration, where the injection pulse must be shorter than a half-cycle of the driving pulse following the Nyquist-Shannon sampling theorem [62]. In contrast, nonlinear injection utilises the nonlinearity of the interaction to confine the injection pulse in time. This confinement is clear in the case of four or eight photons, where the injection process is dominated by an extremely sharp, intense peak and negligible contribution from the two lobes before and after the central peak. For this reason, as long as the injection pulse is sufficiently intense, it can be used to detect the field of the driving pulse even if the duration of the injection pulse is more than the half-cycle of the driving pulse.

Using nonlinearity to confine the gate pulse in time is not without its own set of drawbacks, however. The spectral response functions of LPS and NPS display fundamentally different characteristics as a result of the differences between the two gating mechanisms. The spectral response can be approximated as the Fourier transform of the gating function, provided that the injection pulse shape is known [27]. An approximate response is thus calculated for an ultrashort 5 fs Gaussian pulse in the case of LPS and in the case of NPS. Since the gating event G_{LPS} is defined by the intensity profile of the gate pulse, the response function of LPS rolls off smoothly, with a cut-off frequency determined by the FWHM of the pulse at approximately 0.5 PHz as shown in Fig. 1.5. Moreover, if the CEP of the injection pulse is changed from zero to $\pi/2$ (cosine pulse to sine pulse), the intensity profile of the pulse is unchanged as shown in the inset of Fig. 1.5 and the response function is identical. For NPS, the situation is different, since G_{NPS} is proportional to E^{2n}. The response function rolls off smoothly only in the case of a cosine pulse with CEP = zero. If the CEP is changed to $\pi/2$, the spectral response becomes modulated due to the destructive interference of the spectral components from the two injection events (as shown in the inset).

Now that the short gating event has been created, the next step in the photoconductive sampling process is measuring the electric field of the driving pulse. In the case of solids, this is achieved by driving the generated carriers (electrons and holes) in their respective bands using the driving field, as mentioned in equation (1.13) [23,27,31]. This creates a macroscopic polarisation in the medium, which can

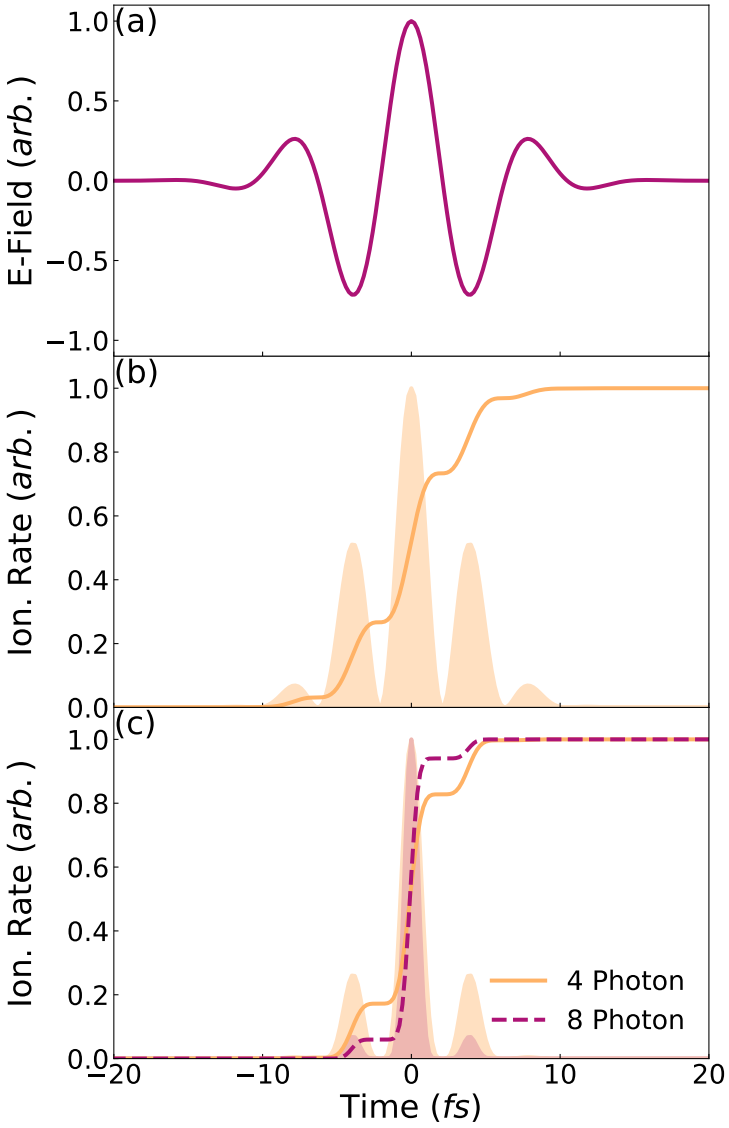

Figure 1.4: (a) Ultrashort injection pulse. (b) Injection rate of the pulse for linear ionisation. The shaded area represents the normalised intensity of the pulse. (c) Injection rate of the pulse for nonlinear ionisation with four photons (orange) and eight photons (magenta dashed). The shaded area represents the normalised intensity of the pulse.

be screened by a pair of electrodes in direct contact to the solid as shown in Fig. 1.6. The screening field on the electrodes generates a potential difference between the electrode and the ground of an external circuit, providing an electromotive force capable of driving a photocurrent between the two terminals. Thus a macroscopic

photocurrent can be measured as a function of delay between the injection and drive pulses, the magnitude of which can be discerned from the Ramo-Shockley theorem [63]. Considering that the mean free path of charge carriers in solids is usually in the order of a few tens of nanometers [64], and that the electrode separation is in the order of a few hundred microns, the macroscopic photocurrent signal obtained originates from the net displacement of charge carriers at the end of the driving pulse and not from electrons directly reaching the electrodes. It is worth noting that photoconductive sampling is not limited to solids and has been demonstrated in gases [65–67]. The difference between the photoconductive sampling process in solids or gas is the medium itself, the detection methodology remains the same.

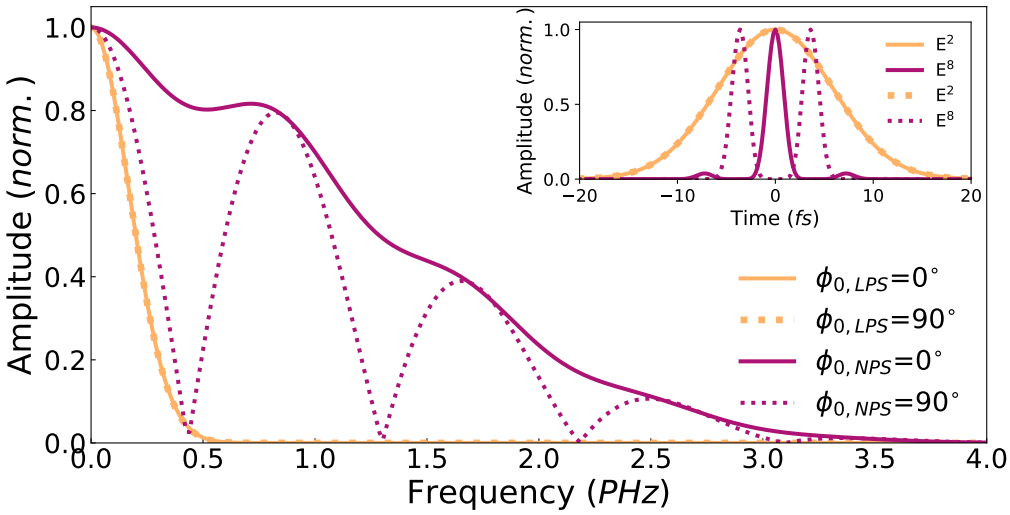

Figure 1.5: Comparison between the spectral response functions of LPS (orange) and NPS (magenta) for two different CEP values: zero (solid lines) and $\pi/2$ (dotted lines) for a 5 fs pulse centred at 400 THz. The inset depicts the amplitude of the gate functions in time. The spectral response is calculated by taking the Fourier transform of the traces in the inset. Note that all quantities are normalised individually for clarity.

In this thesis, NPS is implemented in Chapter 2 to measure the field of a mid-infrared (MIR) pulse centred around 150 THz using a 4.2 fs white-light pulse centred around 385 THz obtained via nonlinear broadening in a hollow-core fibre. LPS is implemented in Chapter 3 to measure an MIR pulse centred around 150 THz using a 2.6 fs visible-ultraviolet (VIS-UV) pulse centred around 666 THz obtained from a waveform synthesiser [39].

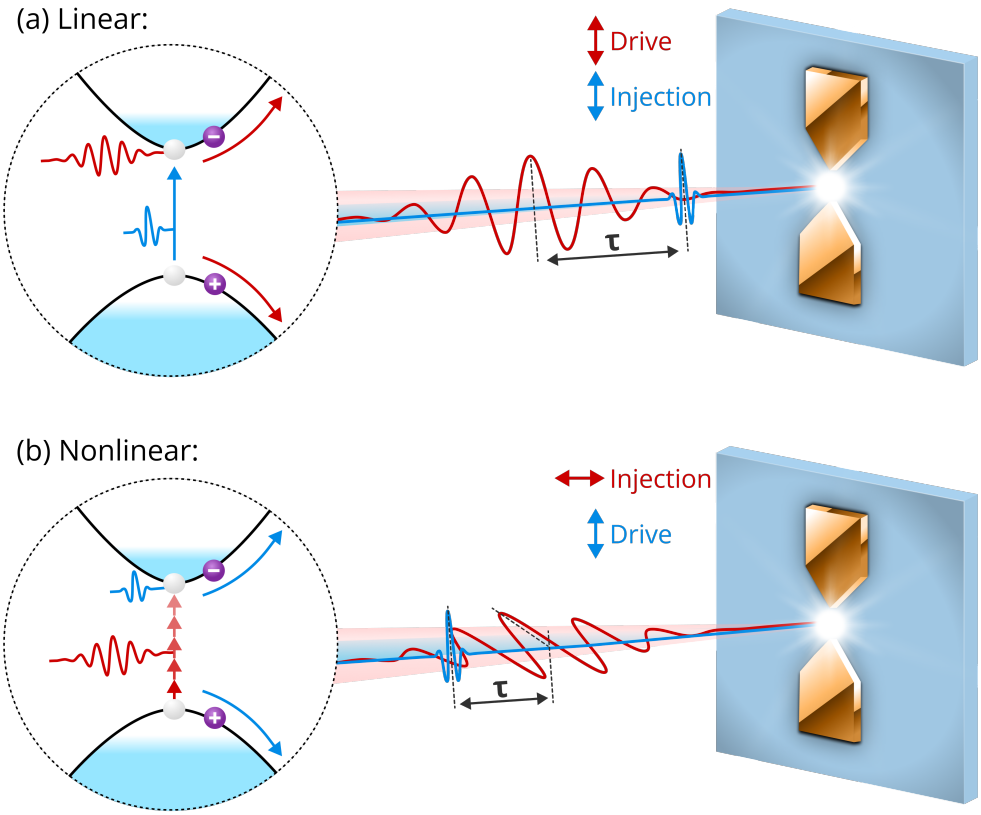

Figure 1.6: Schematic of photoconductive sampling. (a) In linear photoconductive sampling, single photons from the injection pulse (blue) are absorbed to create a short gating event. The drive pulse (red), delayed by τ with respect to the gating pulse, drives the carriers (purple) into their respective bands. (b) For nonlinear photoconductive sampling, multiphoton absorption from the injection pulse (red) creates a short gating event. The drive pulse (blue), delayed by τ with respect to the gating pulse, drives the carriers (purple) into their respective bands. The driving pulse in both cases generates a dipole inside the medium. Electrodes contacted to the sample detect and screen the dipole, if the electrodes are connected to a circuit, current proportional to the drive field flows through the circuit following equation (1.18). Note that for LPS the pulses can have the same polarisation, but for NPS the convention is to use orthogonal polarisations. The reason behind this lies in the injection mechanism, which, for NPS, relies on strong-fields. This means the injection pulse can both inject and drive carriers. By orienting the pulse orthogonal to the electrodes, the driven carriers do not contribute to the measured current.

Chapter 2

Nonlinear photoconductive sampling using heterostructures

The modern technological landscape is based on the utilisation of electronic devices fabricated from semiconductive materials, such as silicon, germanium, gallium-arsenide and indium-phosphide (InP). The first electronic device ever created was the diode, a two-terminal apparatus that facilitates the flow of current in a singular direction [68]. This unidirectionality enables electronic devices to control the flow of electrons and function as logical switches for electrical current, thereby enabling their use for information processing and computing. The efficiency of these semiconductor devices is determined by factors such as temperature, response time, carrier mobility and the speed at which they can switch the current on and off, as measured by the cut-off frequency metric. Many electronic devices have been refined throughout the years, an example of such are Field-Effect Transistors, which can switch the current at a rate of 10^9 per second (GHz). In recent years, High-Electron-Mobility Transistors (HEMT) based on InP surpassed their silicon-based counterparts reaching a cut-off switching frequency of 1.5 THz, enabling the first solid-state amplifier beyond 1 THz [69]. The idea behind HEMTs is: by employing a layered structure of semiconductors, heterojunctions form between the dissimilar bandgaps. By using a doped semiconductor in junction with an intrinsic semiconductor, excess carriers from the doped semiconductor diffuse into the intrinsic semiconductor. The diffused carriers then express high mobility since collisions between the carriers and the impurities or dopants used to create them can be avoided. Devices operating at such high speeds are integrated into all modern electronic equipment that is used on a daily basis. Nevertheless, the quest for more rapid switching and fast response times persists as necessitated by the progression of technology.

Ultrafast optoelectronics is a rapidly evolving field of science that combines the principles of optics and electronics to create devices that can convert between elec-

trical and optical signals with the goal of introducing fast electronic switching aided by ultrafast laser interactions [70]. Besides the application for ultrafast switching, the principles of intense light-matter interactions can be harnessed to construct optoelectronic devices that function as solid-state waveform detectors as mentioned in Section (1.3.2) [23, 27]. In this chapter, the principle of generating charge carriers using a femtosecond pulse is exploited to measure the electric field of a second test pulse. An ultrashort 4.2 fs pulse centred at 780 nm will serve as an injection pulse, rapidly creating charge carriers to sample the field of a 2.1 μm drive pulse. In the first Section (2.1), a theoretical model based on the propagation of Maxwell's equations in a medium explores the prospects of enhancing the signal-to-noise ratio of these optoelectronic devices based on the introduction of a heterostructure. In Section (2.2) the experimental apparatus is detailed, followed by Section (2.3), detailing the sample fabrication process. Section (2.4) presents the experimental results, where the heterostructure is benchmarked against fused silica. Finally, the concluding remarks (2.5) discuss the outlook.

2.1 Theory and simulations

The general mechanisms of ultrafast current generation have been addressed in Section 1.3.2. To understand the intricate details of light-matter interation, a number of open questions pertaining to optical-field-induced currents must be systematically tackled:

1. Where does the current form?

2. Would a heterostructure produce more electrons, similar to a HEMT?

3. Does having more electrons mean better signal?

Equation (1.9) forms the basis of light-matter interaction. To elucidate the answer to the first question, a modified Maxwell solver based on a version initially developed by Dr. Nicholas Karpowicz using the programming language `MATLAB` [71] is implemented to examine the evolution of the electric field and polarisation inside a medium. The model solves the differential equation (1.9) on a grid and calculates the electron density created by the field based on multiphoton absorption. The Runge-Kutta-4 (RK4) numerical method of solving differential equations is used [72]. The basis of the RK4 numerical method is: in each iteration, the derivative of the function[1] is evaluated four times, once at the initial point, twice at trial midpoints and once at a trial endpoint. This information is then used to numerically approximate

[1] Here the field and polarisation.

the solution to the differential equation, providing information on the field, the polarisation, and the electron density in the medium. The current density is then evaluated using the Drude model [73, 74], which states that:

$$J(t) = \frac{ne^2\tau}{m}\vec{E}(t), \tag{2.1}$$

where n is the electron density, e is the electron charge, m is the electron mass, τ is the mean free time between collisions, and $\vec{E}(t)$ is the electric field.

Current formation in bulk

To address the first question, a 9 fs linearly polarised supergaussian pulse of order 4, centred around 400 THz, is propagated through the medium. The pulse parameters are chosen for their similarity to experimentally available pulses from titanium sapphire amplifiers. The calculation is performed using a single-pulse NPS scheme, which employs a single pulse for the injection and drive of the charge carriers[2]. Fig. 2.1 illustrates the evolution of the current across a 1 μm thick fused silica sample. In fused silica, the pulse experiences a group velocity dispersion (GVD) of 40.44 fs^2 per mm, which remains a negligible quantity for a sample thickness of 1 μm. From the plot, it appears that the current initially accumulates on the surface of the sample. It then continues to dynamically change as a function of pulse propagation inside the sample. Note that the pulse is partially reflected by the second surface, which creates a ringing inside the sample. The cumulative current is shown after the passage of the injection pulse and subsequent settlement of the ringing (magenta solid). Previous experiments using step-like electrodes have shown that the total current reaches its maximum after a depth of 20 μm, beyond which the injection pulse disperses and the CEP changes from e.g. 0 to $\pi/2$ [75].

In an actual NPS measurement, where two pulses are utilised, one for injection and one for drive, the current I that plays a role in gating the drive field is the cumulative current generated inside the sample at t_∞ as shown in Fig. 2.2 and not the instantaneous current at t_0. This originates from the experimental technique itself, where the methodology dictates that the measured signal is averaged over some time, typically in the range of 300 ms. Therefore, the fast current oscillations occurring at the beginning do not contribute to the signal because they are averaged out. Note that the current occupies a few microns in the sample, as shown previously in Fig. 2.1, defining a skin-depth of a few microns that describes the extent of

[2] See Section 2.4.1

what effectively counts for gating in the context of field sampling [75, 76].

Current formation in a heterostructure

In answer to the second question, the same calculation is performed for a heterostructured sample, comprised of alternating 100 nm thick layers of silicon dioxide and silicon as shown in Fig. 2.3. It appears that the current accumulates at the interface between the two materials and mostly in silicon. This can be understood as a result of the different bandgaps: fused silica has a bandgap of 9 eV whereas the bandgap of amorphous silicon is 1.75 eV [77, 78]. Therefore, the ionisation cross-section is significantly larger in silicon. As shown in Fig. 2.4, the net current contributing to the gate function is mostly provided by silicon, with $I(t_\infty)$ for silicon orders of magnitude larger than $I(t_\infty)$ for fused silica. Consequently, the heterostructured sample does indeed boost the total current. Similar to the case of the bulk sample, a skin-depth defines the overall extent of the current contributing to the gating mechanism as seen in Fig. 2.3.

2.2 Experimental setup

2.2.1 FP2 Ti:Sa amplifier

The Femtopower 2 (FP2) laser system shown in Fig. 2.5 is an in-house modified version of a commercially available titanium-sapphire chirped pulse amplification system from Spectra-Physics (formerly Femtolasers). The first element of this system is a Rainbow 2 monolithic titanium-sapphire oscillator (Spectra-Physics), delivering a 78 MHz train of pulses centred around 780 nm and spanning approximately one octave. Paired with the CEP4 module (Spectra-Physics), the system delivers phase-stable [79] 350 mW pulses at < 6 fs. In preparation for chirped pulse amplification [80], the output of the oscillator is chirped using a bulk glass stretcher.

Next is the titanium-sapphire amplifier, which is a modified 9-pass titanium-sapphire system (Femtopower Compact Pro). After the fourth pass, the repetition rate of the laser is reduced by picking a train of pulses at 3 kHz using a pulse picker (BME Bergmann) for the subsequent amplification passes. For optimal manipulation of dispersion, the amplifier is also fitted with a DAZZLER (Fastlite) after the fourth pass. The output of the amplifier is then recompressed using a pair of custom transmission gratings (Fraunhofer IOF). Post amplification and recompression, the system delivers 20 fs, 2.5 W pulses centred at 780 nm, which are then sent into a neon-filled hollow core fibre (HCF) for spectral broadening. The 1.86 W, 400-1100 nm output of the fibre is further compressed using three pairs of custom chirped

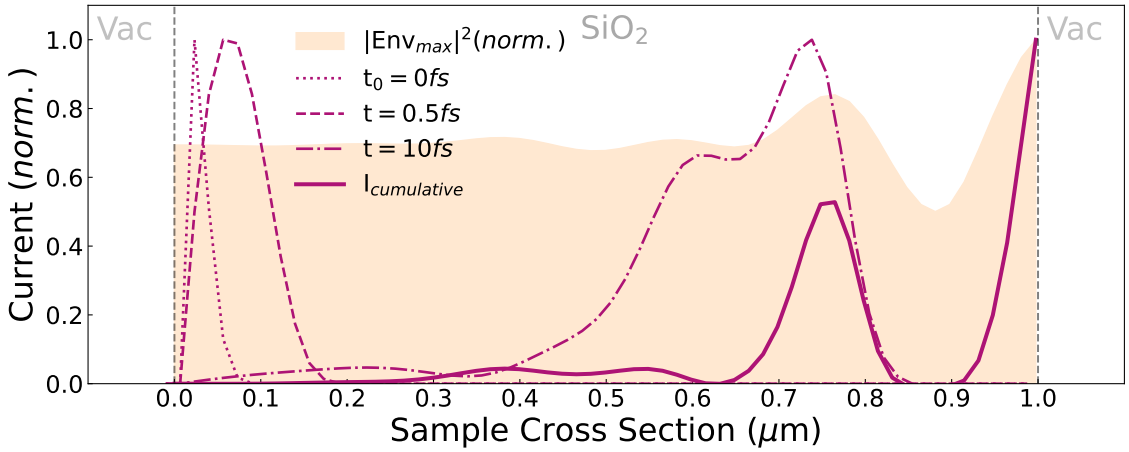

Figure 2.1: Calculated current generated inside a 1 μm thick silicon dioxide (SiO_2) sample. The shaded area (orange) represents the intensity maximum of the injection field. At $t = 0$ fs (magenta dotted), the current starts accumulating on the surface, the current increases for $t = 0.5$ fs (magenta dashed), and evolves as a function of time. After the pulse is gone and the ringing has subsided, the cumulative current is plotted in magenta (solid line).

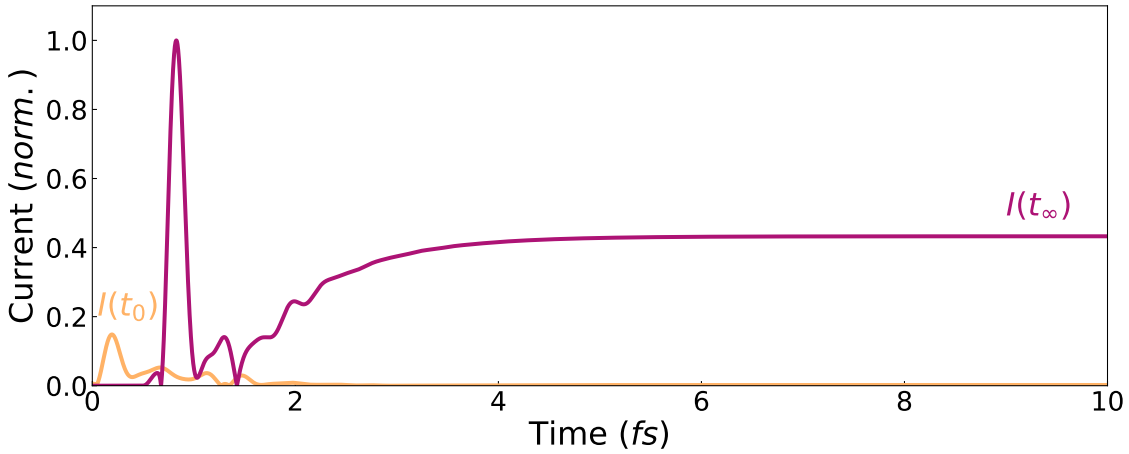

Figure 2.2: Current evolution as a function of time. The portion of the current that gates the driving field is given by the current at $I(t_\infty)$.

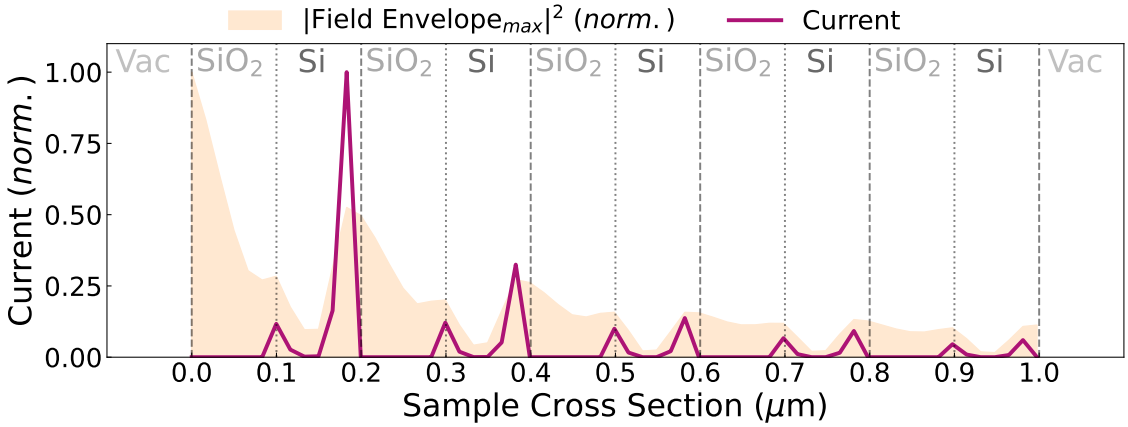

Figure 2.3: Calculated cumulative current (magenta) generated using a heterostructure comprised of alternating layers of silicon oxide and silicon. The shaded area (orange) represents the intensity maximum of the injection field.

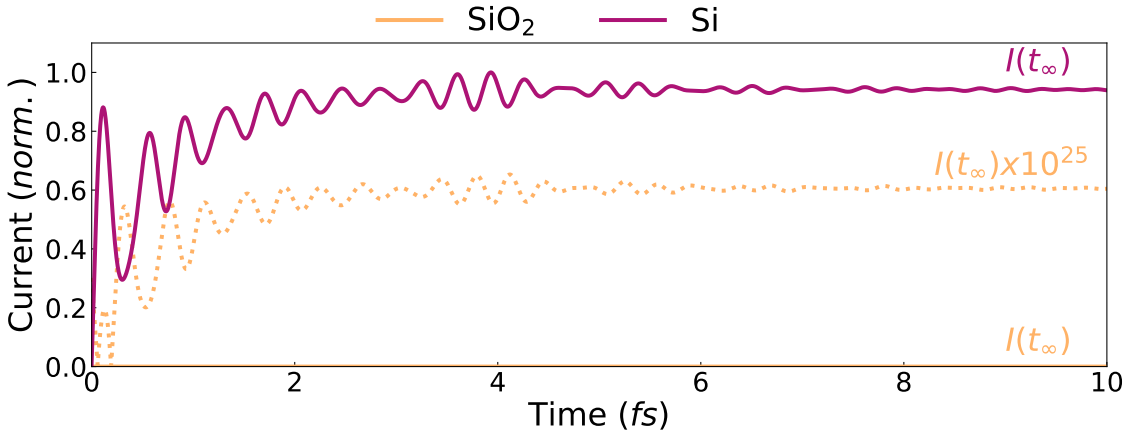

Figure 2.4: Comparison between the current generated in fused silica vs. the current generated in silicon inside the heterostructure sample. $I_{SiO_2}(t_\infty) > 0$, but when normalised to $I_{Si}(t_\infty)$, it is many orders of magnitude smaller. This indicates that most of the current is generated in the silicon layer.

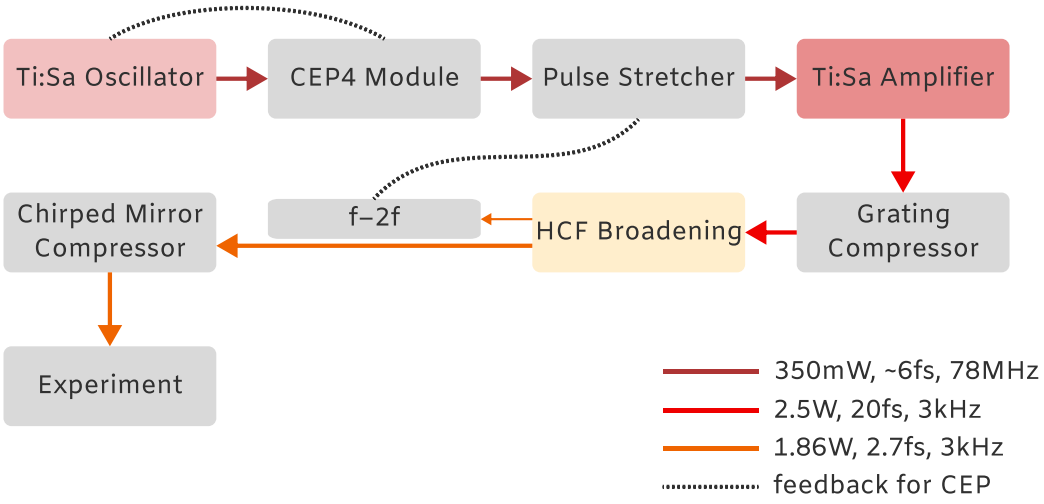

Figure 2.5: The FP2 laser system block diagram. Ti:Sa stands for titanium-sapphire. The hollow core fibre (HCF) is filled with 1.8 bar of neon for spectral broadening. The beam path is shown in red/orange. The dashed line represents feedback from the f-2f interferometer for CEP stabilisation.

mirrors (Ultrafast Innovations), 6 mm of fused silica and approximately 50 cm of air down to 2.7 fs FWHM pulses [27]. A small fraction of the fibre output is directed into a compact f-2f interferometer for stabilising the CEP of the amplified and broadened pulses [81]. The compressed 1.86 W white-light output from the HCF is directed into the experimental setup as shown in Fig. 2.6.

2.2.2 2-micron experimental setup

The experimental setup is comprised of a Mach-Zender-type interferometer with two arms: a drive arm and an injection arm as illustrated in Fig. 2.6. A portion of the power (3 mW) is split off by taking a reflection from the fused silica wedge pair used for fine tuning the compression to form the injection arm of the interferometer. The remainder of the power is utilised to generate 30 μW of 2.1 μm light in a 500 μm thick, Type-II BBO using intra-pulse difference frequency generation (iDFG), forming the drive arm in the experiments. A silicon wafer (Siegert Wafer) is employed after the BBO to remove the residual white-light, permitting only the orthogonally polarised 2.1 μm light to pass through. A thin 1 mm fused silica (FS) substrate is used for compressing the 2.1 μm output. Several wire-grid polarisers are utilised to control the power in each arm and a final wire-grid polariser is used for combining

the two orthogonal beams. A flip mirror is employed to direct the co-propagating beams into either detection setup, where the two field-detection techniques are compared: EOS and NPS.

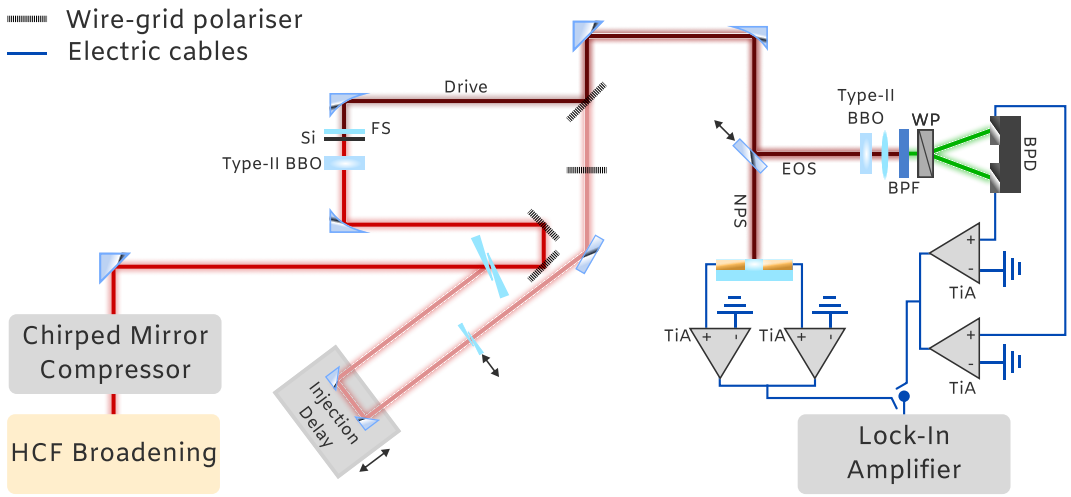

Figure 2.6: The 2.1 μm experimental setup. Post compression, the broadened HCF output is directed into the experimental setup. The beam is split into two arms, one for driving and one for injection (sampling), forming a Mach-Zender-type interferometer. The setup compares EOS and NPS. For more details on the setup, refer to the thesis by Mr. Muhammed Qasim.

NPS is performed for two samples, fused silica and an in-house manufactured heterostructured sample. Per sample, a full NPS measurement consists of measuring five consecutive traces for five injection power setting (total elapsed time is 75 min)[3]. The fused silica sample forms a standard against which the heterostructured sample is compared and the detected current signal traces out a waveform proportional to the vector potential of the field in question [27]. Due to the orthogonality of the beams, EOS is performed in a 500 μm Type-II BBO[4]. The reason behind using a relatively thick crystal for EOS detection is in order to increase the phase-matching length of the process, due to the relatively small 2.1 μm power. After the crystal, a 500-550 nm band-pass filter (Thorlabs) is used for filtering out the EOS signal. A Wollaston prism (WP, Thorlabs) is placed after the filter, which splits the EOS

[3] See Fig. 2.11.
[4] See the PhD thesis by Mr. Muhammed Qasim.

signal into its two orthogonal polarisation components. A home-built pair of balanced photodiodes receives and detects each polarisation component individually, such that a difference in the magnitude of each component would result in a measurable electric current signal. This current signal traces out a waveform proportional to the electric field in question.

Both detection techniques rely on using a transimpedance amplifier (TiA, DLPCA-200, FEMTO Messtechnik) for initially converting the current signal into a voltage, in addition to amplifying it. The amplified signal is then connected to a high frequency dual-channel lock-in amplifier (HF2LI, Zurich Instruments), triggered by an electrical signal synchronised with half the repetition rate of the laser (1.5 kHz).

2.3 Sample fabrication

The two samples used in this chapter are fabricated in-house. The heterostructured sample is fabricated by Dr. Volodymyr Pervak by alternately sputtering silicon and fused silica on top of a thin fused silica substrate. The electrodes are then applied at the Center for Nanotechnologies and Nanomaterials at the Walter Schottky Institute. Both steps are performed by means of physical vapour deposition using electron beams. To apply the electrodes, a mask laser-cut in the desired structure of the intended electrode geometry is mounted on top of the samples. The samples are then coated with a thin layer (5 nm) of chromium, followed by a thick layer of gold (150 nm). The chromium layer acts to bind the gold electrodes onto the samples.

2.4 Experimental results

2.4.1 Injection scan

To address the second question in Section 2.1, a single pulse injection scan is performed[5]. The experiment utilises a 4.2 fs pulse, centred around 385 THz, as illustrated in Fig. 2.7. The inset depicts the pulse spectrum. In an injection scan, a single pulse is applied to the sample, polarised parallel to the electrodes, as shown in Fig. 2.8. In reference to Fig. 2.6, the drive arm is blocked entirely, and the sample is oriented such that the electrodes are parallel to the optical table for a horizontally polarised[6] drive pulse. The pulse both injects and drives the carriers in the medium. A pair of motorised wedges in the beam path serve to alter the shape of the pulse

[5] Five scans are performed for eight power settings (total elapsed time is 44 min).
[6] In the laboratory reference frame.

via dispersion (both GDD and CEP change).

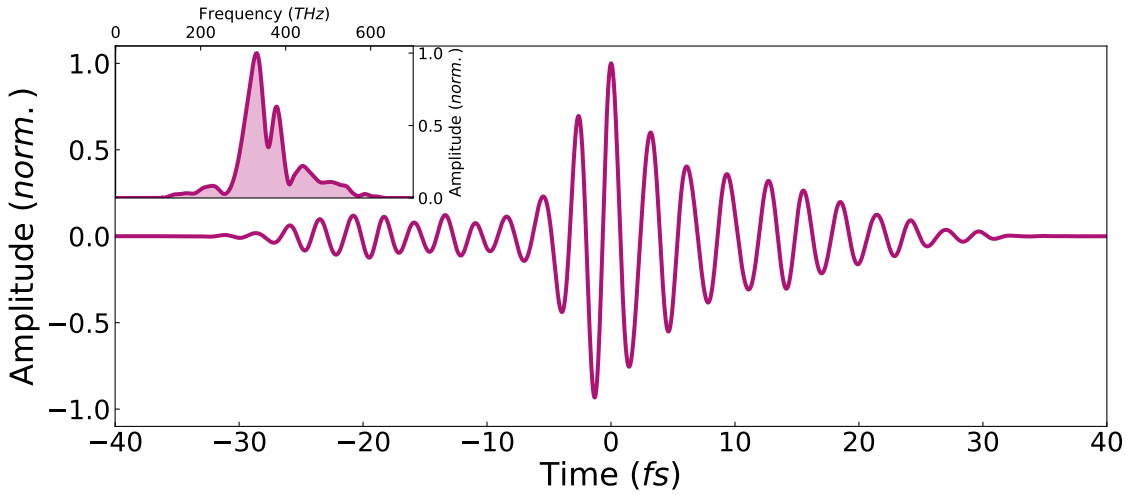

Figure 2.7: White-light injection pulse as measured via NPS in fused silica. The inset illustrates the spectrum of the injection pulse. Measurement and data courtesy of Mr. Muhammad Qasim, plotted with permission.

The measured current shown in Fig. 2.9 displays an oscillatory behaviour with respect to the wedge insertion Δx and is periodic with a CEP change of 2π in agreement with [23, 27, 82, 83]. The envelope of the oscillation exhibits a decrease in the magnitude of the current, which can be attributed to a decrease in the applied laser field strength due to pulse broadening. When compared to fused silica, it is evident from Fig. 2.9 that the heterostructure does indeed affect the net current as anticipated from the calculations performed in Section 2.1. With energies as low as 42 nJ seen in the inset of Fig. 2.9b, it is possible to detect some CEP-dependant current using the heterostructure. The maximum induced charge Q_{max} at $\Delta x = 0$ is plotted as a function of field strength in Fig. 2.10a for both the heterostructured sample and fused silica. A significant increase in the induced charge is observed in the heterostructured sample. For a field strength of $0.47\,\mathrm{V\AA^{-1}}$, the heterostructure yields 31× more current than fused silica. Note that the maximum charge will not continue to increase as a function of field strength due to optical breakdown of the samples.

With that in mind, the heterostructured sample unequivocally yields more current as expected. To extrapolate from Fig. 2.9b, using such sample permits measurements with pulse energies as low as 42 nJ, which is proximate to the pulse energies offered by commercially available solid-state oscillators. Similar to [24], a relative

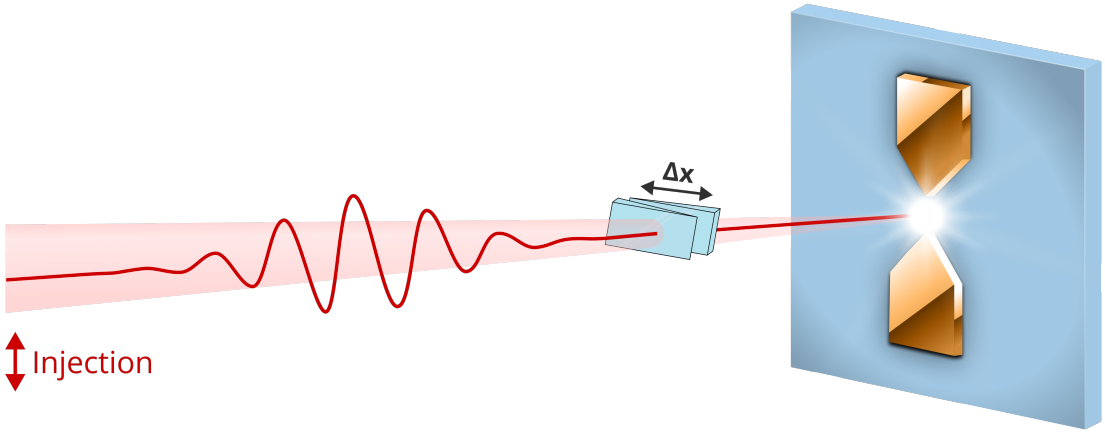

Figure 2.8: Single pulse scan utilising a single pulse for injection and drive. The pulse shape is modified by a pair of fused silica wedges on a moterised stage, altering its CEP and dispersion. The pulse polarisation is parallel to the electrode configuration.

shift in the zero-crossing of the injected current with respect to the wedge position is observed for the heterostructured sample, as a function of field strength. Fig. 2.10b plots the shift as a function of field strength. Considering that more current is generated, the heterostructured sample saturates and arrives at the desired detection regime earlier than fused silica [24, 82] or gallium nitride [25] as illustrated in Fig. 2.10b. Furthermore the relative variation in phase point-to-point is significantly smaller for the heterostructured sample as opposed to fused silica. Thus the utility of the heterostructured device, with an increase in current magnitude, and thereby sensitivity, lies within its applicability as a phase meter in reference to [24]. Such a device, once calibrated, could be implemented as passive phase detector in low energy systems. By monitoring the change in the magnitude of the current at a zero-crossing, information on the phase can be extracted. A shift in the magnitude would correspond to a shift in phase, and corrective measures could be applied.

2.4.2 NPS comparison

In this section, NPS measurements using fused silica and the heterostructured sample are performed and compared for different injection field strengths in answer to the last question in Section 2.1. The injection pulse is the same 4.2 fs pulse, centred around 385 THz depicted in Fig. 2.7. The drive pulse is a 30 μW, 2.1 μm pulse as illustrated in Fig. 2.6. The results of the measurement are plotted in Fig. 2.11, starting from an injection field strength of 1.1 VÅ^{-1} and down to 0.7 VÅ^{-1}, where based on Fig. 2.10, the first injection signal from fused silica is detected.

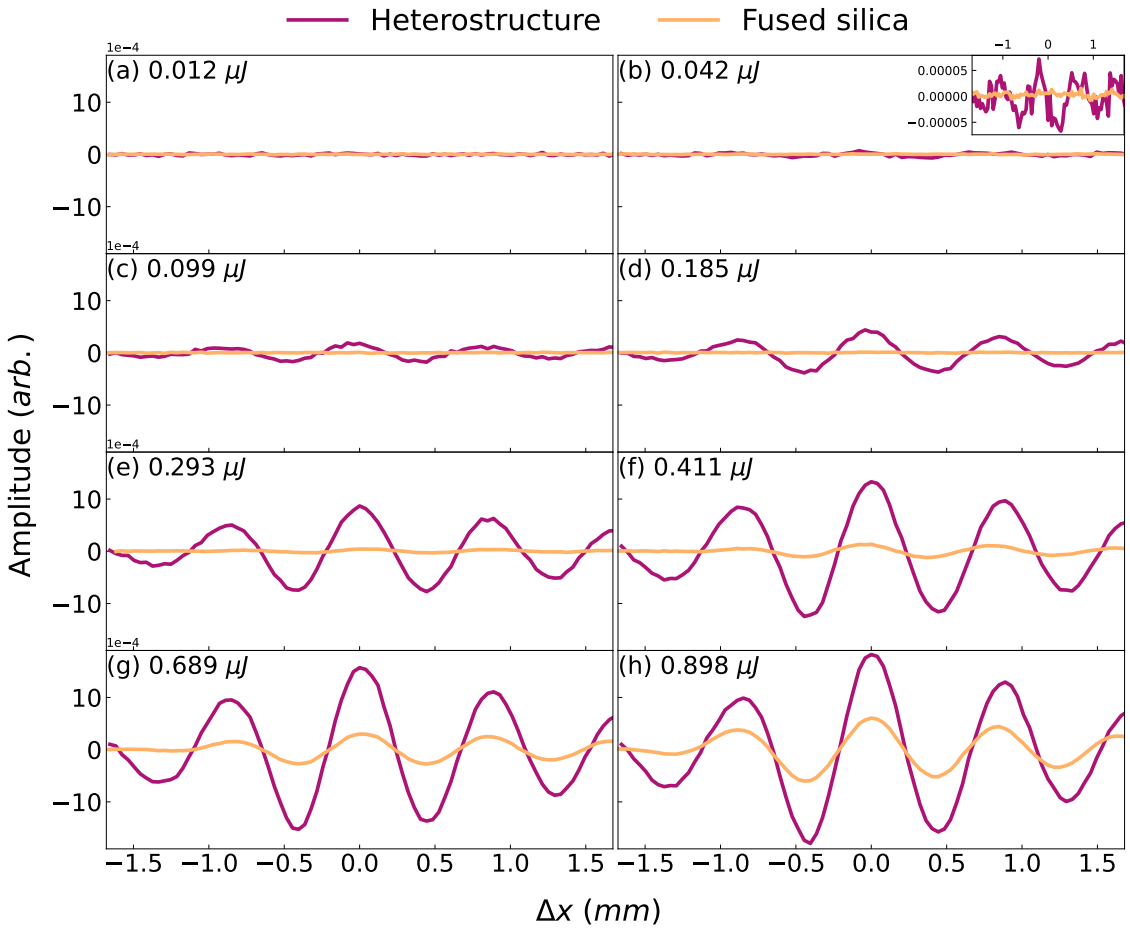

Figure 2.9: Current amplitude as a function of wedge position Δx. The laser power is increased in (a-h), while maintaining the same focal spot size of 45 μm. The results shown are an average of five measurements.

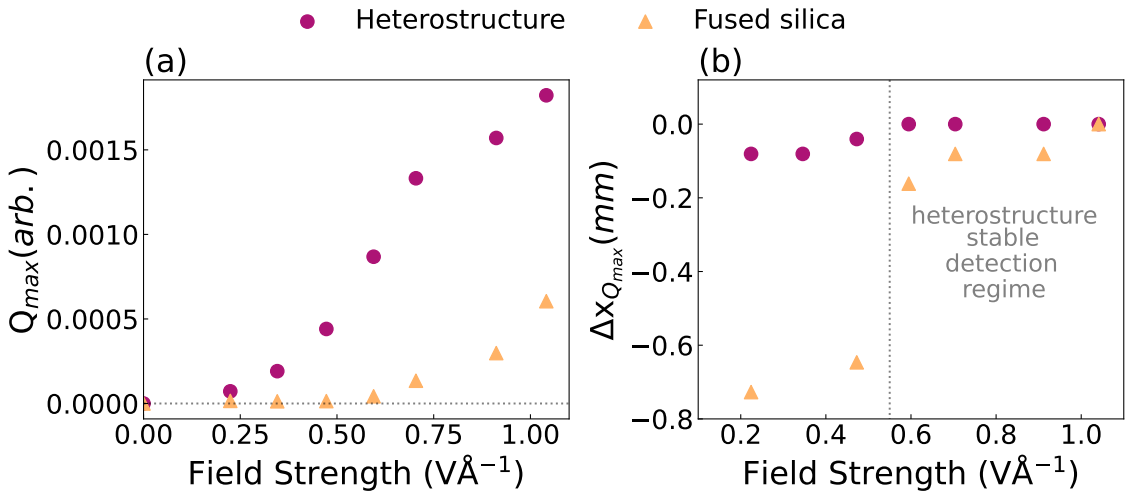

Figure 2.10: (a) Comparison between the maximum induced charge as a function of field strength at $\Delta x = 0$ for the heterostructure (circles) and fused silica (triangles). (b) Relative shift of the zero-crossing of the injected current as a function of field strength (max. field strength is used as a reference).

A cursory examination of Fig. 2.11a-e, reveals that there is no apparent difference in the magnitude of the 2.1 μm envelope maximum obtained by using the heterostructured sample under different injection field strengths. Conversely, in fused silica there is a marked correlation between the two, the scaling of which is plotted in Fig. 2.12. The figure depicts that the heterostructured sample had arrived at the saturation level earlier than fused silica, signified by the lack of variation in the magnitude of the envelope maximum, whereas for fused silica, this point occurs later at field strengths above 1 $\mathrm{VÅ}^{-1}$ in accordance with [24, 25]. This observation indicates that using the heterostructured sample for field sampling purposes is more instructive in systems offering less pulse energy, since the stable operation regime is established earlier.

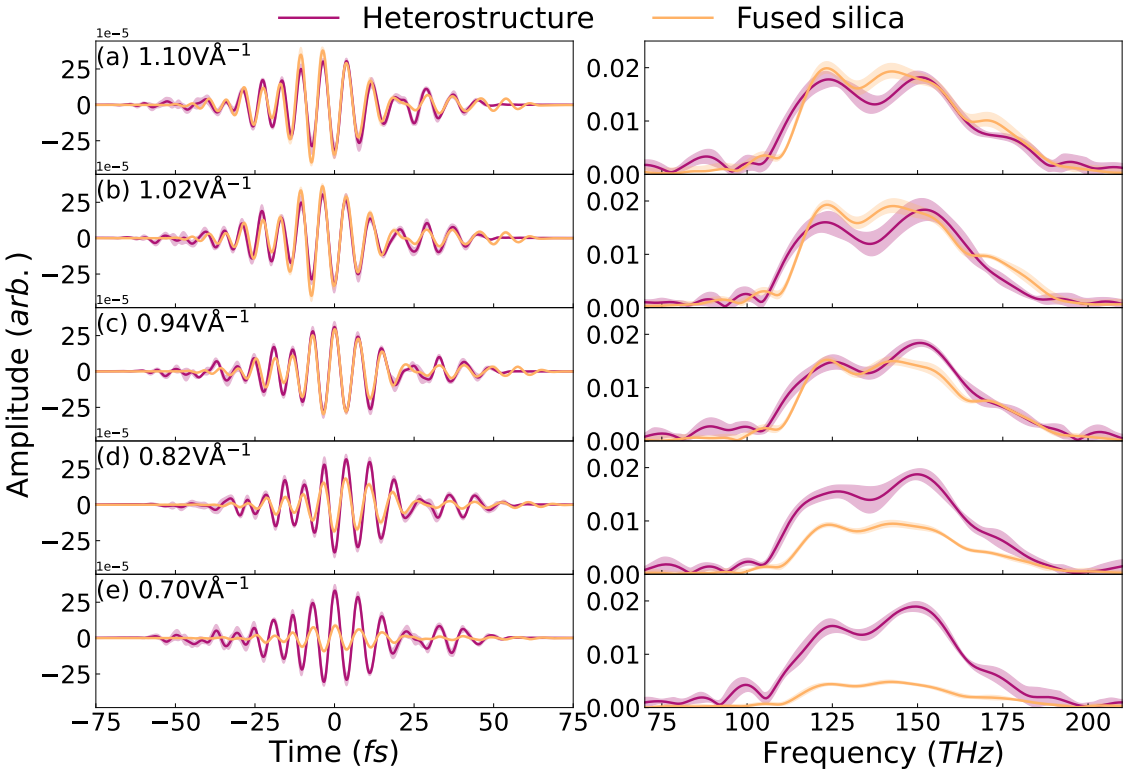

Figure 2.11: Left panel: waveform comparison between the heterostructured sample and fused silica for different injection field strengths. Right panel: spectra obtained from the waveforms for different field strengths. The shading represents the standard deviation of five measurements.

An estimate of the response function of the silicon layers in the heterostructured sample is shown in Fig. 2.13. The response is calculated by means of dividing the

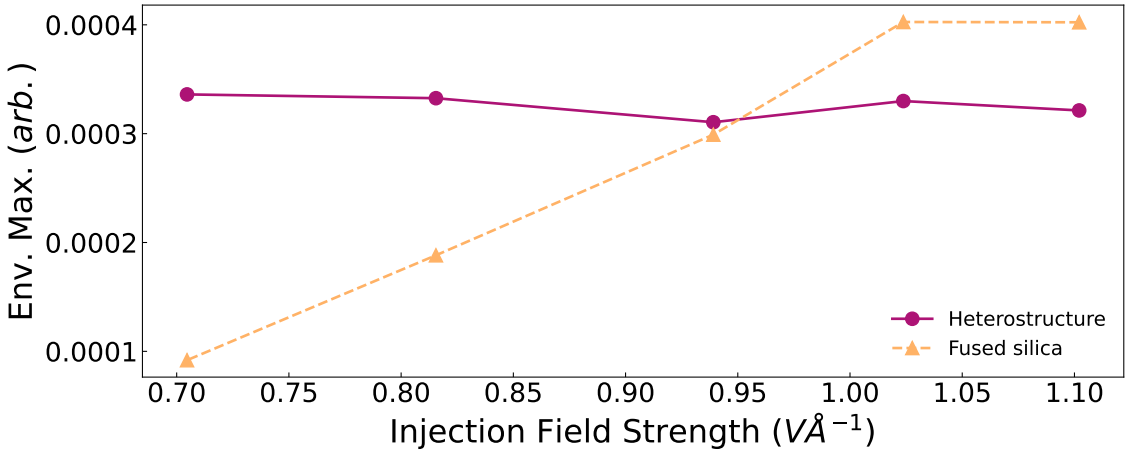

Figure 2.12: The envelope maximum of the 2.1 μm drive field is plotted as a function of injection field strength.

spectrum of the pulse as measured via the heterostructured sample by the pulse as measured using fused silica, effectively removing the contribution of fused silica from the total response function. Following Fig. 2.10, the response is calculated for a field strength of 1.10 VÅ^{-1}, to ensure that both samples are in the same stable operation regime. It appears from the plot that the response due to silicon is relatively flat across the range of interest, indicating that silicon contributes minimally to the total response function. Note that obtaining the total response function of the heterostructured sample is extremely challenging and computationally expensive[7]. The reason behind this is that both silicon and fused silica structures are amorphous, which complicates the calculations as a result of noncrystalline structure and lack of symmetry. Therefore the effectiveness of the heterostructured sample as a field sampling device in low pulse energy systems at this present stage lends itself to referenced measurements, where the response of the system is subtracted in the data processing stage.

For completeness, Fig. 2.14 compares the 2.1 μm waveform as measured via NPS using fused silica and EOS. At first glance, the pulse measured via NPS appears shorter than the pulse measured via EOS. This observation is reflected in the overall width of the spectra obtained in Fig. 2.14b. This is indeed the case (pulse $\text{FWHM}_{NPS} = 16.7\,\text{fs}$ and $\text{FWHM}_{EOS} = 18.74\,\text{fs}$, FTL $\approx 13\,\text{fs}$) and is a result of the EOS sampling crystal thickness[8], which is considerably thick at 500 μm for broadband detection. The choice of a relatively thick crystal for detection is due to

[7] See Section 3.1 for more details on how the spectral response is calculated.
[8] See Section 3.3.3 for more details on why this happens.

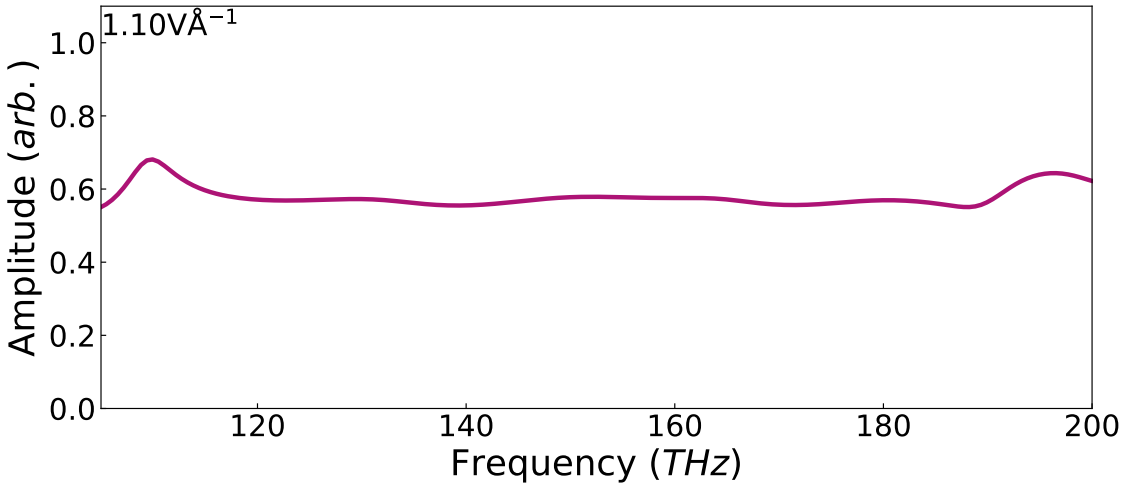

Figure 2.13: Estimated response of silicon in the heterostructured sample calculated by comparing the pulse spectrum as measured by the heterostructured sample to the spectrum measured by fused silica.

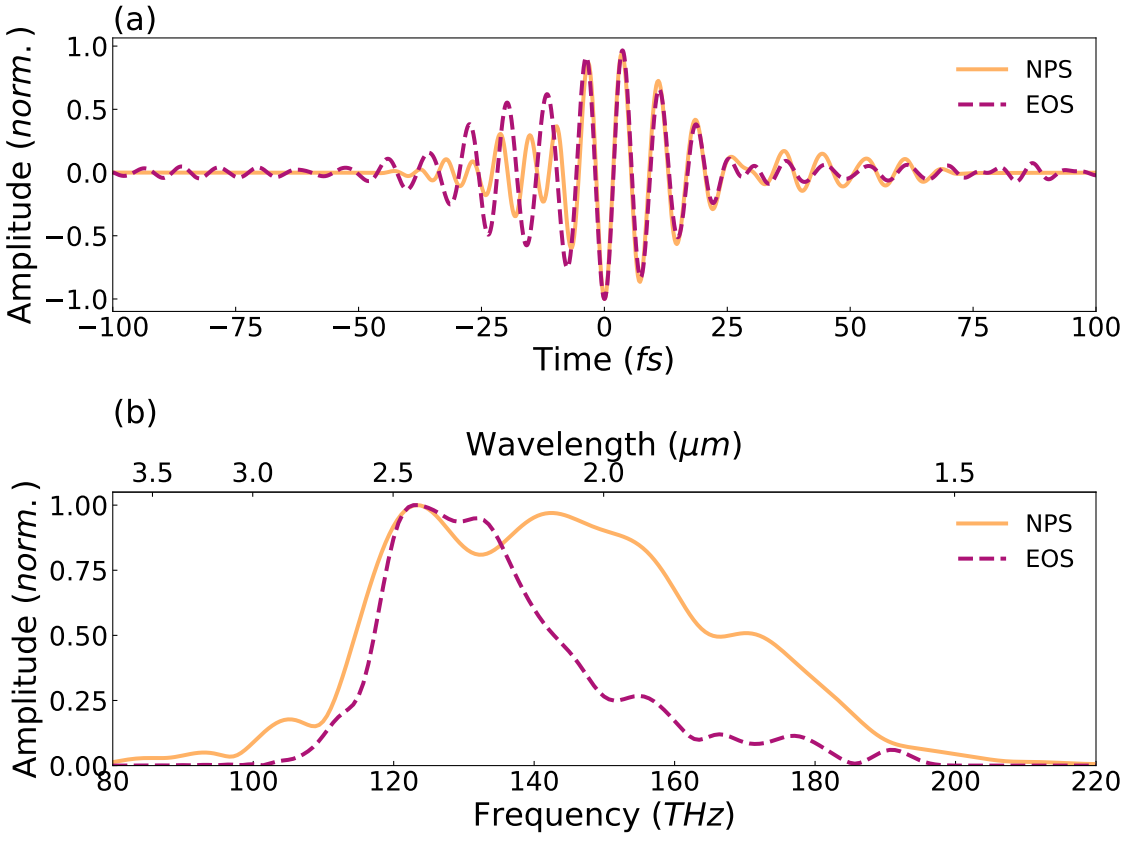

Figure 2.14: (a) The recorded waveforms of the 2.1 μm field as detected via NPS (orange) and EOS (magenta dashed). (b) Corresponding spectra of the waveforms recorded in (a). EOS data courtesy of Mr. Muhammad Qasim, plotted with permission.

the relatively small 2.1 μm power generated via iDFG. The EOS crystal thickness contributes to a reduction in the overall pulse duration, and thereby the measured spectrum, as a result of the interplay between phase-matching and temporal walk-off, which leads to less signal in the blue parts of the spectrum.

2.5 Concluding remarks

In this chapter, an optoelectronic device with an enhanced signal is presented. Due to the demonstrated increase in signal, the device has the potential of passively measuring CEP in low energy systems. The same device is also implemented in a field detection scheme, using two laser pulses. The device is structured in a fashion similar to HEMTs, using alternating layers of silicon and fused silica, where it is noted that the majority of the current is generated in the lower bandgap material.

In terms of electronic switching, in general, there are several physical limits that can impact the performance and efficiency of electronic switches, such as electron mobility, which typically decreases as a function of the bandgap of the material [84]. This limitation affects the lower limit of switching since a higher bandgap material would be capable of switching faster. It naturally lead to the concept of band engineering and HEMTs, which increase the mobility of electrons by creating a two dimensional electron gas that can freely move when a voltage is applied to the material [54].

For optoelectronic devices, similar restrictions on band structure and energy bandwidths exist [31] and development of new technologies is underway, particularly on-chip devices requiring low pulse energies by exploiting field enhancement in nanostructures [85]. As demonstrated, the device presented in this chapter offers a significant increase in the magnitude of the measured signal, and is beneficial for systems with low pulse energy, such as oscillators, offering a step forward in the direction of field detection using affordable and less complicated laser systems [86]. Next steps include validating the operation of the device using a commercial oscillator. Since this device is fabricated based on pulses from a modified commercial titanium sapphire laser, extension and thorough optimisation of the concept for other wavelengths and laser systems is necessary.

Chapter 3

Broadband linear photoconductive sampling

In the preceding chapter, the concept of NPS was presented as a method that enables field sampling through the creation of an extremely short event in time, namely the abrupt alteration in the carrier density within a medium, through the process of multiphoton absorption. While highly successful in sampling fields from 60-1100 THz [27,65,66], NPS as a field sampling metrology technique has a few shortcomings. The technique requires waveform-controlled, strong-field injection pulses and extreme nonlinearities to sample fields, and accordingly, large laser amplifier systems and bulky apparatuses [85, 86]. Moreover, since the technique is based on nonlinear injection, the residual injection field may drive the injected carriers [31]. For this reason, the injection field polarisation is typically oriented perpendicular to the electrodes to separate the potential drive due to the injection pulse from the sought-after drive due to the driving pulse. Furthermore, as the process of NPS utilises multiphoton absorption to generate charge carriers, the resulting population of charges can be dispersed throughout the Brillouin zone in the case of solid-state systems, and distributed over multiple conduction bands, thereby preventing the possibility of obtaining accurate mapping of photon-electron interactions [31].

Linear photoconductive sampling techniques based on the Auston switch [28,29] circumvent these problems by relying on single-photon absorption to inject carriers. A method is presented in this chapter for the detection of broadband mid-infrared fields spanning more than one octave from 110 to more than 200 THz, based on linear absorption in gallium phosphide (GaP). The experiment relies on a three-channel synthesiser[1], where one channel—VIS-UV—is utilised for injection and another channel—MIR—is utilised for drive. On this basis, a GaP crystal is chosen for

[1] See Section 3.2.2.

single-photon absorption, considering that the bandgap of GaP matches the central frequency of the VIS-UV driving pulse (L-cut, direct band-gap 2.78 eV [87]). The results of this chapter closely follow Altwaijry, N. *et al.* [88].

3.1 Theory and simulations

In order to define the criteria for linear injection, the interaction of the VIS-UV pulse with GaP is modelled by solving the time-dependent Schrödinger equation using an initial GaP band structure following:

$$i\hbar\frac{d}{dt}|\Psi_{n\vec{k}}(t)\rangle = \left(\hat{H} + \frac{e}{m_0}\vec{A}_L(t)\cdot\hat{p}\right)|\Psi_{n\vec{k}}(t)\rangle, \tag{3.1}$$

Here, $\hat{p}$ is the momentum operator, $\hat{H}$ is the unperturbed Hamiltonian and $|\Psi_{n\vec{k}}(t)\rangle$ represents the system's wave functions in the basis of stationary three-dimensional Bloch states. The band structure is obtained from density functional theory by solving the Kohn–Sham equations using the Tran-Blaha exchange-correlation potential [89]. These calculations were performed by Mr. Muhammad Qasim using the ELK code [90]. In the basis of accelerated Bloch states, exciting an electron via a laser field from a valence band v to the lowest conduction band c at a time t can be expressed as the scalar product of the laser field and the dipole transition matrix element $\vec{F}_L(t)\cdot\vec{d}_{cv}(\vec{k}+\frac{e}{\hbar}\vec{A}_L)$. The matrix elements of the momentum operator $\vec{p}_{cv} = \langle c\vec{k}|\hat{p}|v\vec{k}\rangle$ are related to the dipole transition matrix elements following $\vec{d}_{vc} = -ie\hbar\hat{p}_{cv}/m_0(E_c - E_v)$. Fig. 3.1 illustrates the electric field and spectrum of the VIS-UV pulse measured via NPS [39]. The waveform of the VIS-UV pulse is utilised in the simulations, where the pulse is allowed to interact with GaP in the [111] crystallographic direction[2]. Equation (3.1) is then solved numerically, and the occupation probabilities are evaluated, from which the generated charge density is calculated [91].

By varying the field strength of the VIS-UV pulse, Fig. 3.2 is obtained. From fitting a polynomial proportional to F_L^{2n}, where F_L is the peak field strength of the VIS-UV pulse and n is the number of photons participating in the transitions, different injection regimes are obtained. For field strengths below 0.1 VÅ^{-1}, the carrier density scales with F_L^2 as indicated by the orange dashed line. In this regime, $n = 1$ and the injection process is mainly dominated by single photon absorption. Above 0.2 VÅ^{-1}, the process is now proportional to $F_L^{3.26}$ as shown by the magenta dashed line. This regime results in $n \approx 2$, for injection mainly dominated by two-photon absorption. To insure a linear injection process, the field strength of the VIS-UV

[2]Note that the crystal structure of GaP is cubic and therefore isotropic.

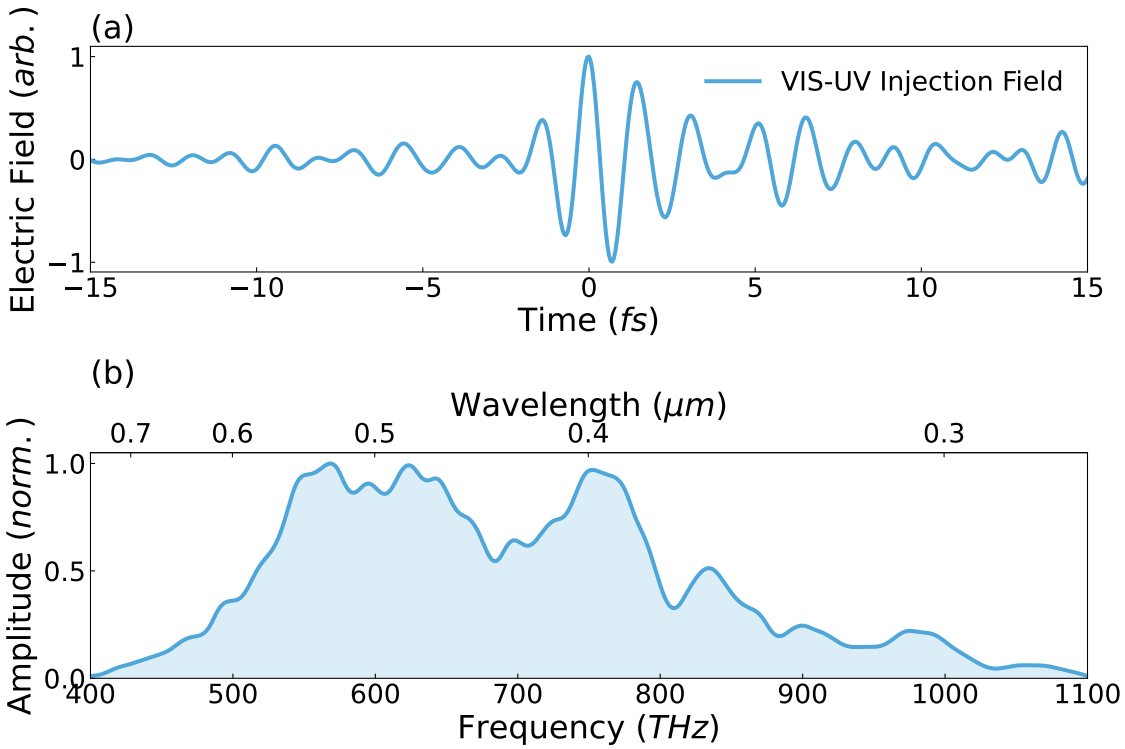

Figure 3.1: (a) The field and (b) the Fourier transform of the field of the VIS-UV injection pulse, which have been independently characterised by NPS [39].

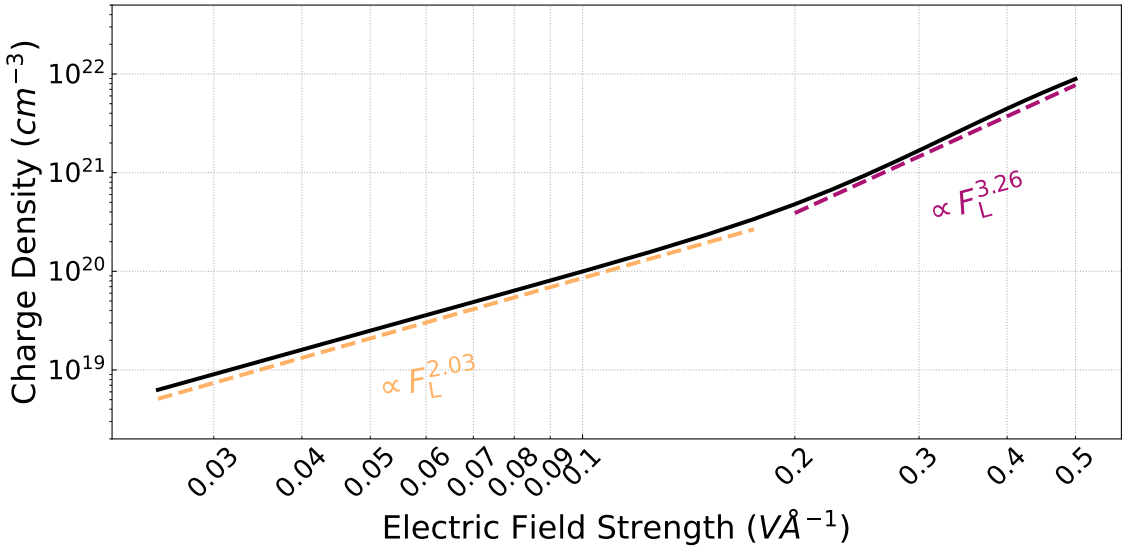

Figure 3.2: Calculated relationship between the VIS-UV field strength and charge density generated in GaP. In the regime depicted by the orange dashed line, the VIS-UV pulse injects the carriers linearly via single-photon absorption. The magenta dashed line highlights a two-photon injection process.

injection pulse is chosen and maintained at 0.08 VÅ^{-1} throughout the experiment.

3.2 Experimental setup

3.2.1 LWS1 regenerative amplifier and OPCPA

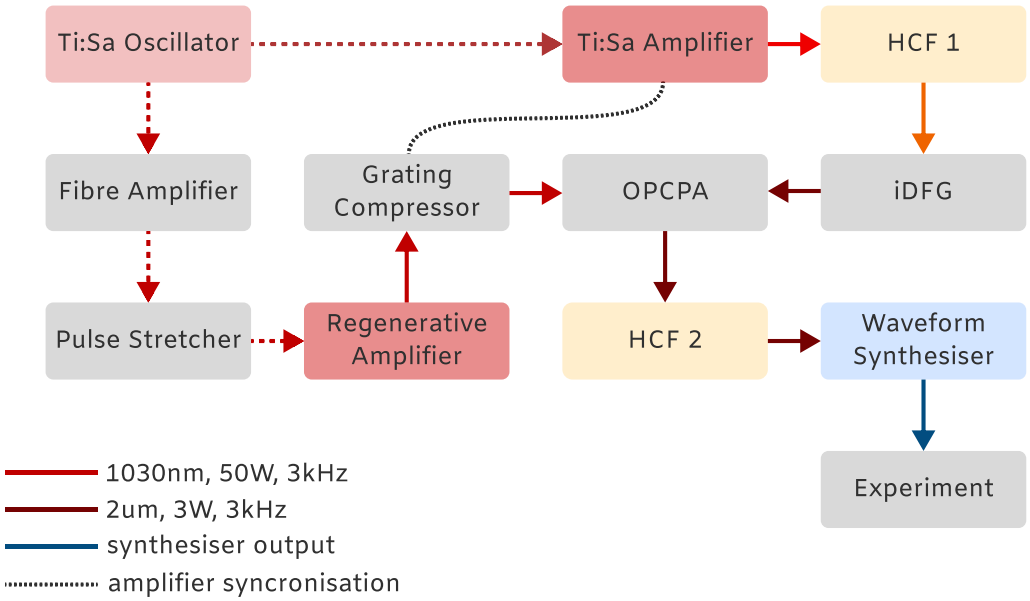

Figure 3.3: The LWS1 laser system. The Ti:Sa oscillator from Chapter 2 seeds both the FP2 and LWS1 systems with 78 MHz pulses. As a result of the amplification process, the output of both amplifiers is reduced to a repetition rate of 3 kHz using a Pockels cell (BME Bergmann) inside each amplifier. A portion (5%) of the Ti:Sa power is directed into HCF 1, filled with 2.3 bar of krypton. HCF 2 is air-filled, contains no windows and is and kept under ambient air conditions.

The lightwave synthesiser 1 (LWS1) laser system depicted in Fig. 3.3 is a home-built Yb:YAG thin disk (Trumpf Lasertechnik) regenerative amplifier, seeded by the portion of the spectrum centred around 1030 nm from the output of the Rainbow 2 oscillator mentioned in the previous chapter.

The seed is stretched to approximately 200 ps and then amplified to 25 mW (or

more) in a fibre amplifier, before being sent into the regenerative amplifier for amplification. The amplified output is then compressed using a pair of gratings (Fraunhofer IOF) in a reflection geometry, delivering 50 W, 1.4 ps pulses centred around 1030 nm. This output is utilised as a pump for an optical parametric chirped pulse amplifier (OPCPA) [92, 93]. To obtain the OPCPA seed, 5% of the power from the Ti:Sa amplifier (FP2) mentioned in the previous chapter is broadened in a krypton-filled hollow core fibre (HCF 1). The output is compressed using chirped mirrors (PC70, Ultrafast Innovations) and then focused into a 500 μm Type-2 BBO, where intrinsically phase-stable 2 μm pulses are generated via iDFG.

After two stages of amplification, first in periodically poled lithium niobate (PPLN) and then in a hybrid phase matching geometry using two BBO crystals, the dispersion is precompensated using a 1 cm thick sapphire block. The system delivers 1.6-2.5 μm, 15 fs long pulses with a power of 3 W, centred around 2 μm [93]. These pulses are then sent into an air-filled hollow core fibre (HCF 2) for spectral broadening from 0.3-3 μm. The three-octave spanning output of the fibre is then split into three parts for waveform synthesis [94].

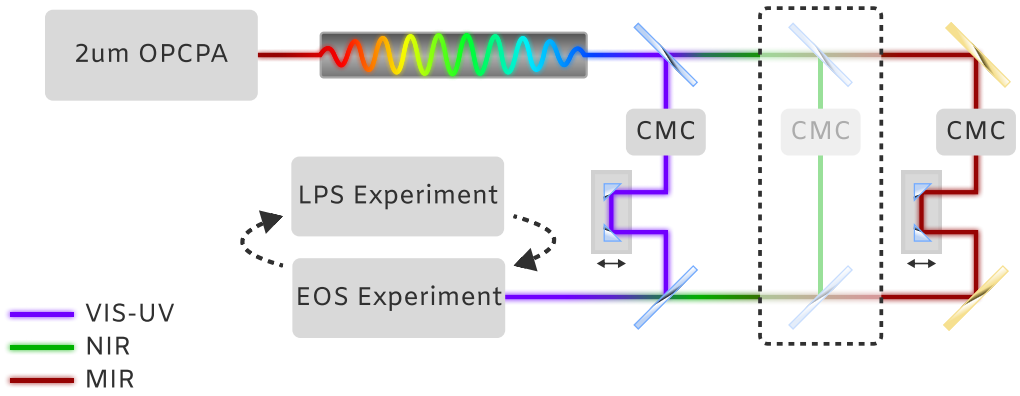

Figure 3.4: The synthesiser layout. Each channel is compressed separately using its own set of chirped mirrors (CMC). The channels form a three-arm interferometer, where each arm is fitted with a piezo stage (SmarAct) for precise waveform control. The shaded area is that of the NIR channel. This channel was not utilised in the this experiment.

3.2.2 Waveform synthesiser

As mentioned above, the three-octave output of the fibre is split into three equal parts using custom beam splitters, each containing one octave: 0.3-0.6 μm for the VIS-UV channel, 0.7-1.4 μm for the near-infrared (NIR) channel and 1.5-3 μm for the MIR channel as seen in Fig. 3.4. Each channel is individually compressed, using custom chirped mirrors manufactured in-house, down to 2.6 fs, 4.8 fs and 10.8 fs, respectively [39]. Due to the nature of the OPCPA and the nonlinear processes involved, compressing the MIR channel to its Fourier limit is challenging and maintaining a 10.8 fs pulse is subject to change on a daily basis based on alignment. The reason behind this is the fact that the spectral content of the MIR channel contains persistent pre- and post-pulses originating from the OPCPA that do not contain enough power for broadening in the air-filled HCF.

The VIS-UV channel depicted in Fig. 3.1 is utilised as a gate pulse in both LPS (injection pulse) and EOS. The MIR waveform constitutes the unknown waveform to be sampled. In the case of LPS, the MIR waveform is referred to as the drive pulse; in the case of EOS, it is referred to as the test pulse. The two channels, both polarised in the same direction, are combined using custom beam combiners [94] and then directed into the experiment.

The experimental layout, illustrated in Fig. 3.5, maintains identical experimental conditions for both sampling methodologies. The GaP and beta-barium borate samples are both kept in the focal plane of a 10.16 cm UV-enhanced off-axis parabola (Thorlabs). The measurements are conducted in succession, first, an EOS scan is performed, followed by an LPS scan. For EOS the signal is filtered using a bandpass filter (BPF) centred at 320 nm $\pm$ 30 nm. A magnesium fluoride Wollaston prism (Thorlabs) set at 45° is implemented to project the EOS signal onto the local oscillator for balanced detection[3]. In the case of LPS, the electrodes are connected to two transimpedance amplifiers (DLPCA-200, FEMTO Messtechnik) for converting the current signal into a voltage, in addition to signal amplification. The amplified signal is then connected to a high-frequency dual-channel lock-in amplifier (HF2LI, Zurich Instruments), triggered by an electrical signal synchronised with half the repetition rate of the laser (1.5 kHz).

[3]Note that BBO is a negative uniaxial crystal, with the following Type-I phase-matching condition: $n_e\omega_{SFG} = n_o\omega_{VIS-UV} + n_o\omega_{MIR}$.

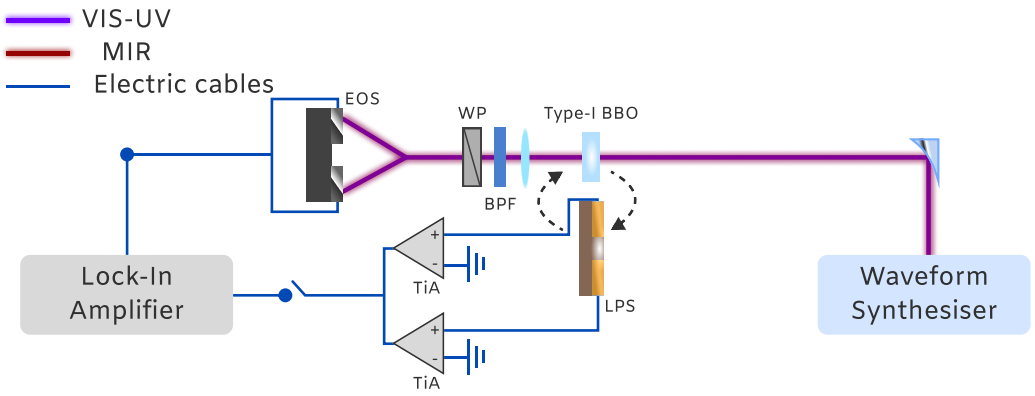

Figure 3.5: The LPS benchmarking experimental setup. The VIS-UV and MIR outputs from the synthesiser are used for electron injection and drive in a GaP sample, respectively. By doing so, the field of the MIR channel is sampled. The LPS measurement is then compared to EOS by using the channels to measure the field of the MIR channel by utilising the VIS-UV channel as a gate pulse and the MIR channel as the test pulse. TiA: Transimpedance Amplifier; WP: Wollaston prism and BPF: bandpass filter.

3.3 Experimental results

3.3.1 Benchmarking against EOS

This section tests the applicability of LPS as a waveform sampling technique against EOS. First, EOS is performed using a 5 μm BBO crystal in a Type-I phase-matching geometry, with the VIS-UV pulse serving as the gate pulse and the MIR field serving as the test pulse. Next, LPS is performed under identical experimental conditions by exchanging the EOS crystal with the LPS detection circuit. The results of the measurement are presented in Fig. 3.6a, depicting the waveform of the MIR field as measured via LPS (orange) and EOS (magenta dashed). The plot presented in the figure illustrates the mean of three waveforms recorded using LPS and five waveforms recorded using EOS. The standard deviation of the measurements is shown as the shaded area around the curves and indicates the measurements' variability. Note that in the case of LPS, the measurement integration time per delay step is 1 s and in EOS the integration time is 100 ms. In Fig. 3.6b, the absolute value of the Fourier transformed waveforms is depicted. The waveforms obtained through both techniques exhibit a notable degree of similarity, as indicated by a correlation

coefficient of r = 0.79[4], despite the distinct physical mechanisms through which the signals were obtained. Similarly, the spectra obtained through both sampling techniques display considerable overlap. To extract the shape of the MIR waveform in 3.6a, the spectral responses of the two measurements must be applied. The following sections address the methodology for obtaining the response functions.

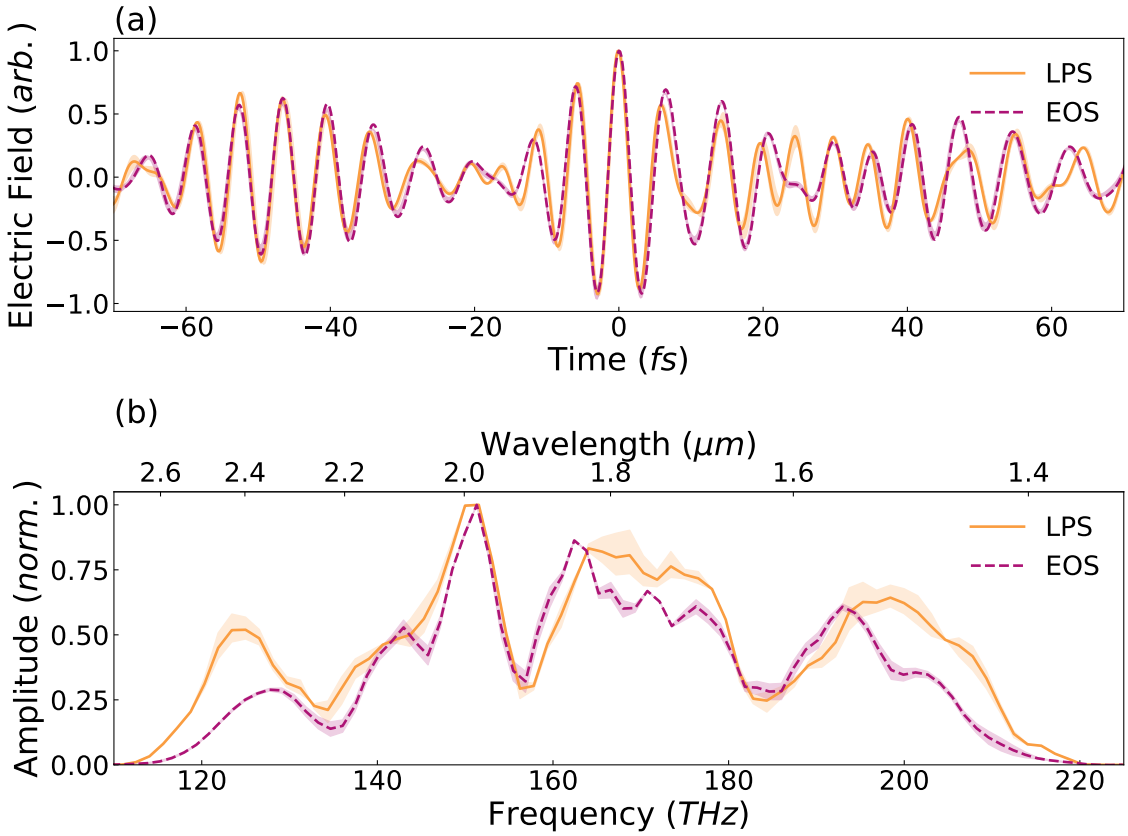

Figure 3.6: (a) The recorded waveforms of the MIR field detected via LPS (orange) and EOS (magenta dashed). (b) Corresponding spectra of the waveforms in (a). The standard deviation is represented by the shaded area around the curves.

3.3.2 LPS spectral response in GaP

To calculate the response function of LPS, the interaction of a VIS-UV few-cycle injection pulse and a MIR drive pulse is modelled in GaP using the method described in Section 3.1, following [91]. The three-dimensional time-dependent Schrödinger equation is again solved in the stationary basis of the Kohn-Sham orbitals. The

[4]See Section A.1.

electronic band structure of GaP is described by band energies and transition matrix elements, obtained from density functional theory as in Section 3.1. Then, two time-delayed laser fields are implemented:

1. A VIS-UV, 2.7 fs field, centred around 650 THz with a maximum field strength of 0.05 $\mathrm{V\AA^{-1}}$ for injecting carriers in GaP.

2. A weak MIR, 6 fs field of field strength equivalent to 0.01 $\mathrm{V\AA^{-1}}$, centred at 165 THz.

Note that the parameters chosen for the analysis of the response function of LPS are optimised for the analysed spectral range. From the interaction of the two pulses, the drift current in GaP is calculated as a function of different delays between the VIS-UV and MIR pulses.

Recall from equation (1.18) and Section 1.3.2 that the drift current is given by the integrated convolution between the gate function and the MIR vector potential. Following Fourier's transform theorem, the spectral response of LPS is then expressed as:

$$J_{LPS}(\omega) = A_{MIR}(\omega)G_{LPS}(\omega) \tag{3.2}$$

Accordingly, information about the system's response is contained and can be retrieved by dividing the Fourier transform of the drift current signal by the original MIR field. Note that $G_{LPS}(\omega)$ is proportional to the intensity of the VIS-UV pulse and the material response itself. Fig. 3.7a depicts the response function for LPS. In order to confirm that the gate function is proportional to the intensity of the pulse, the relationship between the VIS-UV pulse compression and LPS response is investigated. Second-order dispersion—commonly referred to as group delay dispersion (GDD)—is artificially applied to the VIS-UV pulse to simulate different pulse durations and phases. It is evident that the response function of LPS rolls off smoothly across most of the frequency range examined regardless of the gate field phase, as confirmed by the symmetry in the response function between positive and negative chirp values. This verifies LPS's dependency on the VIS-UV intensity envelope rather than the carrier field as postulated in Section 1.3.2. The symmetry can be explained by understanding that the original phase information of the gate field is lost after the photons are absorbed and the temporal profile of the response is a result of the generated carrier density only. Therefore, stretching the injection pulse only serves to reduce the cut-off frequency, as mentioned in Section 1.3.2.

3.3.3 EOS spectral response in BBO

To determine the response function of EOS, the VIS-UV pulse centred around 750 THz with a bandwidth of 300 THz is numerically propagated in conjunction with a broadband MIR field centred at 210 THz with a bandwidth of 180 THz, under varying time delays, as dictated by the following equation [95]:

$$\left(\partial_z - i\vec{k}(\omega)\right)\vec{E}(\vec{r},\omega) = \frac{i}{2\vec{k}(\omega)}\nabla_\perp^2\vec{E}(\vec{r},\omega) + \frac{i\omega}{2\epsilon_0 n(\omega)c}\vec{P}_{NL}(\vec{r},\omega), \tag{3.3}$$

Here $\vec{E}$ is the electric field of light, $\vec{P}_{NL}$ is the nonlinear polarisation, $\vec{k}(\omega)$ is the wavevector and $n(\omega)$ is the refractive index. The propagation assumes the slowly varying amplitude approximation and is performed in a Type-I BBO crystal, phase matching angle of $\theta = 24°$. The nonlinear polarisation response is calculated using the second ($\chi^{(2)}$) and third ($\chi^{(3)}$) order nonlinear tensors of the crystal. The response is then obtained by computing the ratio between the EOS signal (change in the polarisation state of the VIS-UV field) to the input MIR field. From this numerical investigation, several conclusions regarding the spectral response of EOS can be made.

Gate pulse compression

The complex frequency response of EOS for a thin crystal can be defined as [38]:

$$S_{EOS}(\Omega) = \int_\Omega^\infty d\omega R(\omega)|E_{LO}(\omega)||E_{SFG}(\omega-\Omega)|\exp\Big(i[\phi(\omega)-\phi(\omega-\Omega)]\Big), \tag{3.4}$$

Where ω and Ω represent the spectral components contained in the VIS-UV and MIR fields, respectively and $R(\omega)$ represents the response of the entire detection system (bandpass filter, Wollaston prism... etc). The relative phase of two spectral components, the one serving as the input to the sum frequency $\phi(\omega-\Omega)$, and the one serving as the local oscillator $\phi(\omega)$, can affect the measured signal as mentioned in Section 1.3.1. A shift in the carrier-envelope phase of the LO does not influence the EOS response, since it is a constant phase shift that cancels out. However, higher-order terms of the spectral phase, such as chirp, can reshape the response function. To demonstrate this, second-order dispersion is artificially applied to the VIS-UV pulse gate pulse to simulate different pulse durations and phases. Fig. 3.7b illustrates the calculated response functions for EOS. It is clear that the relationship between the EOS response and the VIS-UV field shape highlights the importance of a compressed gate field for EOS, particularly in the case of $\pm 5\,\mathrm{fs}^2$ where the EOS response is reduced by 38 dB.

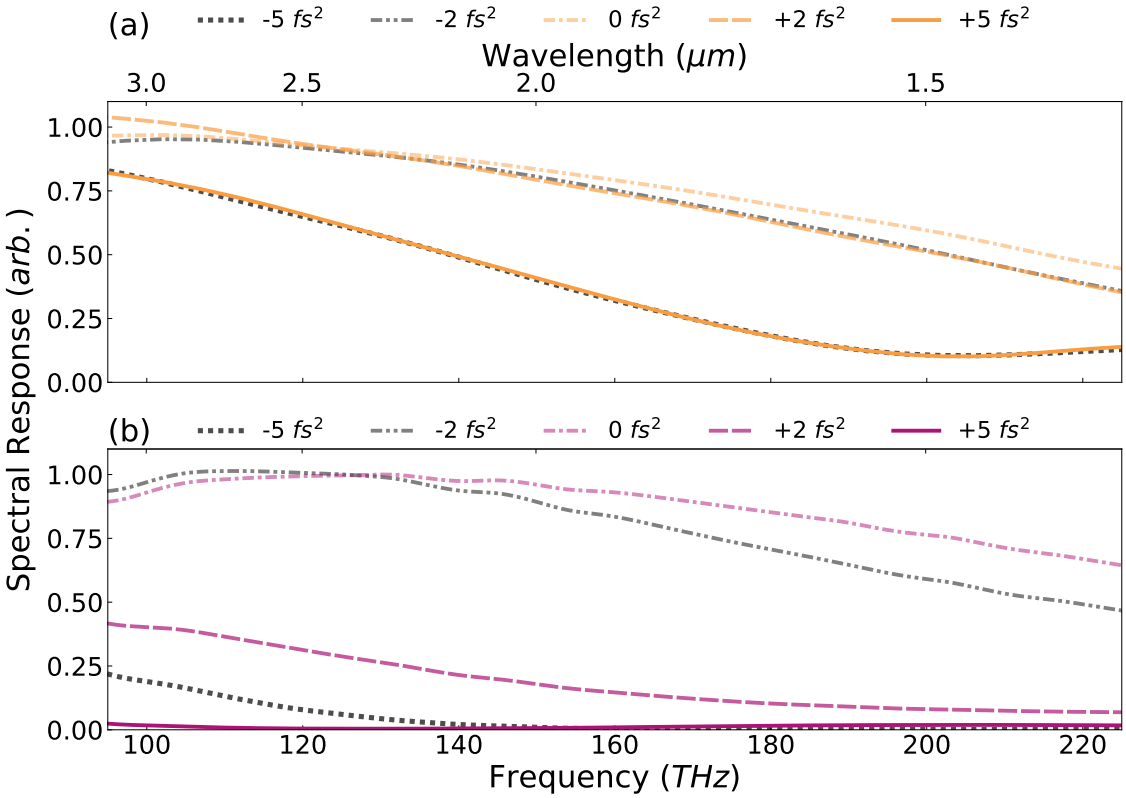

Figure 3.7: (a) LPS and (b) EOS spectral response functions calculated using different GDD values applied to the VIS-UV pulse.

Crystal thickness

Next, the effect of crystal thickness is investigated. To understand the effect of changing the EOS crystal thickness, the origin of the signal in EOS is first discussed. EOS signal generation can be broken down into two parts as shown in Fig. 3.8:

Part 1: Sum frequency generation:

1. In a Type-I geometry, the gate field (VIS-UV) and test field (MIR), are both polarised along the ordinary axis (n_o) of the EOS crystal.

2. The two fields enter and propagate collinearly in the z-direction of the EOS crystal.

3. In the first portion of the crystal, the two pulses overlap and sum frequency generation (SFG) occurs. The SFG signal relies on the presence of a reasonably

short gate pulse. By increasing the crystal thickness, the SFG signal does not necessarily increase due to the dispersion experienced by the gate pulse as discussed in the previous section. A VIS-UV pulse centred around 450 nm will experience a large group velocity dispersion[5] in BBO. For this reason, there exists a maximum nonlinear phase matching distance (optical thickness) d_{max} that depends on the dispersion experienced by the pulses.

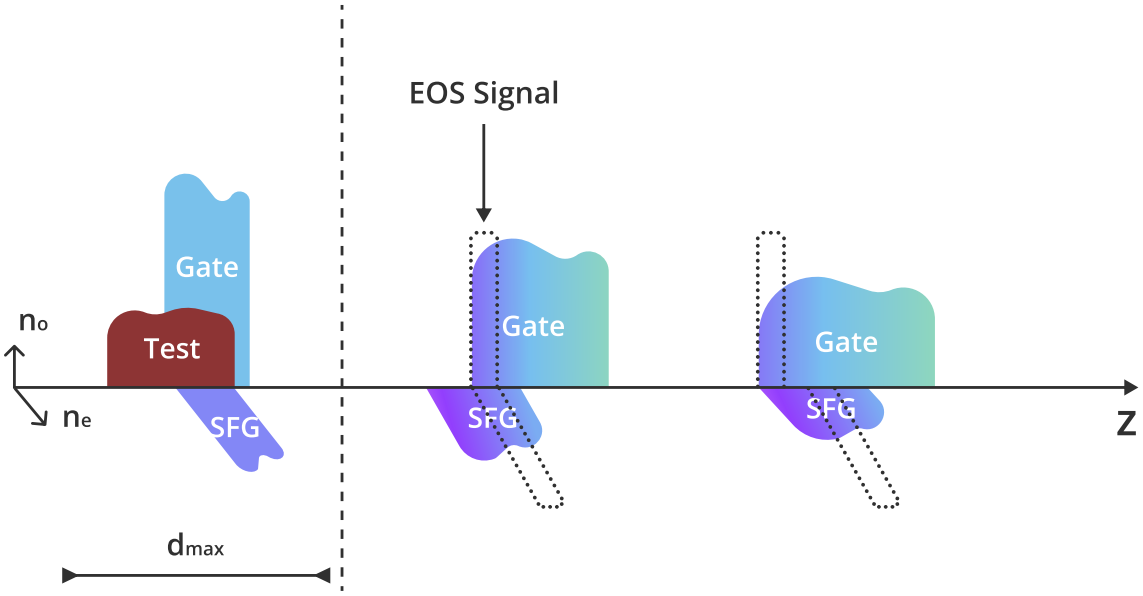

Figure 3.8: Illustration of the signal generation mechanism inside the EOS crystal. d_{max} represents the optimal nonlinear phase-matching thickness for SFG. The dotted square represents the bandpass filtered signal region. After some distance inside the crystal the filtered components no longer overlap due to temporal walk-off and there will be no EOS signal.

Part 2: Spectral interference:

1. The EOS signal originates from the spectral interference between the SFG and the local oscillator as discussed in Section 1.3.1.

2. For a Type-I phase-matching geometry, the SFG is generated on the extraordinary axis (n_e) while the LO remains on the ordinary axis (n_o).

[5] 171.66 fs^2/mm at 450 nm for n_o.

3. Each of the spectral components contained in the SFG and LO experience different refractive indices and therefore propagate with different group velocities[6].

4. The difference in group velocity results in temporal walk-off between the two portions of the spectrum as a function of crystal thickness. This results in a reduction in the overall EOS signal with increasing crystal thickness.

Fig. 3.9 compares EOS spectra calculated for different crystal thicknesses, where the gating pulse (VIS-UV) is considered optimally compressed. By increasing the crystal thickness, the spectrum of the EOS signal becomes narrower and less sensitive to the blue parts of the spectrum due to incomplete interference. Note that the temporal walk-off depends on the second-order derivative of the refractive index as a function of frequency. Knowing that the refractive index is not a linear function and increases with increasing frequency, the blue portion of the spectrum is subject to increased walk-off. Due to the temporal walk-off, the signal strength is diminished, as reflected in the reduced signal amplitude. For these reasons, a thinner crystal is typically preferable for broadband detection, provided the signal is not too weak[7].

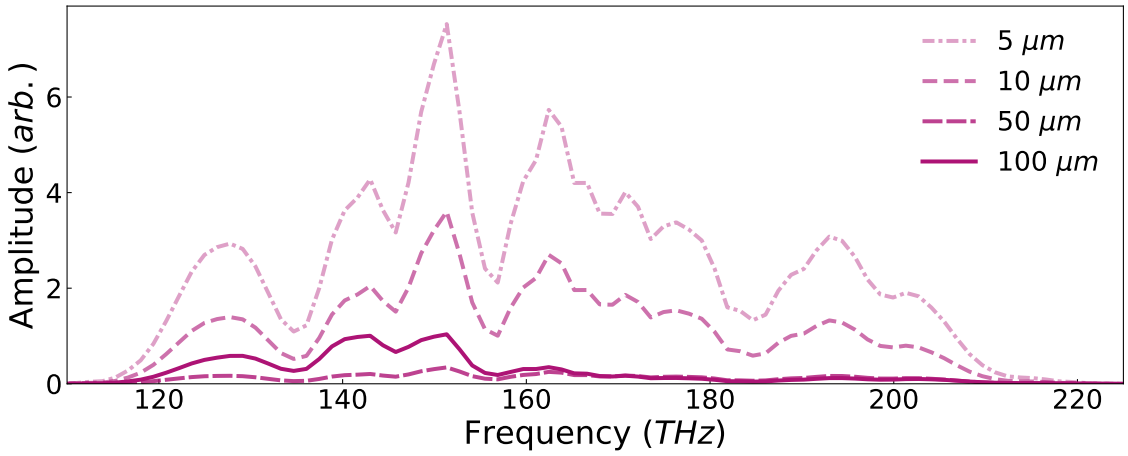

Figure 3.9: EOS spectra calibrated using response functions obtained from crystals with different thicknesses. The spectra are calculated by applying different response functions to the measured EOS signal. The original EOS spectrum is obtained using the response of a 5 μm crystal. The spectra are not normalised.

[6]For BBO, $v_{g,o} < v_{g,e}$, i.e. the LO propagates slower than the SFG.
[7]See Section 2.4.2 and Fig. 2.14 for EOS measurements performed using a thicker crystal.

Bandpass filter considerations

Fig. 3.10 demonstrates the effect of using different parameters for the bandpass filter in EOS and their influence on the response function. As can be seen in Fig. 3.10a, by fixing the width of the bandpass filter and changing the central frequency towards higher frequencies, the cut-off of the response function shifts towards higher frequencies. This feature is beneficial for detecting higher-frequency components, as mentioned in Section 1.3.1, and is a result of enhancing the signal-to-noise ratio around the low-count higher-frequency photons [37].

By keeping the central frequency fixed and changing the filter's width, the response function's shape can be modified further, as shown in Fig. 3.10b. Note that for narrower bandwidths, the signal detection is enhanced precisely for the same reason mentioned above: better signal-to-noise ratio and therefore contrast. This observation is valid so long as the signal detection is enhanced, for an infinitesimally narrow bandwidth, the signal detection compared to the baseline noise level will diminish. This comparison is performed for a flat supergaussian filter of order 4. Considering that the shapes of the spectral filters often used in experiments are different and possibly more complex than this theoretical filter, parts of the experimentally measured spectra, and therefore information, will be either badly represented or altogether lost since there will be fewer photons overall to detect.

3.4 Concluding remarks

In this chapter, an alternative method for field sampling is presented. This method is based on a single-photon absorption process and, therefore, does not require high power or high pulse energy to sample the electric field of light. It offers a cleaner detection mechanism, in comparison to NPS, by injecting a single electron with a well-defined wavepacket in a single, well-defined band [31]. Furthermore, this method can sample a large bandwidth without phase-matching limitations in contrast to EOS, which depends on nonlinear frequency mixing. The technique supports the possibility of simultaneously measuring the electric field in two spatial dimensions, opening the door for sampling fields with complex polarisations. This method overcomes some technical and physical limitations of:

- Attosecond streaking: the requirement of controlled, strong-field laser sources and vacuum infrastructure [8].
- EOS: phase-matching restrictions, the inability to measure higher-frequency components due to approaching absorption edges of common crystals, and the

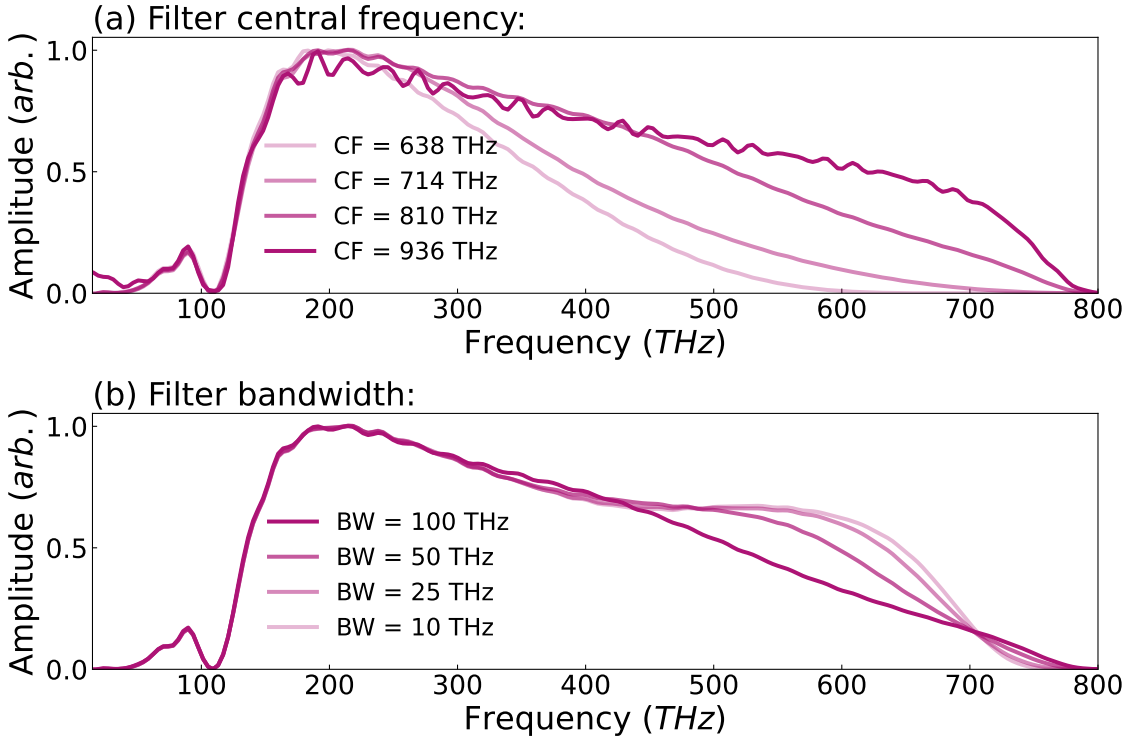

Figure 3.10: (a) EOS response function calculated for a bandpass filter of width 100 THz to evaluate the response function under different central frequencies (CF). (b) EOS response function calculated for a bandpass filter of central frequency 810 THz under different bandwidths (BW).

requirement of two consecutive measurements using two crystals to measure orthogonal polarisations [46].

- NPS: population of higher bands [31], the requirement of strong-field laser sources and the complexity of measuring fields in two dimensions.

It is worth noting that NPS as a technique has the advantage of permitting a pulse to sample itself as a result of exploiting nonlinearity. This is certainly not achievable via LPS following the Nyquist-Shannon sampling theorem, which states that the injection pulse must be shorter than a half-cycle of the driving pulse. Nevertheless, similar to NPS, the method introduced in this chapter occupies a small footprint and, therefore, can be incorporated easily into preexisting infrastructure, opening the door for sensitive field detection in low energy systems.

Since experiments using complex polarisations are underway, future experiments surveying other suitable semiconductors, such as gallium nitride, are required to

optimise the performance of this technique. Furthermore, implementing this technique to measure the NIR channel of the synthesiser would assist in determining the high-frequency cutoff, which is estimated to be around 500 THz based on the bandwidth of the VIS-UV gating pulse.

Chapter 4

Machine learning aided signal denoising

In a laboratory setting, measurements often suffer from the unfavourable effects of noise, which result in a deterioration of the measurement quality. Generally speaking, noise is a signal modification that occurs during the signal's acquisition (measurement), transport (in cables), conversion (from current to voltage), or storage (hard drives). This noise can be random and may take various forms depending on how it affects the measured signal. The most prevalent form of additive noise encountered in a laboratory setting is white noise, also known as Gaussian noise, followed by pink noise, which typically originates from electronics and scales with $1/f$. In the context of optics, intensity noise is a major disadvantage, arising from power and pointing fluctuations.

In practice, there are several methods for denoising acquired signals based on statistical and spectral techniques such as: Fourier filtering, averaging filters, and discrete wavelet transforms, in addition to advanced techniques based on machine learning (ML), such as deep neural networks [96]. The fundamental goal of all signal-denoising methods remains the same: to remove the noise while preserving the signal's underlying information and features. The choice of denoising method primarily depends on the type of noise in the signal, the type of signal, and the desired output. Fourier filtering was implemented in Chapter 2 and Chapter 3 to denoise the data obtained via NPS, LPS and EOS. This chapter develops and implements a machine learning model for denoising waveforms, such as the ones obtained in the laboratory by either of the waveform sampling techniques used in this thesis. The model is compared to traditional denoising methods, and its robustness is tested on new, unseen data. The model is written using the programming language Python and uses the following libraries: `NumPy` [97], `pandas` [98], `TensorFlow` [99], `Keras` [100], `scikit-learn` [101], and `SciPy` [102].

In the first Section (4.1), an introduction to artificial intelligence is presented. In Section (4.2) dataset utilised in the learning process is addressed, followed by Section (4.3), detailing the model infrastructure and learning. Section (4.4) presents the results, where the model is compared with conventional denoising techniques. Finally, the concluding remarks (4.5) discuss the outlook.

4.1 Introduction: artificial intelligence and machine learning

Artificial intelligence (AI) refers to intelligence demonstrated by a machine as opposed to intelligence exhibited by humans or animals. This perceived intelligence is achieved by implementing advanced algorithms, statistical models, and computational techniques that enable machines to process and analyse large amounts of data and make decisions based on the information obtained from the analysis. This allows machines to perform tasks which typically require human-level cognition, like solving puzzles, playing chess, understanding human speech or finding correlations between things. The field of AI has its roots in the work of computing pioneers such as Alan Turing, John McCarthy—who coined the term AI—and Marvin Minsky, all of whom laid out the theoretical foundations for AI in the 1950s, and 1960s [96, 103, 104].

Machine learning pertains to the capability of machines to enhance their ability to perform a specific task through gained experience. This subfield of AI is comprised of three distinct methodologies: supervised learning, unsupervised learning, and reinforcement learning, each of which operates in different ways. Supervised learning, the approach used in this thesis, is a technique that facilitates the training of a machine by providing it with explicit guidance or rules. This involves presenting the machine with input data and the corresponding expected output data, thereby allowing the machine to learn how to map the input into the output through optimising a predefined function. On the other hand, unsupervised learning involves training a machine without explicit instructions or labels. Here the machine discovers patterns in the provided data on its own that may not be immediately apparent. While reinforcement learning is a method of teaching machines to perform tasks that maximise a cumulative reward through their interaction with the environment in which the specific task is performed. For example, a robot sorts objects into boxes based on their colour, the robot is rewarded when the sorting is correct and punished when the sorting is incorrect [96, 105, 106]. Two types of problems can be addressed by supervised learning: classification and regression. Classification is the problem of identifying which of a set of categories an observation belongs to,

e.g. asking the question "Is the object red?" can be answered by either of the two categories "Yes" or "No". The ML problem addressed in this thesis is considered a regression problem since the expected output is not a discrete-valued quantity but rather a continuous range of quantities.

4.2 Dataset

As mentioned in Section 4.1, data constitute the fundamental source of information from which a ML algorithm acquires knowledge and makes predictions (regression) or decisions (classification). The dataset's quality and size, therefore, plays a significant role in the accuracy and performance of the model. A large and varied dataset provides the model with various examples, which can help it develop a more robust approach that can generalise well to new unseen data. The dataset size allows the model to avoid over-fitting, where a model only becomes an expert on the training set and struggles with new data. Moreover, a large dataset mitigates the impact of data outliers, which can skew the results of the ML algorithm. For these reasons, a large and diverse artificial dataset, based on waveforms typically measured in a laboratory setting is generated to augment [107] the size of the dataset required for training the model.

4.2.1 Artificial generation of data

Waveforms following the equation:

$$E(t) = \text{Amplitude} \times \text{Gaussian Envelope} \times \text{Carrier Wave} \times \text{Phase}, \tag{4.1}$$

are generated, where the individual quantities are defined as:

$$\text{Amplitude} = 10^{-2} \times \mathbf{R} \tag{4.2}$$

$$\text{Gaussian Envelope} = \exp\left(- \left[\frac{t - t_{\mathbf{R}}}{\sigma_{\mathbf{R}}} \right]^2 \right) \tag{4.3}$$

$$\text{Carrier Wave} = \exp\left(i\omega_{\mathbf{R}} t \right) \tag{4.4}$$

$$\begin{aligned} \text{Phase} = \exp\Big(i[&10^{-4}\mathbf{R}t^4 + 10^{-3}\mathbf{R}t^3 + 10^{-2}\mathbf{R}t^2 \\ &+ 10^{-1}\mathbf{R}t + \text{CEP}_{\mathbf{R}}] \Big) \end{aligned} \tag{4.5}$$

Note that $\mathbf{R} \rightarrow [0, 1]$ and is randomly selected. The subscript $_{\mathbf{R}}$ denotes a randomly generated value from a range of values. For $t_{\mathbf{R}} \rightarrow [-65, 65]$ (fs), $\sigma_{\mathbf{R}} \rightarrow [5, 35]$

(fs), $\omega_{\mathbf{R}} \rightarrow [375, 750]$ (THz) and $\mathrm{CEP}_{\mathbf{R}} \rightarrow [0, 2\pi)$. This methodology randomly generates a set of waveforms with different arrival times $t_{\mathbf{R}}$, widths $\sigma_{\mathbf{R}}$, central frequencies $\omega_{\mathbf{R}}$, and phases. Fig. 4.1 (magenta dashed) depicts a sample of the randomly generated waveforms. The waveforms are then transformed from the time domain to the frequency domain. Random additive Gaussian noise is applied to the generated waveforms before transforming the data back to the time domain to form the noisy waveforms (light magenta). The total sample size generated by the method is $m = 64000$ waveforms. The dataset is randomly split into a training set containing $m_{\mathrm{train}} = 57600$ waveforms and a test set containing $m_{\mathrm{test}} = 6400$ waveforms. The model is trained using the training set and tested using the testing set. The testing set is hidden from the model and only used to evaluate the model's performance after the model is finished with the learning process.

4.2.2 Data preprocessing for machine learning purposes

In machine learning, a *feature* represents a quantifiable attribute or characteristic of a given phenomenon and is conceptually related to explanatory variables used in statistics. In the context of measured waveforms, points where the field exists in the measurement are regarded as features. Note that ML algorithms deal with numerical values assigned to features, and a significant disparity in the range of values can result in an implicit assumption of "feature importance" assigned to features with higher values. For instance, if a measured waveform is extremely noisy, the large value of noise will appear to the ML model as an essential feature, whereas in reality, the underlying pattern that the model should recognise is the actual waveform and not the noise. To combat this issue, *feature scaling* is performed as a preprocessing step. It refers to the normalisation of the range of values associated with the features within a dataset. The objective is, therefore, to counteract the potential statistical skewing in the ML model caused by the significant discrepancies in the values assigned to the features within a given dataset. This step enhances the performance and accuracy of the ML algorithm, in addition to allowing the model to converge much faster.

The data used for training the ML model in this chapter are scaled using `sklearn.preprocessing.MaxAbsScaler()`. This estimator scales each feature individually such that the maximum absolute value of each element in the training set is equal to 1 following the expression $X_{\mathrm{scaled}} = X/\max(|X|)$. Once the model is finished with the learning process, the data is reverted to its original unscaled state.

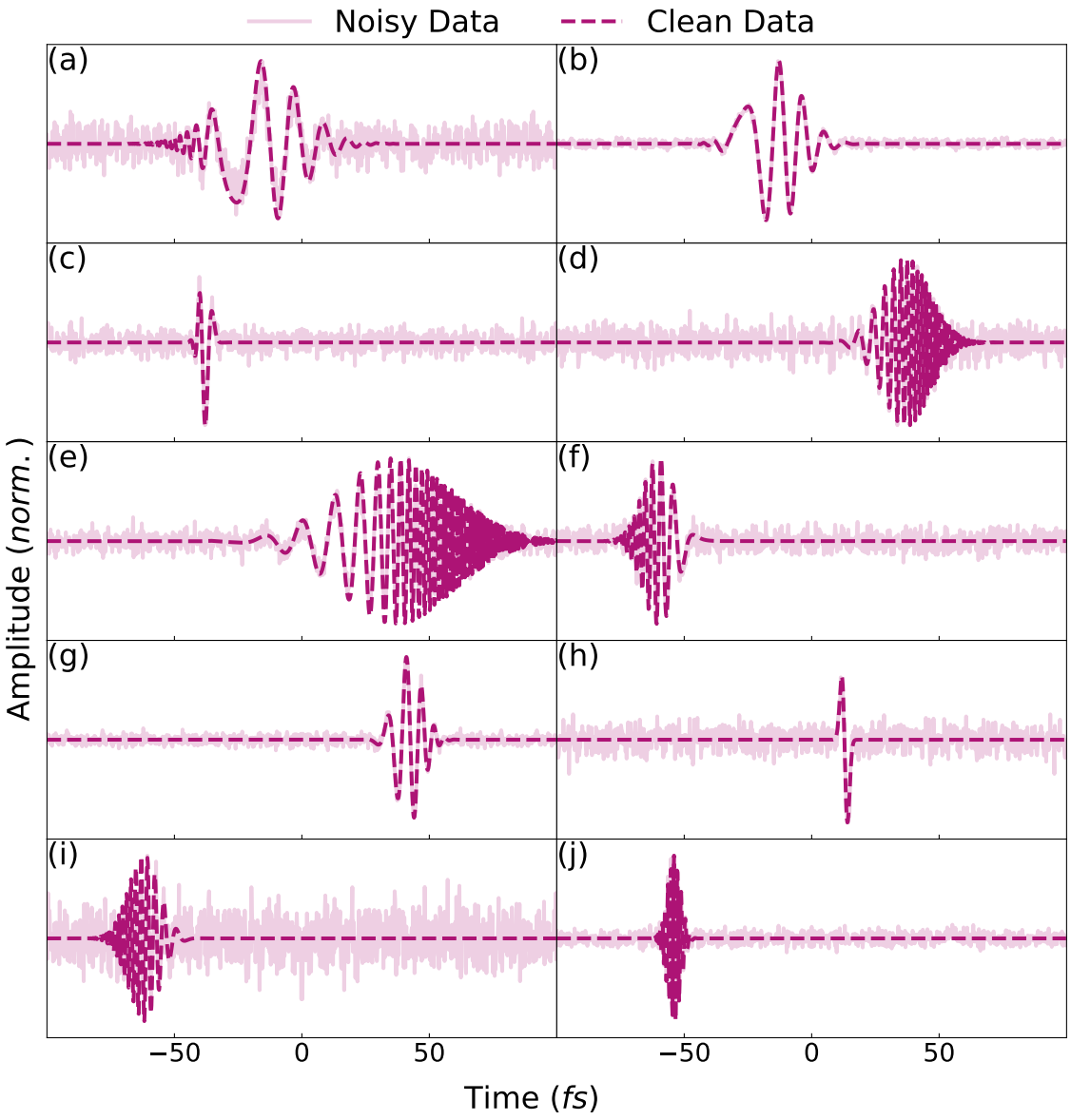

Figure 4.1: Randomly selected waveforms from the training dataset. The methodology in Section 4.2 randomly generates a set of waveforms with different arrival times $t_{\mathbf{R}}$, widths $\sigma_{\mathbf{R}}$, central frequencies $\omega_{\mathbf{R}}$, and phases, where $t_{\mathbf{R}} \to [-65, 65]$ (fs), $\sigma_{\mathbf{R}} \to [5, 35]$ (fs), $\omega_{\mathbf{R}} \to [375, 750]$ (THz) and $\text{CEP}_{\mathbf{R}} \to [0, 2\pi)$. Note that the plotted waveforms are normalised.

4.3 Machine learning model

The most basic ML model is based on the *Perceptron*, which is considered the first artificial neural network [108–110]. A Perceptron mimics a neuron and consists of an *input*, a *node* and an *output*. A more complex artificial neural network mimicking a brain can be constructed by combining several Perceptrons. Fig. 4.2 illustrates a simple neural network consisting of a first input layer with n units (orange), a second layer with two nodes (grey), a third layer with a single node (grey) and a fourth output layer (magenta) for a total of four layers. The two layers in grey form two "hidden layers". An *activation function* Φ is employed in each internal layer to switch the nodes ON or OFF, similar to integrated circuits, thereby determining that layer's output. By doing so, activation functions introduce nonlinearity to the model, permitting it to learn a more complex representation of the data. Following the diagram in Fig. 4.2, the mathematical operations performed on the input data are given by:

Input	$\vec{x} = x_1 + x_2 + ... + x_n$	vector
Layer 1	$a_1^2 = \Phi(w_{11}^1 x_1 + w_{12}^1 x_2 + w_{13}^1 x_3 + w_{1n}^1 x_n)$ $a_2^2 = \Phi(w_{21}^1 x_1 + w_{22}^1 x_2 + w_{23}^1 x_3 + w_{2n}^1 x_n)$	vector
Layer 2	$a_1^3 = \Phi(w_{11}^2 a_1 + w_{12}^2 a_2)$	vector
Output	$h = a_1^3$	vector

The function Φ can take many forms, with the rectified linear, sigmoid and hyperbolic tangent being the most common [104]. The steps performed in the previous table are commonly referred to as *forward propagation*. A single forward propagation through the architecture is insufficient for the model to learn. A recursive algorithm based on a *cost function* (error function) that the model tries to minimise and *back propagation* is therefore implemented. In the context of supervised learning, for a set of input training data $\vec{X}_{\text{train}} = \{\vec{x}_1, \vec{x}_2 \ ... \ \vec{x}_m\}$, where m is the number of examples, the algorithm performs a forward propagation step and defines a hypothesis $H = \{h_1, h_2 \ ... \ h_m\}$. The model then computes the error in the prediction by comparing the hypothesis H with the expected output data $\vec{Y}_{\text{train}} = \{\vec{y}_1, \vec{y}_2 \ ... \ \vec{y}_m\}$. Based on the calculated error, the model back propagates and modifies the weights w_n^i and repeats the process until the cost function is minimised.

The model developed in this section is a one-dimensional *convolutional neural network* written using the library `Keras`. Convolutional neural networks are a class of artificial neural networks with a hierarchical structure of *convolution* and *pooling* layers that can extract relevant features from the input data. They are particularly effective in processing data that can be presented on a grid, such as time-series data

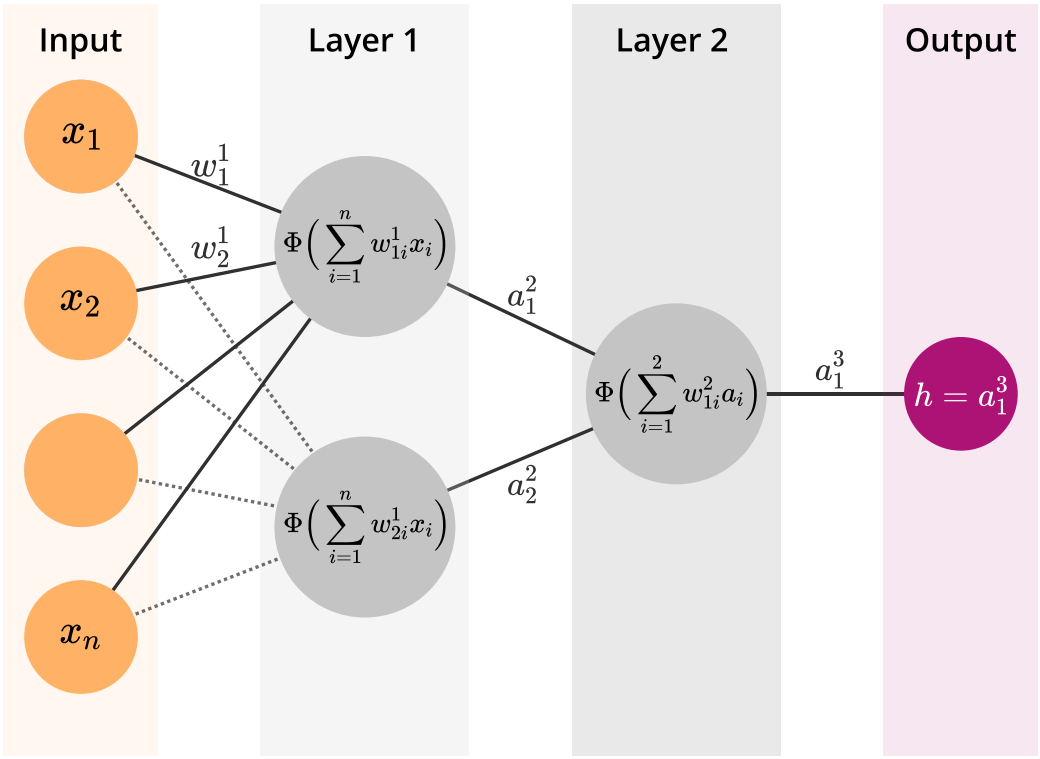

Figure 4.2: A simple neural network. The input layer contains the preprocessed and normalised data (orange circles). The first and second layers (grey circles) are called hidden layers since their values do not appear in the training set. The first layer applies the weights w_n^i, where i denotes the layer number and n denotes the input unit, onto the unit values x_n. In each node (grey circle), an activation function Φ is applied to the vector sum of the weights multiplied by the unit values to generate the quantities a_1^2 and a_2^2. The second layer applies another activation function, Φ, this time on the input from the first layer (namely a_1^2 and a_2^2), to generate the output a_1^3. This neural network defines a hypothesis (or prediction) h, which, in this case, is equal to a_1^3.

(e.g. a waveform), which can be represented as a one-dimensional vector of regularly spaced samples or image data, defined as two- or three-dimensional matrices or tensors of pixels. Like in artificial neural networks, each convolution layer has specific weighted filters (w, called kernels) applied to the input data to help the model identify patterns. Pooling layers then downsample the number of detected features, which reduces the number of parameters in the model (reduces computational cost) and prevents over-fitting by generating a more abstract representation of the data [96]. The type of pooling chosen for this model is *Max Pooling*, which also acts as a noise suppressant by discarding the noisy activations, thereby achieving de-noising in parallel with downsampling. The Table 4.1 below summarises the hyperparameters (parameters that control the learning process) of the model:

Number of layers	10, including input and output layers
Activation function	hyperbolic tangent
Optimisation algorithm	Adam [111]
Cost function	Mean squared error
Metric	Root mean square error
Batch size	128
Epochs	1000

Table 4.1: The optimisation algorithm Adam is a variant of stochastic gradient descent, which is a superior alternative to traditional gradient descent since it is computationally more efficient and converges much faster to the minimum of the error function. The cost function is used as the objective for the optimisation process in training the model. A metric is a function used to assess the performance of the model. A batch is a subset of training data used in one iteration of training in the model. An epoch refers to one complete iteration over the entire training dataset. The model parameters are then updated based on the error calculated.

To arrive at these hyperparameters, hyperparameter optimisation is performed. This is done using the function `sklearn.model_selection.GridSearchCV()` which performs an exhaustive search over specified hyperparameter values (optimisers, batch size, number of epochs, cost function, metrics... etc). Once hyperparameter optimisation is completed and the most optimal hyperparameters are chosen, the model commences the learning process using the function `tf.keras.Model.fit()`:

1. The model takes the training set $\vec{X}_{\text{train},\, m}$ for $m_{\text{train}} = 57600$ and randomly splits off 20% of the data for validation, $\vec{X}_{\text{val}}$. This fraction of the data is set apart from the training data and the model will not train on it. Note that the validation set is especially useful for hyperparameter tuning. When

performing a grid search, the hyperparameter selection is based on the model performance using the validation set.

2. The model divides the remaining 80% of the training data into batches (of size 128 for a total of 360 batches) and runs each batch through the model architecture.

3. After each batch, the model back propagates and updates the weights. The calculated errors are averaged over the batch size, before tackling the next batch.

4. Once all the batch (360) runs are completed, the model finishes one epoch. Note that 80% of $m_{\text{train}} = 46080$, this means the model will run 360 batches per epoch.

5. At the end of each epoch, the model uses both the training and the validation sets to compare its prediction (or hypothesis) $\vec{Y}_{\text{pred}}$ with $\vec{Y}_{\text{train/val}}$ and evaluate the losses and metrics.

6. The next epoch starts and the model repeats the process until all epochs (1000) are complete.

Fig. 4.3 plots the learning curves of the model. A good fit model typically has a sharp training loss and validation loss at the beginning, they both then gradually decrease and flatten. The flattening indicates that adding more training examples does not improve the model performance on training data.

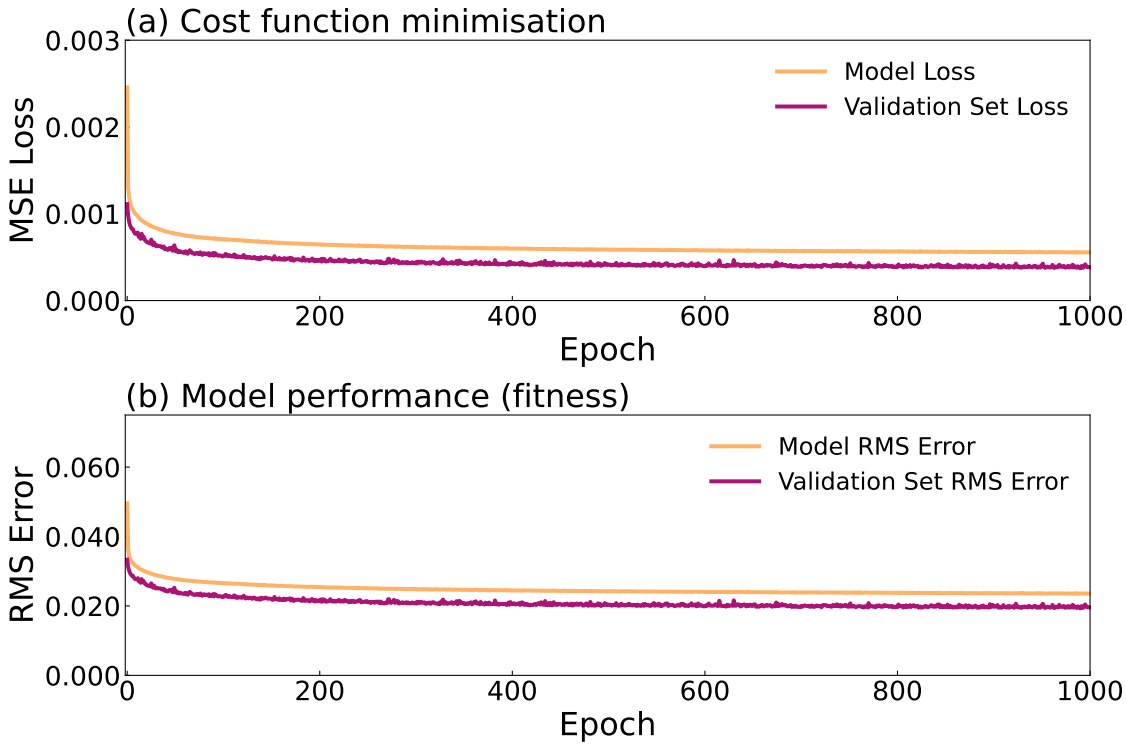

Figure 4.3: (a) Comparison between the model loss (orange) and the validation set loss (magenta). This illustration represents the minimisation efforts of the model per epoch. (b) Model performance as obtained through the root mean square error metric per epoch.

4.4 Results

To test the model's performance on unseen data, recall that a test set containing $m_{\text{test}} = 6400$ waveforms was split off and reserved earlier. This test dataset is now presented to the model using the function `tf.keras.Model.predict()`. Significant overlap between the model prediction $\vec{Y}_{\text{pred}}$ and the target or correct waveforms $\vec{Y}_{\text{test}}$ is clear in Fig. 4.4. Furthermore, the Pearson correlation coefficient is calculated for each plot with excellent correlation.

To further demonstrate that the model does not *just* learn the shape of a waveform and therefore predict a waveform regardless of the input data, Fig. 4.4d demonstrates that the model is also capable of predicting linear data entirely dissimilar to a "waveform". Statistically, the Pearson correlation coefficient measures relative changes since it is a normalised measurement of the covariance, which makes

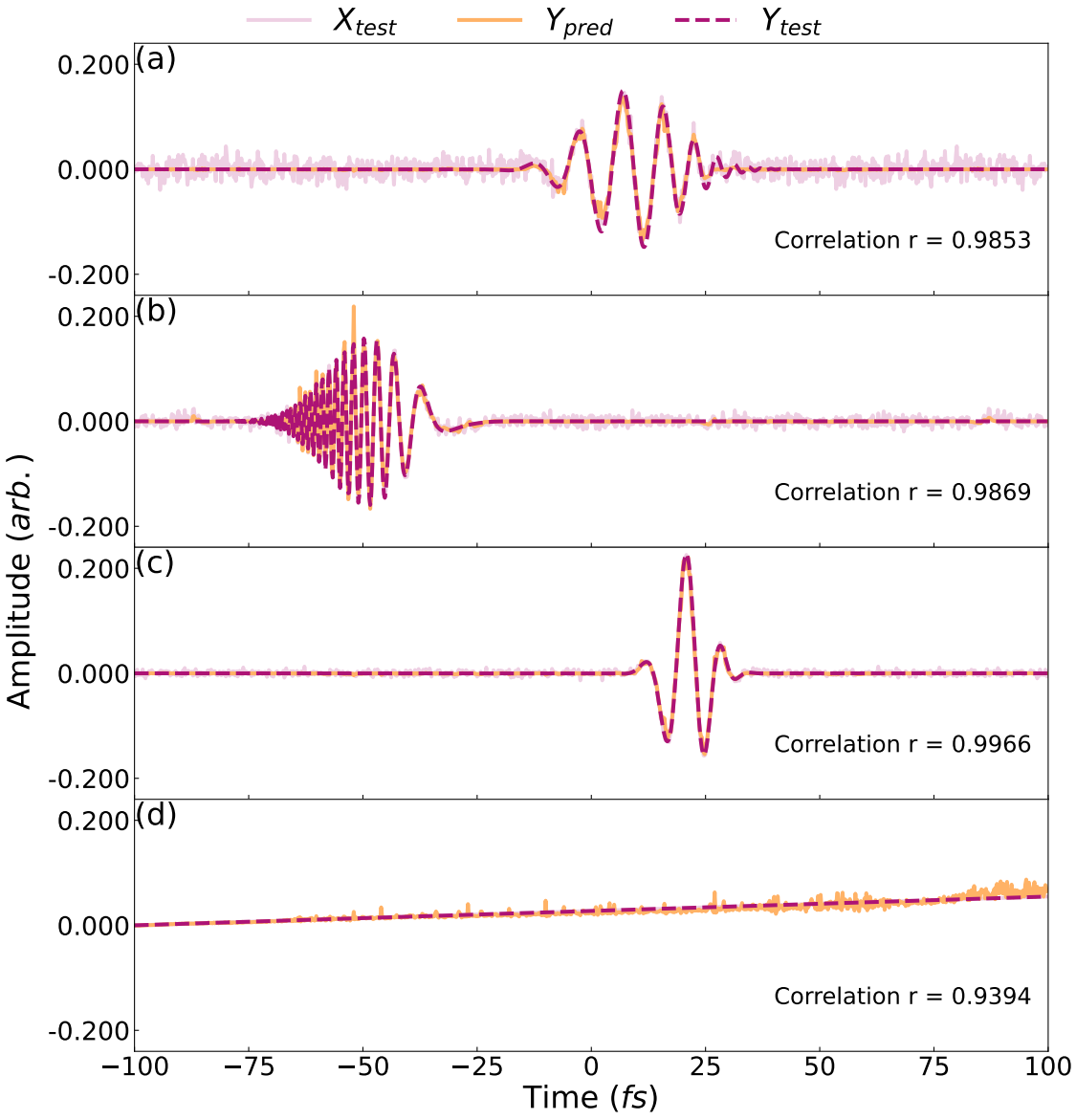

Figure 4.4: A sample of the waveforms as predicted by the model $\vec{Y}_{\text{pred}}$ is shown in orange. The noisy waveforms $\vec{X}_{\text{test}}$ fed into the model are shown in light magenta. The dashed magenta line represents the target waveforms $\vec{Y}_{\text{test}}$.

it independent of the magnitude of the numbers[1]. To quantify how well the predicted values $\vec{Y}_{\text{pred}}$ *exactly* match the target values $\vec{Y}_{\text{test}}$, the coefficient of determination[2] is calculated for the model with an overall score of $R^2 = 0.962$ using `sklearn.metrics.r2_score()`. The result is plotted in Fig. 4.5. It is clear from the plot that most of the predicted waveforms match exceptionally well with the target waveforms, with 6165 test samples having a score of over 0.9. Note that the overall score is weighted by the statistical variance of each prediction so that the statistical significance of extreme outliers is considered proportionally.

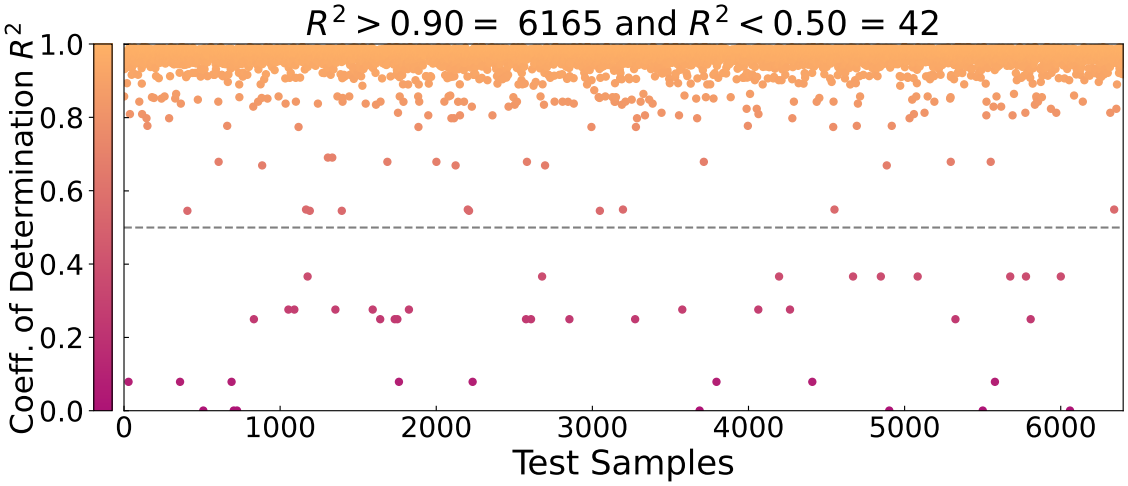

Figure 4.5: Coefficient of determination for all 6400 test samples.

For further confirmation, the model is presented with a sinc function, and its prediction is evaluated in the time domain and the frequency domain. Fig. 4.6 illustrates the results. Note the model does not train on data in the frequency domain. The predicted spectra are obtained by computing the 1D discrete Fourier transform, utilising the function `NumPy.fft.fft()`. The illustration clearly shows that the model can predict the square spectrum, characteristic of a sinc function, despite the relatively small signal-to-noise ratio.

[1] See Section A.1.
[2] See Section A.2.

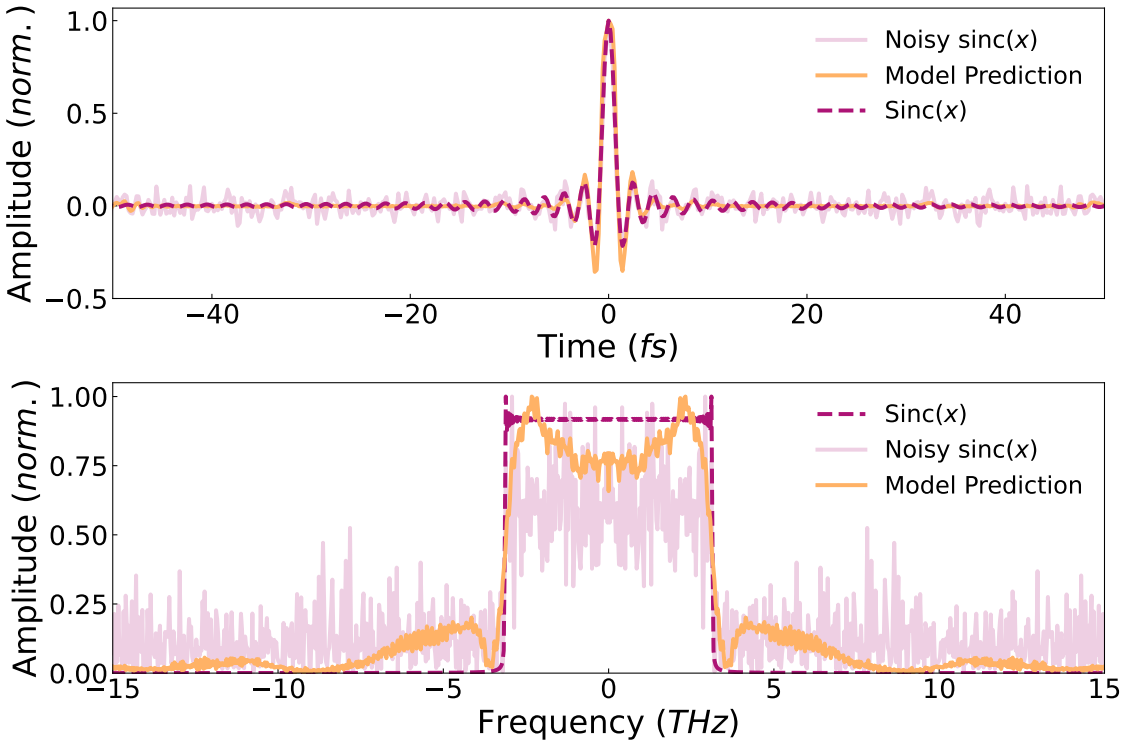

Figure 4.6: Prediction of an unseen sinc function in the time domain (top) and frequency domain (bottom).

4.4.1 Comparison to standard signal processing techniques

Signal processing methods can be categorised into three domains: time domain, frequency domain and time-frequency domain analysis methods. Time domain analysis involves assessing properties such as amplitude and phase which can be extracted by methods such as temporal filtering (windowing), auto- or cross-correlation, and convolution. These approaches facilitate the estimation of the signal's duration or the identification of patterns in the signal. On the other hand, frequency analysis methods rely on Fourier analysis, which converts a time signal into its frequency domain representation. This representation arises from the decomposition of functions into a series of contributions from different sines and cosines at different frequencies. By performing a Fourier transform, the frequency content and its magnitude can be obtained. From there thresholding, filtering (low-pass, high-pass and bandpass), and padding can be performed in the frequency domain, before transforming the signal back into the time domain which aids in signal denoising. To confirm that the machine learning model does not modify the frequency content of the signal in the area of interest representing the waveform, the extracted frequency content

from the model is compared to the standard Fourier analysis approach using the Fourier transform and Fourier bandpass filtering. The results are shown in Fig. 4.7. From the plot, it appears that the denoised signal overlaps quite well, and the peak frequency (represented by the vertical lines) extracted is identical.

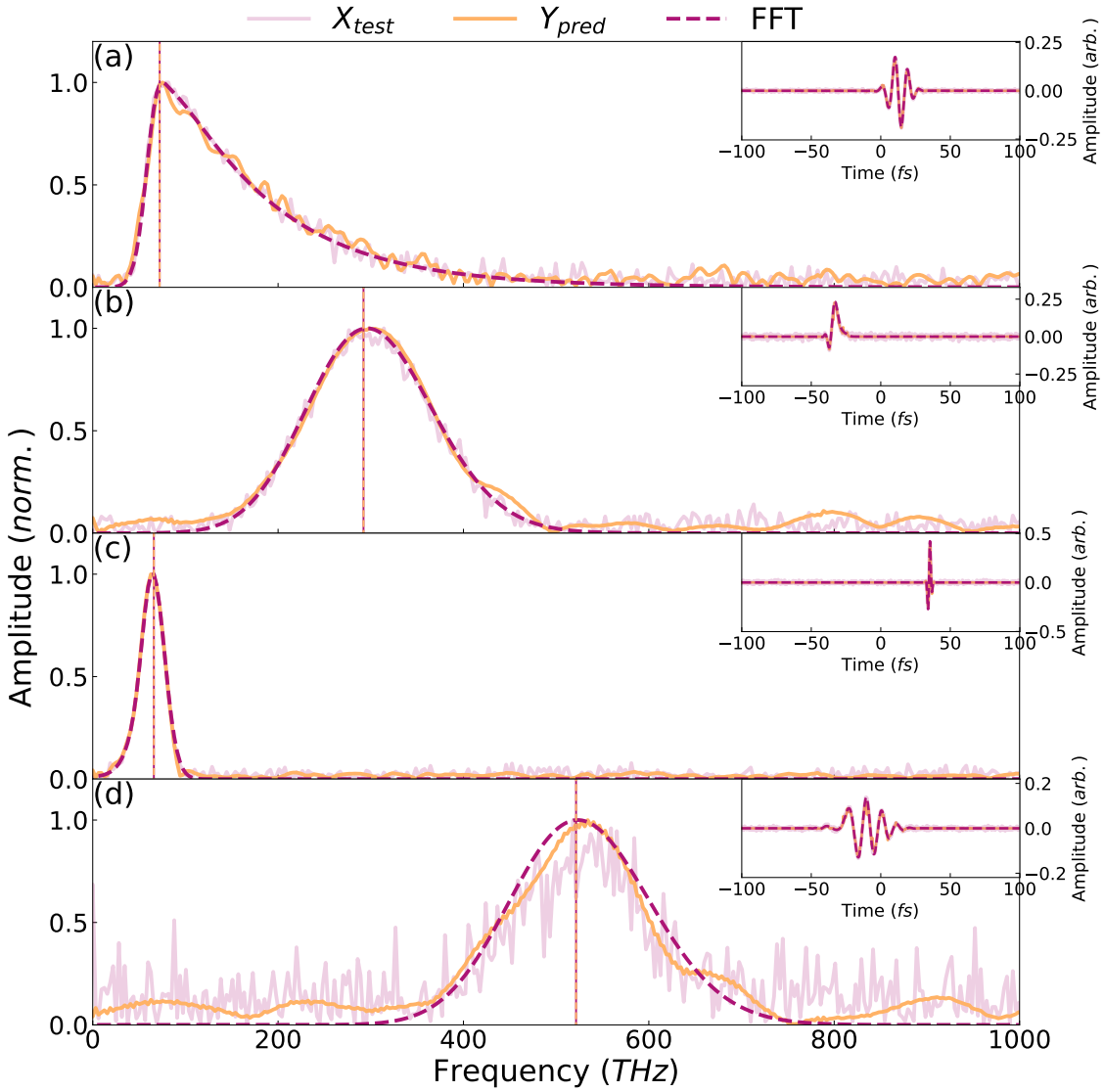

Figure 4.7: Frequency domain comparison between the ML model output (orange) and the standard Fourier transform (FFT) procedure (magenta dashed) for various pulses shown in the insets. The peak frequency is denoted by the vertical lines.

A limitation of standard Fourier analysis originates in the time-frequency du-

ality, which is constrained by Heisenberg's uncertainity principle $\Delta t \Delta \nu \geq 1$ [112]. For instances where it is necessary to obtain information on which frequencies exist at which points in time, time-frequency analysis is typically used. Some examples of time-frequency techniques include the windowed Fourier transform (short-time Fourier transform) and the wavelet transform. For completeness, the performance of the ML model is tested against the wavelet transform using the Python library `PyWavelets` [113].

The wavelet transform[3] is a linear signal processing technique that decomposes a given signal into a set of wavelet coefficients called approximation and detail coefficients [114]. The transform convolves the signal iteratively following a multiresolution analysis algorithm, with a set of high-pass (detail) and low-pass (approximation) filters at varying delays, effectively filtering low- and high-frequency components, respectively, to obtain the coefficients. The set of filters is defined by a scalable *mother wavelet* $\Psi_{(s,l)}(x) = 2^{-s/2}\Psi(2^{-s}x - l)$, which is scaled (in frequency) by the parameter s and translated (in time) by the parameter l. The algorithm is then designed to give good time but poor frequency resolution at high frequencies of Ψ and good frequency but poor time resolution at low frequencies of Ψ. The most prominent dissimilarity between the wavelet transform and the Fourier transform is the set basis functions used to construct the transform. Fourier is based on sines and cosines, whereas the wavelet transform has an infinite set of basis functions. Any scalable, orthogonal functions with a finite energy qualify as basis functions.

Wavelets can be used to denoise data through iterative thresholding [115]. The approximation filters act as averaging filters whereas the detail filters extract high frequency information. Soft thresholding [116] (values $< 2\sigma$ are set to zero) is implemented to omit high frequency information, which are typically characteristic of noise. The data is then transformed back at the end of the iterative process, producing the denoised data [114, 115]. Fig. 4.8 presents a comparison between the performance of the ML model vs. the discrete wavelet transform. The denoising is performed using two layers of filters and the `Symlets 8` family of wavelets. It is evident from Fig. 4.8a and 4.8b that both techniques perform really well when the signal to noise ratio is small. In situations where the signal to noise ratio is large, like Fig. 4.8c and 4.8d, the ML model outperforms the wavelet transform. Note that due to the iterative filtering process in the wavelet transform method, the amplitude of the signal decreases, since some of the energy is removed by the filtering stages (thresholding).

[3] See Section A.3.

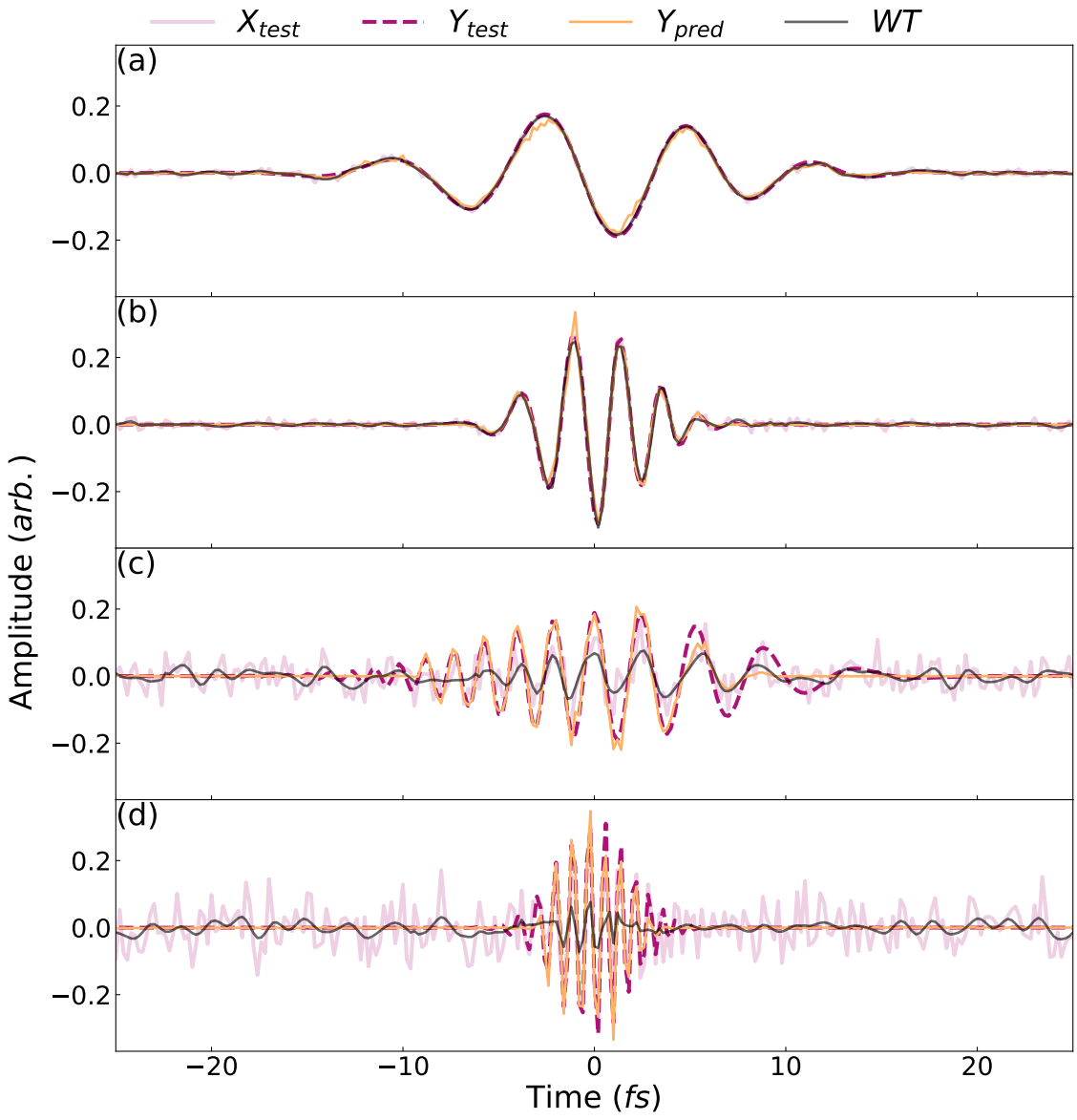

Figure 4.8: Comparison between the model's denoising performance (orange) and a two level Wavelet Transform (WT, grey). The magenta dashed line represents the target data.

4.5 Concluding remarks

In this chapter, a machine learning model based on a convolutional neural network is presented as a means for denoising data acquired in the laboratory. As discussed in the previous section, the model exhibits exceptional performance in comparison to traditional techniques like Fourier filtering and wavelet transforms. While the performance of the ML model in denoising data is exceptional, the output *may* contain nonphysical results. This is reflected in the amplitude of the denoised waveforms, which appears to not decrease despite the removal of noise. This may lead to a nonphysical estimation of power or energy from the spectral density. The current ML model's utility lies in experiments that rely on relative rather than absolute measurements, such as spectral measurements, where information is extracted from ratios.

As mentioned earlier in Section 4.2, the efficacy of the ML model is subject to the quality and composition of the dataset it is trained on. This is because a model's capacity to learn is confined to the information presented to it during training, and therefore the characteristics of the dataset determine the limitations of the model. This observation was realised in the earlier stages of the model development. Initially, the augmented dataset contained waveforms that were translated and centred around 0 fs. This human error led the model to believe that "something" must appear around 0 fs, even if the test data was pure noise. For this reason, the dataset was revised, and randomness was incorporated in every parameter possible as mentioned in Section 4.2.1. By doing so, the model performance was greatly improved, and it could generalise well to data that does not resemble a waveform as shown in Fig. 4.4d. From this, it is clear that a more comprehensive examination of the model and dataset needs to be performed and cross-examined with laboratory measurements in the future to obtain precise estimations of power and energy.

Summary and outlook

Direct access to the temporal evolution of few-cycle pulses opened up a new path to study the electronic response of various media [12–21]. Recent advancements in the development, control and characterisation of such few-cycle pulses initiated a new era of spectroscopic [117, 118] and microscopic [55, 119] techniques and triggered the development of a plethora of pulse characterisation tools as detailed in [23, 24, 31, 38, 39, 55].

In this thesis, pulse characterisation techniques based on photoconductive sampling[1], both linear and nonlinear, have been developed and implemented to measure the electric field of a test pulse. In Chapter 2, a chirped pulse amplification system based on titanium-sapphire technology is implemented to generate phase-stable few-cycle 1.86 W at 3 kHz pulses with a bandwidth of 400-1100 nm. A portion of the power is split off to form the gating field, whereas the remainder of the power is utilised to generate a 2.1 μm test pulse. Nonlinear photoconductive sampling is then implemented in a specially designed heterostructured sample, engineered to increase the signal obtained from the measurement technique. The sample concept is inspired by high-mobility electron transistors, with one small-bandgap layer comprised of amorphous silicon donating its carriers to a large-bandgap layer comprised of fused silica. As demonstrated in Section 2.4.1, the heterostructured sample significantly increases the magnitude of the measured signal, making it beneficial for systems operating with low pulse energies, such as oscillators. Furthermore, as shown in Section 2.4.2, and as a consequence of having more signal, the heterostructured sample arrives at the stable detection regime earlier than non-engineered samples (e.g. fused silica and gallium phosphide), which makes it a powerful candidate for passive phase-detection in analogy to [24]. A summary of the experimental work done in Chapter 2 can be seen in Fig. 5.1 in the top panel.

In Chapter 3, two amplifiers, one based on the technology of regenerative amplification and the other on titanium sapphire chirped pulse amplification technology, are synchronised and implemented to create a phase-stable waveform synthesiser.

[1] See Section 1.3.2.

The output of the broadening stage preceding the synthesiser spans three octaves, from 300-3000 nm. A portion of the spectrum covering 300-600 nm is split off to form a VIS-UV gating field, whereas the test MIR pulse is formed by the portion of the spectrum spanning 1500-3000 nm. The field of the test pulse is then sampled by employing the technique of linear photoconductive sampling in a gallium phosphide sample. Gallium phosphide is chosen for its bandgap, which equals the central frequency of the VIS-UV pulse. As shown in Section 3.3.1, the technique extends the limit of linear photoconductive sampling in ambient air from 100 to more than 200 THz. Moreover, since the technique is based on linear absorption of a single photon, it does not require strong, waveform-controlled fields for sampling the field of the test MIR pulse. A summary of the experimental work done in Chapter 3 can be seen in the bottom panel of Fig. 5.1.

Both results from Chapter 2 and Chapter 3 are benchmarked against electro-optic sampling, another established field sampling technique[2]. In the case of Chapter 2, the results offer the following advantages:

1. The heterostructured sample can detect currents when the gate field has pulse energies as low as 42 nJ, in the range of energies provided by commercial oscillators.

2. The sample offers 31× more signal than fused silica.

3. Considering that more current is generated, the sample saturates and arrives at the desired stable detection regime earlier than fused silica, and other samples [24, 25].

4. Photoconductive sampling can sample a large bandwidth and does not require phase-matching, in contrast to electro-optic sampling.

In the case of Chapter 3, the results offer the following advantages:

1. Since the gating process is linear, constraints on using waveform-controlled strong fields are lifted, and this technique does not require high pulse energies, in contrast to nonlinear photoconductive sampling.

2. In comparison to electro-optic sampling, constraints on the pulse phase are lifted since the only factor that plays a role in the high-frequency cutoff is the pulse duration.

[2] See Section 1.3.1.

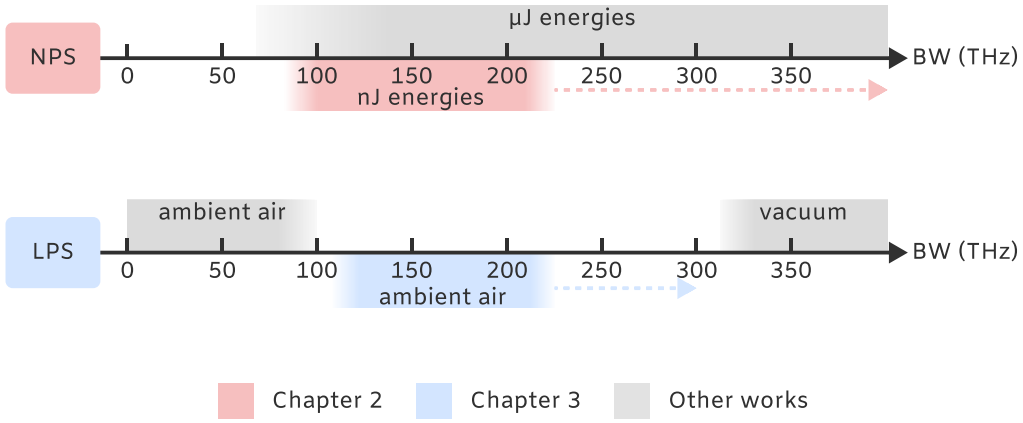

Figure 5.1: Contribution of this thesis to photoconductive field-resolved metrology techniques. Top panel: Chapter 2 (red) contributes to the technique of NPS by employing a custom-built heterostructured sample to boost the overall signal obtained via injection, as demonstrated in Section 2.4.1. This is reflected in the fact that the heterostructured sample establishes the capability of detecting carriers injected with energies as low as 42 nJ, in the range of pulse energies provided by oscillators, as opposed to [27] which relied on pulse energies approximately a thousand times higher at 7μJ, as indicated by the coloured arrows. This fact allows for the utilisation of the device as a phase detector, with possible applications as a phasemeter in low pulse energy systems [24]. Furthermore, the heterostructured sample reaches the stable detection regime earlier than the samples used by others (grey) [24, 25, 27] as shown in Section 2.4.2, enabling reliable field detection in low pulse energy systems. Note that the heterostructured sample does not, in principle, limit the bandwidth of detection. The dashed arrow (red dashed) denotes a yet unexplored range of frequencies. Bottom panel: Chapter 3 (blue) contributes to the technique of LPS by extending the detection bandwidth from 100 THz [30] (grey, left) to more than 200 THz by employing a VIS-UV pulse for injection [88]. Moreover, the technique operates in ambient air conditions, which avoids the need for attosecond pulses from high harmonic generation and vacuum infrastructure altogether, in contrast to [31] (grey, right). The dashed arrow (blue dashed) indicates a range of frequencies that can be examined by implementing the LPS technique in a larger bandgap material. In principle, the NIR channel of the syntehsiser can be used as a drive pulse to cover the range from 220-315 THz.

3. The experimental methodology permits the simultaneous measurement of fields with complex polarisation structures, opening the door for field-resolved spectroscopic measurements in two dimensions.

4. Photoconductive sampling can sample a large bandwidth and does not require phase-matching, unlike electro-optic sampling.

5. The entire process takes place in ambient air conditions, in contrast to [31].

Lastly, Chapter 4 draws from the contemporary tool and emergent technology of machine learning to denoise data resembling waveforms obtained by measurement techniques such as the ones presented in Chapter 2 and Chapter 3. The convolutional neural network is developed and implemented on a large augmented dataset containing 64000 noisy waveforms. The algorithm is compared to conventional denoising techniques such as Fourier filtering and the wavelet transform with excellent results. However, a caveat of the present approach is that it may yield nonphysical results, and the current model's utility lies in experiments that rely on relative rather than absolute measurements.

The prospects of expanding on the results presented in this thesis are numerous. To touch on a few upcoming possibilities: the sample implemented in Chapter 2 is optimised and designed specifically for a laser system with the aforementioned specific parameters. A similar approach to what is done in Chapter 2 can be applied to laser systems operating with different central frequencies, for example, 2 μm systems. Moreover, a thorough examination of the device and its applicability as a passive phase detector is needed, in addition to testing the device with a low pulse energy system such as an oscillator. Additionally, in a fashion similar to [27], it is necessary to examine the operation of the heterostructured sample in the unexplored range of frequencies from 220-1000 THz shown in Fig. 5.1. For Chapter 3, testing the technique using a slightly larger bandgap material such as gallium nitride is called for to push the method towards bridging the gap between 220-310 THz, as indicated in Fig. 5.1. Furthermore, testing the technique in a two-dimensional measurement setup is yet to be shown. The results from Chapter 4 can be expanded to yield absolute results rather than relative results by carefully calibrating the model and cross-examining its results with laboratory measurements.

Appendix A

Mathematical formulae

A.1 Pearson correlation coefficient

The Pearson correlation coefficient is given by the covariance of two variables divided by the product of their standard deviations, defined as:

$$\text{corr(X,Y)} = \frac{\text{cov}(X,Y)}{\sigma_X \sigma_Y}. \tag{A.1}$$

It is a measure of the linear correlation between two sets of data. Through its definition, it is evident that the Pearson correlation coefficient is a normalised measurement of the covariance, such that the results always have a value between -1 and 1. Correlations equal to +1 or -1 correspond to data points lying exactly on a line, and a value of exactly +1 or -1 implies that a linear equation describes the relationship between X and Y. The sign of the number is determined by the slope of the line, +1 for increasing X and Y, -1 for decreasing X and Y, and a value of 0 implies that there is no linear dependency between X and Y [120]. The Pearson coefficient can be colloquially understood as "how close are the two variables X and Y to the line of best fit?".

A.2 Coefficient of determination

In a regression model, for a dataset comprised of a vector $\vec{Y} = \{\vec{y}_1, \vec{y}_2 \ ... \ \vec{y}_m\}$ and an associated predictions vector $\vec{Y}_{\text{pred}} = \{\vec{y}_{\text{pred},1}, \vec{y}_{\text{pred},2} \ ... \ \vec{y}_{\text{pred},m}\}$, the coefficient of determination calculates the proportion of the variation in the dependent variable $\vec{Y}_{\text{pred}}$ relative to the total variance of the independent variable $\vec{Y}$. It is defined as:

$$R^2 = 1 - \frac{\sum_i^m (Y_i - Y_{\text{pred},i})^2}{\sum_i^m (Y_i - \overline{Y})^2}, \tag{A.2}$$

where the bar notation denotes the mean of $\vec{Y}$. The numerator is often referred to as "residuals" or "errors".

It typically has a value between 0 and 1, where 0 indicates that the model does not explain any of the variability in the dependent variable, and 1 indicates that the model explains all of the variability. Note that if the model predicts the mean $\overline{Y}$, based on the definition above, $R^2 = 0$. If the model predicts values worse than the mean, this means the numerator will be greater than the denominator, such that $R^2 < 0$. This means that the R^2 fit is worse than the null hypothesis, or a straight line, and the chosen model does not follow the trend of the data, yielding a random fit. Note that R^2 is not actually a squared value and can therefore be negative. For $R^2 = 0.6$, 60% of the variability of $\vec{Y}_{\text{pred}}$ is accounted for, and the remaining 40% of the variability is unaccounted for [120]. The coefficient of determination can be colloquially understood as "how well can the independent variable predict the dependent variable?" or in other words "how good is this model?".

A.3 Wavelet transform

For a function $f(x)$, the wavelet transform W can be expressed as:

$$W[f(l,s)] = 2^{-s/2} \int_{-\infty}^{\infty} f(x)\Psi(2^{-s}x - l)dx, \tag{A.3}$$

where l is a translation parameter and s is a scaling parameter. The basis function Ψ, referred to as a *mother wavelet*, defines a Hilbert basis of square integrable, orthonormal functions. The functions are formed by translations l and dilations s such that $\Psi \in L^2(\mathbb{R})$. Generally speaking, scalable, orthogonal (inner product = 0) functions with a finite energy qualify as basis functions.

A.4 Data processing of the waveforms

The MIR waveforms are processed by applying a supergaussian bandpass filter in the frequency domain following:

$$SG(\nu) = \exp\left(-\frac{\nu - \nu_0}{2\sigma} \right)^{10}, \tag{A.4}$$

where in Chapter 2, $\nu_0 = 145\,\mathrm{THz}$ and $\sigma = 50\,\mathrm{THz}$ and in Chapter 3, $\nu_0 = 165\,\mathrm{THz}$ and $\sigma = 45\,\mathrm{THz}$.

Bibliography

[1] T. H. Maiman. Stimulated optical radiation in ruby. *Nature*, 187(4736):493–494, Aug 1960.

[2] F. J. McClung and R. W. Hellwarth. Giant optical pulsations from ruby. *Journal of Applied Physics*, 33(3):828–829, 1962.

[3] E.P. Ippen, C.V. Shank, and A. Dienes. Passive mode locking of the cw dye laser. *Applied Physics Letters*, 21(8):348–350, 1972.

[4] Hans W. Mocker and R. J. Collins. Mode competition and self-locking effects in a q-switched ruby laser. *Applied Physics Letters*, 7(10):270–273, 1965.

[5] R. L. Fork, B. I. Greene, and C. V. Shank. Generation of optical pulses shorter than 0.1 psec by colliding pulse mode locking. *Applied Physics Letters*, 38(9):671–672, 1981.

[6] Marcos Dantus, Mark J. Rosker, and Ahmed H. Zewail. Real-time femtosecond probing of "transition states" in chemical reactions. *The Journal of Chemical Physics*, 87(4):2395–2397, 1987.

[7] M. Hentschel, R. Kienberger, Ch. Spielmann, G. A. Reider, N. Milosevic, T. Brabec, P. Corkum, U. Heinzmann, M. Drescher, and F. Krausz. Attosecond metrology. *Nature*, 414(6863):509–513, Nov 2001.

[8] Ferenc Krausz and Misha Ivanov. Attosecond physics. *Rev. Mod. Phys.*, 81:163–234, Feb 2009.

[9] R. Kienberger, E. Goulielmakis, M. Uiberacker, A. Baltuska, V. Yakovlev, F. Bammer, A. Scrinzi, Th. Westerwalbesloh, U. Kleineberg, U. Heinzmann, M. Drescher, and F. Krausz. Atomic transient recorder. *Nature*, 427(6977):817–821, Feb 2004.

[10] Shambhu Ghimire and David A. Reis. High-harmonic generation from solids. *Nature Physics*, 15(1):10–16, Jan 2019.

[11] Tran Trung Luu, Zhong Yin, Arohi Jain, Thomas Gaumnitz, Yoann Pertot, Jun Ma, and Hans Jakob Wörner. Extreme–ultraviolet high–harmonic generation in liquids. *Nature Communications*, 9(1):3723, Sep 2018.

[12] E. Goulielmakis, M. Uiberacker, R. Kienberger, A. Baltuska, V. Yakovlev, A. Scrinzi, Th. Westerwalbesloh, U. Kleineberg, U. Heinzmann, M. Drescher, and F. Krausz. Direct measurement of light waves. *Science*, 305(5688):1267–1269, 2004.

[13] M Drescher, M Hentschel, R Kienberger, M Uiberacker, Th Westerwalbesloh, U Kleineberg, U Heinzmann, and F Krausz. Time-resolved electron spectroscopy of atomic inner-shell dynamics. *Journal of Electron Spectroscopy and Related Phenomena*, 137-140:259–264, 2004. ICESS-9 Proceedings of the 9th International Conference on Electronic Spectroscopy and Structure.

[14] M. F. Kling, Ch. Siedschlag, A. J. Verhoef, J. I. Khan, M. Schultze, Th. Uphues, Y. Ni, M. Uiberacker, M. Drescher, F. Krausz, and M. J. J. Vrakking. Control of electron localization in molecular dissociation. *Science*, 312(5771):246–248, 2006.

[15] Martin Huppert, Inga Jordan, Denitsa Baykusheva, Aaron von Conta, and Hans Jakob Wörner. Attosecond delays in molecular photoionization. *Phys. Rev. Lett.*, 117:093001, Aug 2016.

[16] J. Vos, L. Cattaneo, S. Patchkovskii, T. Zimmermann, C. Cirelli, M. Lucchini, A. Kheifets, A. S. Landsman, and U. Keller. Orientation-dependent stereo wigner time delay and electron localization in a small molecule. *Science*, 360(6395):1326–1330, 2018.

[17] Shubhadeep Biswas, Benjamin Förg, Lisa Ortmann, Johannes Schötz, Wolfgang Schweinberger, Tomáš Zimmermann, Liangwen Pi, Denitsa Baykusheva, Hafiz A. Masood, Ioannis Liontos, Amgad M. Kamal, Nora G. Kling, Abdullah F. Alharbi, Meshaal Alharbi, Abdallah M. Azzeer, Gregor Hartmann, Hans J. Wörner, Alexandra S. Landsman, and Matthias F. Kling. Probing molecular environment through photoemission delays. *Nat. Phys.*, 16(7):778–783, Jul 2020.

[18] E. Goulielmakis, V. S. Yakovlev, A. L. Cavalieri, M. Uiberacker, V. Pervak, A. Apolonski, R. Kienberger, U. Kleineberg, and F. Krausz. Attosecond control and measurement: Lightwave electronics. *Science*, 317(5839):769–775, 2007.

[19] A. L. Cavalieri, N. Müller, Th. Uphues, V. S. Yakovlev, A. Baltuška, B. Horvath, B. Schmidt, L. Blümel, R. Holzwarth, S. Hendel, M. Drescher,

U. Kleineberg, P. M. Echenique, R. Kienberger, F. Krausz, and U. Heinzmann. Attosecond spectroscopy in condensed matter. *Nature*, 449(7165):1029–1032, Oct 2007.

[20] Martin Schultze, Elisabeth M. Bothschafter, Annkatrin Sommer, Simon Holzner, Wolfgang Schweinberger, Markus Fiess, Michael Hofstetter, Reinhard Kienberger, Vadym Apalkov, Vladislav S. Yakovlev, Mark I. Stockman, and Ferenc Krausz. Controlling dielectrics with the electric field of light. *Nature*, 493(7430):75–78, Jan 2013.

[21] Martin Schultze, Krupa Ramasesha, C.D. Pemmaraju, S.A. Sato, D. Whitmore, A. Gandman, James S. Prell, L. J. Borja, D. Prendergast, K. Yabana, Daniel M. Neumark, and Stephen R. Leone. Attosecond band-gap dynamics in silicon. *Science*, 346(6215):1348–1352, 2014.

[22] Kyung Taec Kim, Chunmei Zhang, Andrew D. Shiner, Bruno E. Schmidt, François Légaré, D. M. Villeneuve, and P. B. Corkum. Petahertz optical oscilloscope. *Nature Photonics*, 7(12):958–962, Dec 2013.

[23] Agustin Schiffrin, Tim Paasch-Colberg, Nicholas Karpowicz, Vadym Apalkov, Daniel Gerster, Sascha Mühlbrandt, Michael Korbman, Joachim Reichert, Martin Schultze, Simon Holzner, Johannes V. Barth, Reinhard Kienberger, Ralph Ernstorfer, Vladislav S. Yakovlev, Mark I. Stockman, and Ferenc Krausz. Optical-field-induced current in dielectrics. *Nature*, 493(7430):70–74, Jan 2013.

[24] Tim Paasch-Colberg, Agustin Schiffrin, Nicholas Karpowicz, Stanislav Kruchinin, Özge Sağlam, Sabine Keiber, Olga Razskazovskaya, Sascha Mühlbrandt, Ali Alnaser, Matthias Kübel, Vadym Apalkov, Daniel Gerster, Joachim Reichert, Tibor Wittmann, Johannes V. Barth, Mark I. Stockman, Ralph Ernstorfer, Vladislav S. Yakovlev, Reinhard Kienberger, and Ferenc Krausz. Solid-state light-phase detector. *Nature Photonics*, 8(3):214–218, Mar 2014.

[25] Tim Paasch-Colberg, Stanislav Yu. Kruchinin, Özge Sağlam, Stefan Kapser, Stefano Cabrini, Sascha Muehlbrandt, Joachim Reichert, Johannes V. Barth, Ralph Ernstorfer, Reinhard Kienberger, Vladislav S. Yakovlev, Nicholas Karpowicz, and Agustin Schiffrin. Sub-cycle optical control of current in a semiconductor: from the multiphoton to the tunneling regime. *Optica*, 3(12):1358–1361, Dec 2016.

[26] Takuya Higuchi, Christian Heide, Konrad Ullmann, Heiko B. Weber, and Peter Hommelhoff. Light-field-driven currents in graphene. *Nature*, 550(7675):224–228, Oct 2017.

[27] Shawn Sederberg, Dmitry Zimin, Sabine Keiber, Florian Siegrist, Michael S. Wismer, Vladislav S. Yakovlev, Isabella Floss, Christoph Lemell, Joachim Burgdörfer, Martin Schultze, Ferenc Krausz, and Nicholas Karpowicz. Attosecond optoelectronic field measurement in solids. *Nature Communications*, 11(1):430, Jan 2020.

[28] D. H. Auston. Picosecond optoelectronic switching and gating in silicon. *Appl. Phys. Lett.*, 26(3):101–103, 1975.

[29] P.R. Smith, D.H. Auston, and M.C. Nuss. Subpicosecond photoconducting dipole antennas. *IEEE Journal of Quantum Electronics*, 24(2):255–260, 1988.

[30] Masaaki Ashida. Ultra-broadband terahertz wave detection using photoconductive antenna. *Jap. J. Appl. Phys.*, 47(10):8221–8225, oct 2008.

[31] M. Ossiander, K. Golyari, K. Scharl, L. Lehnert, F. Siegrist, J. P. Bürger, D. Zimin, J. A. Gessner, M. Weidman, I. Floss, V. Smejkal, S. Donsa, C. Lemell, F. Libisch, N. Karpowicz, J. Burgdörfer, F. Krausz, and M. Schultze. The speed limit of optoelectronics. *Nat. Com.*, 13(1):1620, Mar 2022.

[32] Seung Beom Park, Kyungseung Kim, Wosik Cho, Sung In Hwang, Igor Ivanov, Chang Hee Nam, and Kyung Taec Kim. Direct sampling of a light wave in air. *Optica*, 5(4):402–408, Apr 2018.

[33] Yangyang Liu, John E. Beetar, Jonathan Nesper, Shima Gholam-Mirzaei, and Michael Chini. Single-shot measurement of few-cycle optical waveforms on a chip. *Nature Photonics*, 16(2):109–112, Feb 2022.

[34] J. A. Valdmanis, G. Mourou, and C. W. Gabel. Picosecond electro-optic sampling system. *Applied Physics Letters*, 41(3):211–212, 1982.

[35] Ahmed H. Zewail. Laser femtochemistry. *Science*, 242(4886):1645–1653, 1988.

[36] Ferenc Krausz. The birth of attosecond physics and its coming of age. *Physica Scripta*, 91(6):063011, may 2016.

[37] Michael Porer, Jean-Michel Ménard, and Rupert Huber. Shot noise reduced terahertz detection via spectrally postfiltered electro-optic sampling. *Opt. Lett.*, 39(8):2435–2438, Apr 2014.

[38] Sabine Keiber, Shawn Sederberg, Alexander Schwarz, Michael Trubetskov, Volodymyr Pervak, Ferenc Krausz, and Nicholas Karpowicz. Electro-optic sampling of near-infrared waveforms. *Nature Photonics*, 10(3):159–162, Mar 2016.

[39] Enrico Ridente, Mikhail Mamaikin, Najd Altwaijry, Dmitry Zimin, Matthias F. Kling, Vladimir Pervak, Matthew Weidman, Ferenc Krausz, and Nicholas Karpowicz. Electro-optic characterization of synthesized infrared-visible light fields. *Nature Communications*, 13(1):1111, Mar 2022.

[40] Dmitry A. Zimin, Vladislav S. Yakovlev, and Nicholas Karpowicz. Ultra-broadband all-optical sampling of optical waveforms. *Science Advances*, 8(51):eade1029, 2022.

[41] Thomas Gaumnitz, Arohi Jain, Yoann Pertot, Martin Huppert, Inga Jordan, Fernando Ardana-Lamas, and Hans Jakob Wörner. Streaking of 43-attosecond soft-x-ray pulses generated by a passively cep-stable mid-infrared driver. *Opt. Express*, 25(22):27506–27518, Oct 2017.

[42] Q. Wu and X.-C. Zhang. Free-space electro-optic sampling of terahertz beams. *Applied Physics Letters*, 67(24):3523–3525, 1995.

[43] G. Gallot and D. Grischkowsky. Electro-optic detection of terahertz radiation. *J. Opt. Soc. Am. B*, 16(8):1204–1212, Aug 1999.

[44] S. Kono, M. Tani, and K. Sakai. Coherent detection of mid-infrared radiation up to 60thz with an lt-gaas photoconductive antenna. *IEE Proc. Optoelectr.*, 149:105–109(4), June 2002.

[45] Q. Wu and X.-C. Zhang. Free-space electro-optics sampling of mid-infrared pulses. *Applied Physics Letters*, 71(10):1285–1286, 1997.

[46] LiangLiang Zhang, Hua Zhong, Chao Deng, CunLin Zhang, and YueJin Zhao. Polarization sensitive terahertz time-domain spectroscopy for birefringent materials. *Appl. Phys. Lett.*, 94(21):211106, 2009.

[47] Bahaa E. A. Saleh and Malvin Carl Teich. *Fundamentals of photonics: Part 1: Optics; 3rd edition.* Wiley series in pure and applied optics. Wiley, Hoboken, 2019.

[48] Robert W Boyd. *Nonlinear optics; 2nd ed.* Academic Press, Amsterdam, 2003.

[49] Robert R. Thomson, Derryck T. Reid, and Christopher G. Leburn. *Ultrafast Nonlinear Optics.* Scottish Graduate Series. Springer Cham, 2013.

[50] Charles Kittel. *Introduction to Solid State Physics.* Wiley, 8 edition, 2004.

[51] N. W. Ashcroft and N. D. Mermin. *Solid State Physics.* Holt-Saunders, 1976.

[52] Felix Bloch. Über die quantenmechanik der elektronen in kristallgittern. *Z. Phys.*, 52(7):555–600, Jul 1929.

[53] Mark Fox. *Optical properties of solids*. Oxford master series in condensed matter physics. Oxford University Press, Oxford U.K., second edition, 2010.

[54] John Singleton. *Band Theory and Electronic Properties of Solids*. Oxford master series in condensed matter physics. Oxford University Press, Oxford U.K., first edition, 2001.

[55] Mikhail Mamaikin, Yik-Long Li, Enrico Ridente, Wei Ting Chen, Joon-Suh Park, Alexander Y. Zhu, Federico Capasso, Matthew Weidman, Martin Schultze, Ferenc Krausz, and Nicholas Karpowicz. Electric-field-resolved near-infrared microscopy. *Optica*, 9(6):616–622, Jun 2022.

[56] Rick Trebino, Kenneth W. DeLong, David N. Fittinghoff, John N. Sweetser, Marco A. Krumbügel, Bruce A. Richman, and Daniel J. Kane. Measuring ultrashort laser pulses in the time-frequency domain using frequency-resolved optical gating. *Review of Scientific Instruments*, 68(9):3277–3295, 1997.

[57] Rick Trebino. *Frequency-Resolved Optical Gating*. Springer New York, NY, 31 August 2002.

[58] Yutaka Nomura, Hideto Shirai, and Takao Fuji. Frequency-resolved optical gating capable of carrier-envelope phase determination. *Nature Communications*, 4(1):2820, Nov 2013.

[59] A Herbst, K Scheffter, M M Bidhendi, M Kieker, A Srivastava, and H Fattahi. Recent advances in petahertz electric field sampling. *Journal of Physics B: Atomic, Molecular and Optical Physics*, 55(17):172001, aug 2022.

[60] T. M. Fortier, P. A. Roos, D. J. Jones, S. T. Cundiff, R. D. R. Bhat, and J. E. Sipe. Carrier-envelope phase-controlled quantum interference of injected photocurrents in semiconductors. *Phys. Rev. Lett.*, 92:147403, Apr 2004.

[61] Dandan Hui, Husain Alqattan, Shunsuke Yamada, Vladimir Pervak, Kazuhiro Yabana, and Mohammed Th. Hassan. Attosecond electron motion control in dielectric. *Nature Photonics*, 16(1):33–37, Jan 2022.

[62] C.E. Shannon. Communication in the presence of noise. *Proceedings of the IRE*, 37(1):10–21, 1949.

[63] Johannes Schötz, Ancyline Maliakkal, Johannes Blöchl, Dmitry Zimin, Zilong Wang, Philipp Rosenberger, Meshaal Alharbi, Abdallah M. Azzeer, Matthew

Weidman, Vladislav S. Yakovlev, Boris Bergues, and Matthias F. Kling. The emergence of macroscopic currents in photoconductive sampling of optical fields. *Nature Communications*, 13(1):962, Feb 2022.

[64] R Jung, J.C Lee, G.T Orosz, A Sulyok, G Zsolt, and M Menyhard. Determination of effective electron inelastic mean free paths in sio2 and si3n4 using a si reference. *Surface Science*, 543(1):153–161, 2003.

[65] A. Korobenko, K. Johnston, M. Kubullek, L. Arissian, Z. Dube, T. Wang, M. Kübel, A. Yu. Naumov, D. M. Villeneuve, M. F. Kling, P. B. Corkum, A. Staudte, and B. Bergues. Femtosecond streaking in ambient air. *Optica*, 7(10):1372–1376, Oct 2020.

[66] Dmitry Zimin, Matthew Weidman, Johannes Schötz, Matthias F. Kling, Vladislav S. Yakovlev, Ferenc Krausz, and Nicholas Karpowicz. Petahertz-scale nonlinear photoconductive sampling in air. *Optica*, 8(5):586–590, May 2021.

[67] Johannes Schötz, Ancyline Maliakkal, Johannes Blöchl, Dmitry Zimin, Zilong Wang, Philipp Rosenberger, Meshaal Alharbi, Abdallah M. Azzeer, Matthew Weidman, Vladislav S. Yakovlev, Boris Bergues, and Matthias F. Kling. The emergence of macroscopic currents in photoconductive sampling of optical fields. *Nature Communications*, 13(1):962, Feb 2022.

[68] R. Boylested and L. Nashelsky. *Electronic Devices and Circuit Theory*. Prentice Hall, eleventh edition, 2012.

[69] Xiaobing Mei, Wayne Yoshida, Mike Lange, Jane Lee, Joe Zhou, Po-Hsin Liu, Kevin Leong, Alex Zamora, Jose Padilla, Stephen Sarkozy, Richard Lai, and William R. Deal. First demonstration of amplification at 1 thz using 25-nm inp high electron mobility transistor process. *IEEE Electron Device Letters*, 36(4):327–329, 2015.

[70] Dandan Hui, Husain Alqattan, Simin Zhang, Vladimir Pervak, Enam Chowdhury, and Mohammed Th. Hassan. Ultrafast optical switching and data encoding on synthesized light fields. *Science Advances*, 9(8):eadf1015, 2023.

[71] MATLAB. *R2017b*. The MathWorks Inc., Natick, Massachusetts, 2017.

[72] J.C. Butcher. A history of runge-kutta methods. *Applied Numerical Mathematics*, 20(3):247–260, 1996.

[73] P. Drude. Zur elektronentheorie der metalle. *Annalen der Physik*, 306(3):566–613, 1900.

[74] P. Drude. Zur elektronentheorie der metalle; ii. teil. galvanomagnetische und thermomagnetische effecte. *Annalen der Physik*, 308(11):369–402, 1900.

[75] Sabine Keiber. *Novel Metrology Techniques Resolve Strong-Field-Driven Electron Dynamics in Solids*. PhD thesis, Ludwig-Maximilians-Universität München, Geschwister-Scholl-Platz 1, 80539 München, 2016.

[76] Najd Altwaijry. *Optimising Strong-Field-Induced Currents in Solids Using Wave Propagation Effects*. Master's thesis, Ludwig-Maximilians-Universität München, Geschwister-Scholl-Platz 1, 80539 München, 2018.

[77] Nae-Man Park, Tae-Soo Kim, and Seong-Ju Park. Band gap engineering of amorphous silicon quantum dots for light-emitting diodes. *Applied Physics Letters*, 78(17):2575–2577, 2001.

[78] Marvin J. Weber. *Handbook of optical materials*. CRC Press, Boca Raton, 2003.

[79] Fabian Lücking, Andreas Assion, Alexander Apolonski, Ferenc Krausz, and Günter Steinmeyer. Long-term carrier-envelope-phase-stable few-cycle pulses by use of the feed-forward method. *Opt. Lett.*, 37(11):2076–2078, Jun 2012.

[80] Donna Strickland and Gerard Mourou. Compression of amplified chirped optical pulses. *Optics Communications*, 55(6):447–449, 1985.

[81] M. Schultze, A. Wirth, I. Grguras, M. Uiberacker, T. Uphues, A.J. Verhoef, J. Gagnon, M. Hofstetter, U. Kleineberg, E. Goulielmakis, and F. Krausz. State-of-the-art attosecond metrology. *Journal of Electron Spectroscopy and Related Phenomena*, 184(3):68–77, 2011. Advances in Vacuum Ultraviolet and X-ray Physics.

[82] Tim Paasch-Colberg. *Ultrafast, optical-field-induced currents in solid-state materials*. PhD thesis, Technische Universität München, James-Franck-Straße 1, 85748 Garching bei München, 2014.

[83] Johannes Schötz. *Field-resolved studies of ultrafast light-matter interaction*. PhD thesis, Ludwig-Maximilians-Universität München, Geschwister-Scholl-Platz 1, 80539 München, 2021.

[84] D. L. Rode. Electron mobility in direct-gap polar semiconductors. *Phys. Rev. B*, 2:1012–1024, Aug 1970.

[85] Mina R. Bionta, Felix Ritzkowsky, Marco Turchetti, Yujia Yang, Dario Cattozzo Mor, William P. Putnam, Franz X. Kärtner, Karl K. Berggren, and

Phillip D. Keathley. On-chip sampling of optical fields with attosecond resolution. *Nature Photonics*, 15(6):456–460, Jun 2021.

[86] Nicholas Karpowicz. Nanoantenna tunnelling currents record laser waves. *Nature Photonics*, 15(6):408–410, Jun 2021.

[87] Richard Zallen and William Paul. Band structure of gallium phosphide from optical experiments at high pressure. *Phys. Rev.*, 134:A1628–A1641, Jun 1964.

[88] Najd Altwaijry, Muhammad Qasim, Mikhail Mamaikin, Johannes Schötz, Keyhan Golyari, Michael Heynck, Enrico Ridente, Vladislav S. Yakovlev, Nicholas Karpowicz, and Matthias F. Kling. Broadband photoconductive sampling in gallium phosphide. *Advanced Optical Materials*, n/a(n/a):2202994, 2023.

[89] Fabien Tran and Peter Blaha. Accurate band gaps of semiconductors and insulators with a semilocal exchange-correlation potential. *Phys. Rev. Lett.*, 102:226401, Jun 2009.

[90] The elk code. http://elk.sourceforge.io.

[91] Muhammad Qasim, Dmitry A. Zimin, and Vladislav S. Yakovlev. Optical gain in solids after ultrafast strong-field excitation. *Phys. Rev. Lett.*, 127:087401, Aug 2021.

[92] Alexander Schwarz. *Few-cycle phase-stable infrared OPCPA*. PhD thesis, Ludwig-Maximilians-Universität München, Geschwister-Scholl-Platz 1, 80539 München, 2014.

[93] Enrico Ridente, Matthew Weidman, Mikhail Mamaikin, Clemens Jakubeit, Ferenc Krausz, and Nicholas Karpowicz. Hybrid phase-matching for optical parametric amplification of few-cycle infrared pulses. *Optica*, 7(9):1093–1096, Sep 2020.

[94] Olga Razskazovskaya. *Infrared waveform synthesis for applications in attosecond science*. PhD thesis, Ludwig-Maximilians-Universität München, Geschwister-Scholl-Platz 1, 80539 München, 2017.

[95] Thomas Brabec and Ferenc Krausz. Nonlinear optical pulse propagation in the single-cycle regime. *Phys. Rev. Lett.*, 78:3282–3285, Apr 1997.

[96] Ian Goodfellow, Yoshua Bengio, and Aaron Courville. *Deep Learning*. MIT Press, 2016. http://www.deeplearningbook.org.

[97] Charles R. Harris, K. Jarrod Millman, Stéfan J. van der Walt, Ralf Gommers, Pauli Virtanen, David Cournapeau, Eric Wieser, Julian Taylor, Sebastian Berg, Nathaniel J. Smith, Robert Kern, Matti Picus, Stephan Hoyer, Marten H. van Kerkwijk, Matthew Brett, Allan Haldane, Jaime Fernández del Río, Mark Wiebe, Pearu Peterson, Pierre Gérard-Marchant, Kevin Sheppard, Tyler Reddy, Warren Weckesser, Hameer Abbasi, Christoph Gohlke, and Travis E. Oliphant. Array programming with NumPy. *Nature*, 585(7825):357–362, September 2020.

[98] Wes McKinney. Data Structures for Statistical Computing in Python. In Stéfan van der Walt and Jarrod Millman, editors, *Proceedings of the 9th Python in Science Conference*, pages 56 – 61, 2010.

[99] Martín Abadi, Ashish Agarwal, Paul Barham, Eugene Brevdo, Zhifeng Chen, Craig Citro, Greg S. Corrado, Andy Davis, Jeffrey Dean, Matthieu Devin, Sanjay Ghemawat, Ian Goodfellow, Andrew Harp, Geoffrey Irving, Michael Isard, Yangqing Jia, Rafal Jozefowicz, Lukasz Kaiser, Manjunath Kudlur, Josh Levenberg, Dan Mane, Rajat Monga, Sherry Moore, Derek Murray, Chris Olah, Mike Schuster, Jonathon Shlens, Benoit Steiner, Ilya Sutskever, Kunal Talwar, Paul Tucker, Vincent Vanhoucke, Vijay Vasudevan, Fernanda Viegas, Oriol Vinyals, Pete Warden, Martin Wattenberg, Martin Wicke, Yuan Yu, and Xiaoqiang Zheng. Tensorflow: Large-scale machine learning on heterogeneous distributed systems, 2016.

[100] François Chollet et al. Keras. https://keras.io, 2015.

[101] F. Pedregosa, G. Varoquaux, A. Gramfort, V. Michel, B. Thirion, O. Grisel, M. Blondel, P. Prettenhofer, R. Weiss, V. Dubourg, J. Vanderplas, A. Passos, D. Cournapeau, M. Brucher, M. Perrot, and E. Duchesnay. Scikit-learn: Machine learning in Python. *Journal of Machine Learning Research*, 12:2825–2830, 2011.

[102] Pauli Virtanen, Ralf Gommers, Travis E. Oliphant, Matt Haberland, Tyler Reddy, David Cournapeau, Evgeni Burovski, Pearu Peterson, Warren Weckesser, Jonathan Bright, Stéfan J. van der Walt, Matthew Brett, Joshua Wilson, K. Jarrod Millman, Nikolay Mayorov, Andrew R. J. Nelson, Eric Jones, Robert Kern, Eric Larson, C J Carey, İlhan Polat, Yu Feng, Eric W. Moore, Jake VanderPlas, Denis Laxalde, Josef Perktold, Robert Cimrman, Ian Henriksen, E. A. Quintero, Charles R. Harris, Anne M. Archibald, Antônio H. Ribeiro, Fabian Pedregosa, Paul van Mulbregt, and SciPy 1.0 Contributors. SciPy 1.0: Fundamental Algorithms for Scientific Computing in Python. *Nature Methods*, 17:261–272, 2020.

[103] A. M. Turing. I.—Computing Machinery and Intelligence. *Mind*, LIX(236):433–460, 10 1950.

[104] Wolfgang Ertel. *Introduction to Artificial Intelligence*. Springer Cham, 18 January 2018.

[105] Miroslav Kubat. *An Introduction to Machine Learning*. Springer Cham, 15 October 2016.

[106] Sandro Skansi. *Introduction to Deep Learning*. Springer Cham, 04 February 2018.

[107] Connor Shorten and Taghi M. Khoshgoftaar. A survey on image data augmentation for deep learning. *Journal of Big Data*, 6(1):60, Jul 2019.

[108] F. Rosenblatt. The perceptron: A probabilistic model for information storage and organization in the brain. *Psychological Review*, 65(6):386–408, 1958.

[109] F. Rosenblatt. The perceptron - a perceiving and recognizing automaton. Technical Report 85-460-1, Cornell Aeronautical Laboratory, Ithaca, New York, January 1957.

[110] Marvin Minsky and Seymour Papert. *Perceptrons: An Introduction to Computational Geometry*. MIT Press, Cambridge, MA, USA, 1969.

[111] Diederik P. Kingma and Jimmy Ba. Adam: A method for stochastic optimization, 2014. arxiv:1412.6980.

[112] Jon F. Claerbout. *Fundamentals of geophysical data processing: with applications to petroleum prospecting*. McGraw-Hill Inc., New York, March 1976.

[113] Gregory R. Lee, Ralf Gommers, Filip Waselewski, Kai Wohlfahrt, and Aaron O'Leary. Pywavelets: A python package for wavelet analysis. *Journal of Open Source Software*, 4(36):1237, 2019.

[114] A. Graps. An introduction to wavelets. *IEEE Computational Science and Engineering*, 2(2):50–61, 1995.

[115] D.L. Donoho. De-noising by soft-thresholding. *IEEE Transactions on Information Theory*, 41(3):613–627, 1995.

[116] David L Donoho and Iain M Johnstone. Ideal spatial adaptation by wavelet shrinkage. *Biometrika*, 81(3):425–455, 09 1994.

[117] Ioachim Pupeza, Marinus Huber, Michael Trubetskov, Wolfgang Schweinberger, Syed A. Hussain, Christina Hofer, Kilian Fritsch, Markus Poetzlberger, Lenard Vamos, Ernst Fill, Tatiana Amotchkina, Kosmas V. Kepesidis, Alexander Apolonski, Nicholas Karpowicz, Vladimir Pervak, Oleg Pronin, Frank Fleischmann, Abdallah Azzeer, Mihaela Žigman, and Ferenc Krausz. Field-resolved infrared spectroscopy of biological systems. *Nature*, 577(7788):52–59, Jan 2020.

[118] Martin T. Peschel, Maximilian Högner, Theresa Buberl, Daniel Keefer, Regina de Vivie-Riedle, and Ioachim Pupeza. Sub-optical-cycle light-matter energy transfer in molecular vibrational spectroscopy. *Nature Communications*, 13(1):5897, Oct 2022.

[119] Ayman Alismail, Haochuan Wang, Gaia Barbiero, Syed Ali Hussain, Wolfgang Schweinberger, Ferenc Krausz, and Hanieh Fattahi. Near-infrared molecular fieldoscopy of water. In Ammasi Periasamy, Peter T. C. So, and Karsten König, editors, *Multiphoton Microscopy in the Biomedical Sciences XIX*, volume 10882, page 1088231. International Society for Optics and Photonics, SPIE, 2019.

[120] William Navidi. *Statistics for Engineers and Scientists*. McGraw-Hill Education, NY, 2011.

List of Publications

Publications relevant to this thesis:

- **Altwaijry, N.** *et al.* "Machine learning aided waveform sampling" (working title).
  The author conceived the idea, generated the augmented dataset, wrote and trained the model, analysed the data and is writing the manuscript.

- **Altwaijry, N.** *et al.* "Nonlinear photoconductive sampling in heterostructures" (working title).
  The experiment was conceptualised by the author together with Karpowicz, N. The author performed the necessary simulations, maintained the laser system, built the experimental setup together with Qasim, M., measured and analysed the data, and is writing the manuscript.

- **Altwaijry, N.**, Qasim, M., Mamaikin, M. *et al.* "Broadband photoconductive sampling in gallium phosphide." Advanced Optical Materials, adom 202202994, (2023).
  The experiment was conceptualised by the author together with Golyari, K. The author maintained the laser system, built the experimental setup, fabricated the sample, measured and analysed the data, performed the EOS response simulations, and wrote the manuscript.

- Ridente, E., Mamaikin, M., **Altwaijry, N.** *et al.* "Electro-optic characterization of synthesized infrared-visible light fields." Nature Communications 13, 1111 (2022).
  The author maintained the laser system, built the NPS experimental setup for characterising the VIS-UV arm and measured the NPS and NPS-relevant data. The author discussed and assisted in writing and revising the manuscript together with Ridente, E., Mamaikin, M and Karpowicz, N.

Other publications:

- Mamaikin M., Ridente, E., **Altwaijry, N.** *et al.* "Contrast enhancement in near-infrared electro-optic imaging." Optics Express 30, 18179 (2022).

- Alismail, A., Wang, H., Barbiero, G., **Altwaijry, N.** *et al.* "Multi-octave, CEP-stable source for high-energy field synthesis." Science Advances 6, eaax3408 (2020).

- Alismail, A., Wang, H., **Altwaijry, N.**, Fattahi, H. "Carrier-envelope phase stable, 5.4 μJ, broadband, mid-infrared pulse generation from a 1 ps, Yb:YAG thin-disk laser." Applied Optics 56, 4990 (2017).

Acknowledgements

First and foremost, I would like to sincerely thank my advisor **Prof. Dr. Matthias Kling**. I am incredibly thankful for the freedom he gave me to explore my own scientific ideas and try things out on my own. Prof. Kling's approach and gentle guidance instilled in me a sense of self-reliance, which not only helped me during my PhD but will continue to help me for the rest of my life. Furthermore, I am particularly thankful to him for encouraging me to join both the IMPRS-APS and MPSP, both of which made my PhD much more exciting and enabled me to meet scientists and make friends from all over the world. Through Prof. Kling's support, I also had the chance to work at SLAC and learn from the excellent team of Shambhu Ghimire in my early PhD days. I could not have asked for a better and more supportive mentor!

Secondly, the experiments in this thesis were carried out at the Max Planck Institute for Quantum Optics in the Chair of Experimental Physics - Laser Physics. For that, I would like to extend my genuine thanks to **Prof. Dr. Ferenc Krausz** for permitting me to join his team, learn from his teams' expertise and use his facilities. I would like to thank my direct supervisor **Dr. Nicholas Karpowicz**. The task of conducting and completing this thesis was *a long and taxing journey*. I would not have completed this work if it were not for the guidance and encouragement I received from him. In fact, without Nick's remote support all the way from Italy, the LWS1 laser would still be broken and Chapter 3 would not have existed. Moreover, I would like to thank **Prof. Dr. Vladislav Yakovlev** for his continued support and excellent advice, not only in theory but also in practice.

I would like to thank **Dr. Mikhail Mamaikin** for being the best friend and office mate anyone could ask for. I really enjoyed arguing about nitpicky things in the lab with him. His expertise in aesthetics truly elevated the plots we publish, especially the incorporation of the colour salmon red. My gratitude to **Muhammad Qasim** for running the LPS response simulations - the paper would not have been published without that. It was a great pleasure working with him in the lab, especially the long nights measuring NPS. To **Amelie Schulte** for her great taste in music, her constant and infectious gute Laune even when the laser is broken, and for

being part of the woman-power team in the Krausz group. To **Dr. Keyhan Golyari** for the great scientific discussions, fixing the CPA and teaching me how to do it and, of course, the freshly baked bread he brought every day. To **Simon Reiger** for sharing his extensive knowledge of chemistry and being a constant source of entertainment and finally, to **Marco Dassie**, **Manoram Agrawal** and **Dr. Dmitrii Kormin** for their inspiring and motivational spirits.

I would like to thank my colleagues in the Kling and Krausz groups for their continued engagement. I particularly enjoyed all the cool Christmas parties. Many thanks to Džiugas Kimbaras and Johannes Blöchl for the fun MPSP trips and to Dr. Mathias Krüger for his excellent input on my choice of colour scheme. Thanks to Dr. Volodymyr Pervak for coating the NPS sample. My former colleagues: **Michael Heynck** for helping me fix the lasers, being a cool friend and for his expertise in anything metal-related. Dr. Enrico Ridente for trusting me with his firstborn, the synthesiser. Dr. Dmitry Zimin for teaching me how to do NPS. **Dr. Johannes Schötz** for being a never-ending source of knowledge and experience. My gratitude to the former members of the teams: Dr. Julia Gessner, Dr. Clemens Jakubeit, Dr. Florian Siegrist, Dr. Marcus Ossiander, Yang Cui, Yik Long Li, Ludwig Lorenz, Eva Bayer, Dr. Gaia Barbiero, Dr. Christina Hofer, Sambit Mitra and Maximilian Kubullek.

My friends Clemens Kuhlenkamp, Hadeel Alnegheimish and Aljoharah Alhuqail, thank you for all the good times and distractions. My deepest appreciation goes to **James Sparkes** (I did it bro!), **Nawara Aldossari** and **Dr. Wolfgang Schweinberger** for being there for me for the entirety of this long and arduous journey, for lending me an understanding ear whenever I complained about it and for always having my back. Not enough words can describe my appreciation.

My immeasurable gratitude to **my sisters** Drs. Najla, Najwa and Nojood Altwaijry and **my brothers** Drs. Hesham, Haithem, Hotham and Hani Altwaijry for their constant encouragement and support. They set the bar *so high*, a PhD is not enough to be in their league. Do I have to become an astronaut now or something? Thanks to **my nieces** Yara, Layal, Tala, Tamara, Rahaf and Rula and **nephews** Zeyad, Tariq, Abdulaziz 2.0, Feras, Rakan, Faisal, Yasir, Abdulaziz 3.0, Khalid and Saud. My cats Sylphrena and Kairos, thank you for bringing joy to my life.

Finally, I would like to thank **my father**, who is my source of inspiration and **my mother** for being a force of true and unparalleled resilience. Thank you for constantly encouraging us to pursue our dreams. We all made it this far because of you.